

DISSERTATION

Modeling and Simulation of Ferroelectric Devices

ausgeführt zum Zwecke der Erlangung des akademischen Grades
eines Doktors der technischen Wissenschaften

eingereicht an der Technischen Universität Wien
Fakultät für Elektrotechnik und Informationstechnik
von

Klaus Dragosits

Wien, im Dezember 2000

Kurzfassung

Die vorliegende Arbeit beschäftigt sich mit der Modellierung und Simulation eines neuen Typus von nichtflüchtigen Speicherzellen. Dieser nützt die ferroelektrische Hysterese, eine Materialeigenschaft, die insbesondere bei Perowskiten weit verbreitet ist, um Information zu speichern. Diese Bauelemente sind, in erster Linie wegen ihres signifikant niedrigeren Energieverbrauches und dem einfacheren Schreibzugriff die vielversprechendste Alternative zu den bereits existierenden nichtflüchtigen Speicherzellen wie EPROM, EEPROM und Flash-Speicher.

Das Hauptziel der vorliegenden Arbeit war, für die Analyse dieses neuen Speichertyps geeignete Modelle zu finden und deren Implementierung in den Bauelement-Simulator MINIMOS-NT. Ausgehend von bestehenden, eindimensionalen Hysterese-Modellen wurden Algorithmen entwickelt, die für die zweidimensionale Simulation ferroelektrischer Materialien geeignet sind, und zwar sowohl für die Simulation von Einkristallen als auch für die Simulation polykristalliner Strukturen.

Zusätzlich zur Entwicklung und Implementierung der zweidimensionalen Algorithmen wird das transiente Verhalten gründlich untersucht und ein neuer, auf Differenzialgleichungen basierender Ansatz vorgestellt. Mit diesem kann im Frequenzbereich bis 1MHz eine ausgezeichnete Übereinstimmung zu Messdaten erreicht werden.

Besondere Sorgfalt wurde für die Implementierung in den Simulator MINIMOS-NT aufgewendet. Im Rahmen des von MINIMOS-NT verwendeten generischen Ansatzes wurde ein modulares Konzept entwickelt, das einfach erweiterbar ist. Dies trägt der rasanten technologischen Entwicklung Rechnung, im Zuge derer das Wissen über ferroelektrische Materialien und die Zahl der möglichen Anwendungen beständig wächst.

Um mögliche Anwendungsfelder der neuen Software aufzuzeigen, werden praxisnahe Beispiele vorgestellt. Eine dieser Anwendungen schlägt eine Brücke zur Schaltungssimulation, eine weitere bietet einen genauen Einblick in die Feldverhältnisse in einem isotropen Kristall. Das letzte Beispiel liefert die erste tiefere Analyse des ferroelektrischen Feldeffekt Transistors (FEMFET), eines der vielversprechendsten nicht flüchtigen Speicherbauelemente, und es werden bereits eine Reihe kritischer Aufgabestellungen Bauelementeigenschaften und Haltbarkeit betreffend aufgezeigt.

Abstract

This work deals with the modeling and the simulation of ferroelectric non-volatile memory cells. Their design strategy utilizes the hysteresis in the D/E characteristics that occurs in some of the perovskite type crystals. These devices are the most promising alternative to standard non-volatile memories like EPROM, EEPROM and Flash, primarily because of their drastically lower energy consumption and the easier write access.

The basic purpose of this work was to find models for a rigorous analysis of this new type of storage devices and their implementation into the device simulator MINIMOS-NT. Starting from an analysis of existing models, suitable approaches that match the constraints of two-dimensional device simulation were developed. These include algorithms for single crystals as well as for structures built by a large number of arbitrarily oriented grains.

In addition to the development and implementation of these two-dimensional algorithms, also transient properties are thoroughly investigated, and a new model based on differential equations was introduced. This model offers an excellent fit to the measured data for a frequency range from zero up to 1MHz.

Special care was taken regarding the implementation of the new models into the device simulator MINIMOS-NT. Following the generic approach of MINIMOS-NT a modular concept was found that will also be easily extendable to future simulation tasks, which is absolutely necessary as the knowledge about ferroelectric materials and the possible applications is still increasing.

In order to demonstrate possible applications of the new tools a series of concrete examples is provided. One of these examples builds a bridge from two-dimensional device geometry to circuit simulation, another one allows deep insight into the field properties inside an anisotropic crystal. The last example serves as the first profound analysis of a new, very promising nonvolatile memory cell, the ferroelectric field effect transistor (FEMFET), and several critical issues concerning device performance and reliability are pointed out.

Acknowledgment

First from all I want to thank my advisor, Professor Selberherr, who provided me with a perfect working environment. His exceptional international reputation and his close contacts to the international semiconductor industry allowed me to gain a lot of experience and to keep in touch with up to date technology issues. I am also grateful to Professor Hauser for his support and his service on my examining committee.

I have to express my thanks to Infineon Villach for financial support of this thesis and the people I was cooperating with at Infineon Munich and Infineon Graz, especially to Rainer Hagenbeck for many interesting discussions and his support of my work. Special thanks to Oliver Lohse from the Technische Hochschule Aachen, as he performed many essential measurements for me.

It is a pleasure to express my thanks to the people I cooperated with at the Samsung Advanced Institute of Technology in Suwon/South Korea, namely to Dr. Byoung-Ho Cheong for the perfect organization of my internship, and to Dr. Chung for the fruitful scientific cooperation.

Special thanks to Charles Dachs from Philips Research/Eindhoven for the interesting time during my internship, the perfect organization and his attempts to show me the glamorous aspects of Eindhoven.

I am very grateful to all my colleagues at the Institute for Microelectronics. Special thanks goes to Martin Knaipp, who supported my bootstrapping at the institute. Furthermore I have to express my gratitude to Tibor Grasser, Robert Mlekus and Robert Klima. Their efforts for the development of MINIMOS-NT provided a solid basis for my work. In this context I want to thank Christian Troger, Thomas Binder and Rudolf Strasser for the perfect administration of our Linux cluster. Special thanks as well to Robert Kosik and Wolfgang Pyka for many fruitful discussions concerning my work.

Of course I have to mention my colleague I shared office with for the last three years, Vassil Palankovski. I will never forget our thrilling conversations on chauvinism, especially on the topics of whether the Austrians or the Bulgarians “invented” semiconductor physics, radio transmission, computers, and lazy soccer players. Special thanks as well to the part time inhabitant of our office, Rüdiger Quay. Even though from Germany, his exceptional sense of humor, his education and his intelligence made it a pleasure to spend the evenings with him and a few pints of Guinness.

Special thanks to my colleagues from the lunch and network testing group, “Highlander” Christian Harlander, “Anne Dy” Andreas Hössinger, “Saba” Rainer Sabelka, “Cerv” Johann

Cervenka, “Wolfine” Wolfgang Pyka, and Heinrich Kirchauer for the interesting and funny discussions during lunch time and after. Not to forget Peter Fleischmann, who introduced me into the secrets of system administration and Japanese culture.

Special thanks go to my sister, Eva Dragosits, who spent several nights in order to improve my English.

Finally, I thank my parents, as their support was of vital importance for my personal and academic advancement.

Table of Contents

Kurzfassung	i
Abstract	ii
Acknowledgment	iii
Table of Contents	v
List of Abbreviations	ix
List of Symbols	x
List of Figures	xiii
List of Tables	xvii
1 Introduction	1
1.1 Simulation of Ferroelectric Materials	2
1.2 Outline of the Thesis	2
2 Ferroelectricity	4
2.1 Instabilities in Crystals with a Centrosymmetric Prototype	4
2.2 Structural Properties of Perovskites	6
2.2.1 Perfect Cubic Structure	6
2.2.2 Distorted Cubic Structure – Ferroelectricity	6
2.3 Microstructure	10
2.4 Domains	11
2.4.1 Analysis of Domain Configuration	12

3	Modeling of Hysteresis	15
3.1	Compact Modeling with Discrete Devices	15
3.2	Compact Modeling - Preisach Hysteresis	17
3.2.1	Turning Point	19
3.2.2	Depolarization	20
3.2.3	Subcycles	21
3.2.4	Memory Wipe Out	23
3.3	Lattice Models – Minimized Free Energy	24
3.3.1	Lattice Models	26
3.4	Discussion of the Models	27
4	Two-Dimensional Simulation	29
4.1	Shape Functions	29
4.1.1	The arctan Shape Function	30
4.1.2	The tanh Shape Function	30
4.1.3	Comparison between the Shape Functions	31
4.2	Two-Dimensional Algorithm	32
4.2.1	Two-Dimensional Properties	32
4.2.2	Single Crystals – Polycrystals	32
4.2.3	Polarization in an Orthogonal Direction	33
4.2.4	Algorithm for Anisotropic Materials	35
	Uniaxial Materials	35
	Biaxial Materials	35
4.2.5	Algorithm for Materials without any Favored Direction	35
4.2.6	Comparison of the Two-Dimensional Approaches	39
4.2.7	Simple, One-Dimensional Model	39
4.3	Comparison of the Two-Dimensional Model to Measurements	40
5	Frequency Dependent Simulation	41
5.1	Modeling	41
5.2	Discretization	42
5.3	Comparison to Measurement	43
5.4	Extraction of the Parameters	45

5.5	Analysis of Signal Response	46
5.5.1	Frequency and Amplitude Dependence of the Coercive Field	46
5.5.2	Pulse Shape and Amplitude	47
5.5.3	Switching of a Capacitor	48
5.6	Measurement of Frequency Dependence	49
6	Implementation	54
6.1	Preprocessing	54
6.1.1	User Interface	54
	Control Parameters	57
	Physical Input Quantities	58
	Device Description	58
6.1.2	Calculations	59
6.2	Numerical Calculation	60
6.2.1	Discretization	61
6.2.2	Nonsymmetry of the Locus Curves - Sign Handling	61
6.2.3	Detection of the Locus Curves	62
6.2.4	Calculation - Data flow	63
6.3	Postprocessing	64
6.3.1	Memory Management	64
6.3.2	Data Flow of Postprocessing	67
7	Ferroelectric Non-volatile Memory Cells	68
7.1	The Transistor Capacitor Memory Cell	69
7.1.1	Double Cell Design	69
7.1.2	Single Cell Design	70
7.2	The Ferroelectric Memory Field Effect Transistor	73
7.2.1	Operating Principle	74
8	Simulation of Ferroelectric Devices	76
8.1	Extraction of Equivalent Parameters for a Finger Structure	77
8.2	Simulation of Thin Films	78
8.2.1	Simulation of Materials with Uniaxial Anisotropy	79

<i>TABLE OF CONTENTS</i>	viii
8.2.2 Simulation of Materials with Biaxial Anisotropy	85
8.3 Analysis of a Ferroelectric Memory Field Effect Transistor	89
8.3.1 Transfer Characteristics	91
8.3.2 Field and Charge Distribution	91
8.3.3 Discussion	92
9 Conclusion and Outlook	97
List of Publications	102
Curriculum Vitae	103

List of Abbreviations

BL	Bit Line
EEPROM	Electrically Erasable and Programmable Read-Only Memory
EPROM	Electrically Programmable Read-Only Memory
FEMFET	Ferroelectric Memory Field Effect Transistor
LTI	Linear Time Invariant
PE	Preisach-Everett
RC	Resistor Capacitor
PL	Plate Line
TCAD	Technology Computer Aided Design
WL	Write Line
1C1T	Single Transistor Single Capacitors
2C2T	Two Transistors Two Capacitors

List of Symbols

A_{down}	Area in the PE Diagram with Down Oriented Dipoles
A_{up}	Area in the PE Diagram with Up Oriented Dipoles
C_B	Bitline Capacity
C_F	Ferroelectric Capacitor
C_S	Sense Capacitor
d	Width
D	Electric Displacement
E	Electric Field
E_a, E_b	Operating Points of the Electric Field
E_c	Coercive Field
E_i, E_k	Electric Field at the Grid Point i, k
$E_{i,x}, E_{i,y}$	x- and y-Component of the Electric Field at the Grid Point i
E_{ik}	Electric Field between the Grid Points i and k
$E_{ik,x}, E_{ik,y}$	x- and y-Component of the Electric Field between the Grid Points i and k
E_d	Transition Field in the Down Direction
E_{old}	Electric Field of the Previous Operating Point
E_{stat}	Static Electric Field
E_{turn}	Turning Point Electric Field
E_u	Transition Field in the Up Direction
E_1	Electric Field of the Current Operating Point
$E_{1,\perp}$	Orthogonalized Field
$f(E \pm E_c, k)$	Hysteresis Shape Function
$f_{\text{loc},\parallel}$	Subcycle Parallel to the Electric Field
$f_{\text{loc},\perp}$	Subcycle Orthogonal to the Electric Field
$F(E_u, E_d)$	Distribution Function of the Transition Fields
G	Total Free Energy
I	Electrical Current
I_d	Drain Current
I_0	Initial Current
k	Subcycle Parameter
k_{nonlin}	Parameter of the Nonlinear Transient Polarization Term
p_n	Dipole Moment of the n th Dipole
p_m, n	Dipole Moment of the n th Dipole in the m th Row
P	Polarization

P_{ef}, P_{pol}	Transient Polarization Components
P_{nonlin}	Nonlinear Transient Polarization
P_{off}	Subcycle Parameter
P_{old}	Polarization of the Previous Operating Point
P_{stat}	Static Polarization
P_{turn}	Turning Point Polarization
P_{Ferro}	Hysteretic Polarization
P_{Part}	Dipole Polarization
P_{Rem}	Remanent Polarization
P_S	Spontaneous Polarization
P_{Sat}	Saturation Polarization
P_{turn}	Turning Point Polarization
P_0	Polarization in the Domain Center
$P_{ }$	Polarization Parallel to the Electric Field
P_{\perp}	Polarization Orthogonal to the Electric Field
P_1	Current Polarization
$P_{old, }$	Previous Parallel Component of the Polarization
$P_{old,\perp}$	Previous Orthogonal Component of the Polarization
$P_{1, }$	Current Parallel Component of the Polarization
$P_{1,\perp,init}$	Initial Guess to the Current Orthogonal Component of the Polarization
$P_{1,\perp}$	Current Orthogonal Component of the Polarization
R_f	Series Resistance of the Ferroelectric Capacitor
R_i	Input Resistanc of the Digitizer
s_h	Sign Flag
t	Time
t_{cryst}	Crystal Thickness
Δt	Time-step
T	Temperature
T_C	Curie Temperature
V	Volume
V_g	Gate Voltage
V_i	Input Voltage
V_{out}	Output Voltage
V_t	Threshold Voltage
V_B	Bulk Voltage
V_D	Drain Voltage
V_{DD}	Supply Voltage
V_S	Source Voltage
w	Shape Parameter
W_{dip}	Dipole Energy
W_E	Depolarization Energy
W_W	Wall Energy
$vec{X}$	Space Coordinate
α	Angle
α, β	Parameters for the Free Energy Model
χ	Susceptibility

LIST OF SYMBOLS

xii

ϵ_r	Relative Permittivity
ϵ_0	Vacuum permittivity
ϵ^*	Constant Depending on the Permittivity
γ	Viscosity Coefficient
Φ_i, Φ_k	Potential at Grid Point i,k
ρ	Space Charge Density
σ	Electric Conductivity
σ_{Wall}	Wall Energy Density
τ_1, τ_2	Time Constants
τ_{ef}	Relaxation Time of the Electric Field
τ_{pol}	Relaxation Time of the Polarization

List of Figures

2.1	Fundamental types of uniaxial instabilities of centrosymmetric crystals (after Lines and Glass [LG96])	5
2.2	Fundamental types of biaxial instabilities of centrosymmetric crystals (after Lines and Glass [LG96])	6
2.3	Lattice structure of a symmetric perovskite crystal	7
2.4	Tetragonally distorted crystal	8
2.5	Polarization of a tetragonally distorted crystal	8
2.6	Potential distribution in the direction of the spontaneous polarization	9
2.7	Rhombohedrally distorted crystal	9
2.8	Monoclinicly distorted crystal	9
2.9	Hysteresis loop	10
2.10	Structural model of a 180° and a 90° domain wall	12
2.11	Head to head domain wall	13
2.12	Scheme of a zigzagged domain wall	13
2.13	Periodic domain structure	14
3.1	Parallelogram shaped hysteresis	15
3.2	SPICE based compact model with parallelogram shaped hysteresis	16
3.3	Hysteresis loop for an individual particle	17
3.4	Polarization density function $F(E_d, E_u)$	18
3.5	Preisach-Everett diagram, increasing electric field	19
3.6	Hysteresis loop, increasing electric field	20
3.7	Preisach-Everett diagram, turning point	20
3.8	Resulting hysteresis loop for a single turning point	21
3.9	Preisach-Everett diagram after two turning points	21

3.10	Preisach-Everett diagram, depolarization	22
3.11	Hysteresis loop for depolarization	22
3.12	Minor loop	23
3.13	Memory wipe out	24
3.14	One-dimensional lattice model, atoms in the double minimum potential interact with their neighbors, cyclic boundary condition $p_1 = p_{n+1}$	25
3.15	Hysteresis of the free energy model	26
4.1	Comparison of the arctan and the tanh shape function	31
4.2	Location of the center ion, first axis of anisotropy	32
4.3	Location of the center ion, second axis of anisotropy	32
4.4	Application of an electric field orthogonal to the remanent polarization	33
4.5	Construction of the polarization components	34
4.6	Construction of the lag angle	34
4.7	Algorithm for materials with more than one axis of anisotropy	36
4.8	Splitting of the field vectors	37
4.9	Calculation of the initial guess	38
4.10	Calculation of the polarization	39
4.11	Reduction of the orthogonal component	39
4.12	Non-ferroelectric blocking layer	40
5.1	Comparison simulation to measurement, Supplier 1	43
5.2	Comparison simulation to measurement, Supplier 2	44
5.3	Comparison simulation to measurement, coercive field	45
5.4	Algorithm to fit the parameters	46
5.5	Coercive voltage as a function of frequency and peak voltage	47
5.6	Signal response as function of frequency, sinusoidal pulse	48
5.7	Signal response as function of frequency, triangular pulse	49
5.8	Signal response as function of amplitude, sinusoidal input with 1MHz	50
5.9	Charge and current response of a voltage step	50
5.10	Charge and current response of a transient simulation	51
5.11	Sawyer-Tower circuit	51
5.12	Equivalent circuit diagram	51

5.13	Initial oscillations of the Sawyer-Tower circuit for different ratios of the resistors	52
5.14	Distorted output signal	53
6.1	Schematic overview of preprocessing	55
6.2	Control concept	58
6.3	Data flow of preprocessing	60
6.4	Possible locus curves in an operating point	62
6.5	Detection of the change of the electric field, electric field decreases.	63
6.6	Detection of the change of the electric field, electric field increases.	64
6.7	Modified trivial iteration scheme	64
6.8	Data flow of the numerical calculation	65
6.9	Overview of postprocessing	66
6.10	Data flow of postprocessing	67
7.1	Overview of the different ferroelectric memory designs	69
7.2	Cross section of a stacked transistor-capacitor structure	70
7.3	2C2T circuit	71
7.4	Sense scheme of a 2C2T circuit	71
7.5	1C1T circuit	72
7.6	Sensing scheme of the write operation of the 1C1T circuit	72
7.7	Approximation of the hysteresis loop with capacitors	73
7.8	Timing diagram of the read operation of the 1C1T circuit	73
7.9	Ferroelectric non-volatile memory field effect transistor	74
7.10	ON state of the FEMFET	75
7.11	OFF state of the FEMFET	75
8.1	Cross section of a finger structure and the simulated area	76
8.2	'One-dimensional' capacitor versus finger structure	77
8.3	Polarization reversal near the edge of the contact	78
8.4	Comparison of the transfer characteristics of a finger structure and the 'one-dimensional' capacitor with fitted hysteresis parameters	79
8.5	Definition of the angle α of the axis of anisotropy	80
8.6	Hysteresis curves for different angles of the anisotropy axis	81
8.7	Distribution of the polarization field, angle = 45°	82

8.8	Distribution of the electric field, angle = 45°	83
8.9	Distribution of the potential, angle = 45°	84
8.10	Hysteresis curves for different angles of the anisotropy axes; two perpendicular anisotropy axes are applied	85
8.11	Total polarization in a device with two anisotropy axes	86
8.12	Polarization in the first anisotropy direction, angle = 15°	87
8.13	Polarization in the second anisotropy direction, angle = 75°	88
8.14	Geometry of the gate area	89
8.15	Acceptor doping distribution of NMOS and FEMFET	90
8.16	Donor doping distribution of NMOS and FEMFET	90
8.17	Transfer characteristics for different peak voltages, linear scale	91
8.18	Transfer characteristics for different peak voltage, logarithmic scale	92
8.19	Space charge density in the ON state	93
8.20	Current density in the ON state	94
8.21	Space charge density in the OFF state	95
8.22	Current density in the OFF state	96

List of Tables

3.1	Comparison between different simulation approaches	28
6.1	Control parameters	57
6.2	Device description	59
7.1	Comparison of different types of non-volatile memories, after Sheikoleslami [SG00]	68

Chapter 1

Introduction

AS IT IS well known, semiconductor based non-volatile storage devices have left their central area, computers, in recent years and entered the world of consumer electronics. Especially qualities like low power and space consumption, silence and low marginal costs make them very attractive.

Applications like digital cameras or MP3 players are already entering the market and it seems to be only a question of time until they will have marginalized their precursors. Consequently the market for non-volatile memories is constantly growing and it is very unlikely that this will change soon.

This development got a significant boost of popularity with the introduction of Flash memory, which allows to program an arbitrary single cell and to electrically erase a large number of cells en block. This enhances their flexibility compared to electrically programmable read-only memories (EPROMs), which are electrically programmable as well, but demand an ultraviolet exposure to be erased. The electrically erasable and programmable read-only memories (EEPROMs) are programmable and erasable by single byte, but they demand more chip space compared to Flash technology, which makes them more expensive and limits their scope to special applications only [PBOZ97].

Still Flash memories have some not so highly appreciated properties. Compared to the supply voltage, their write and erase operations demand a significantly higher voltage, which leads to an increased complexity of the on-chip circuits and also to a rather high power consumption. Considering that non-volatile memories are especially attractive as storage device for mobile electronic components and that power consumption and compact circuit design are the main issues in this area, the search for alternative designs becomes reasonable.

The most attractive approach in this context is the introduction of ferroelectric materials. From 127 papers on non-volatile memory reported by the INSPEC data base between January 1999 and July 2000, 53 are on ferroelectrics.

Similar to ferromagnetics, ferroelectrics show a nonlinear dependence on the applied field and a remanent field component, just not in terms of magnetization but in terms of polarization. This leads to some very interesting effects compared to standard type non-volatile memory. First, as the information is stored inside the material, these memory cells are expected to

be superior in terms of time stability without refresh. Data retention rates of more than ten years are expected [Maz00]. Another advantage is that designs are possible that use the on chip supply voltage for read and write operations.

1.1 Simulation of Ferroelectric Materials

Many questions concerning ferroelectric non-volatile memory cells are still not clarified, since this is a comparatively young technology. These include key issues like material properties, device design, circuit design and sensing schemes.

This leads to a difficult situation for research engineers. For example device and circuit designers should be able to transform the steady flow of innovation into new, more powerful memory cells, but each innovation might lead to side effects which can hardly be predicted from the present state of the research. This situation is even intensified by the highly nonlinear properties of the ferroelectric materials.

Consequently, the utilization of simulation tools becomes very attractive. In order to match the demands of device research, the following features have to be provided:

- No restrictions in terms of materials
- Arbitrary two-dimensional geometry
- Arbitrary compound of materials, including semiconductors
- Temperature dependence
- Transient behavior
- Simulation of small circuits

Up to date several approaches for the simulation of ferroelectric materials have been tried, but none of them combines all of the characteristics outlined above. They concentrate either on circuit simulation [BEL97][Dun94] or on effects inside the material like domain wall movement [Ish92][OAI91] or material phase transitions [RW95][WR97]. More relevant for development tasks is an approach that adds the ability to simulate ferroelectric materials to a state-of-the art device simulator like MINIMOS-NT [BDG⁺98], as it is the case for the work presented in this thesis.

1.2 Outline of the Thesis

This thesis starts with a brief description of the properties of ferroelectric materials in Chapter 2 and provides information on the physical properties involved. An overview of the modeling of these materials follows in Chapter 3, with special emphasis on hysteresis. This section concentrates on two different approaches, compact modeling and lattice modeling.

In Chapter 4 these models are analyzed with respect to TCAD requirements. Utilizing the results of this discussion, algorithms are introduced which allow the general two-dimensional simulation of hysteresis.

Chapter 5 concentrates on the frequency dependence of ferroelectric materials. A model is introduced which offers an excellent correspondence with measurements for one of the most popular ferroelectric materials, PbZrTiO_3 (PZT).

The next chapter focuses on the details concerning the implementation of the models into MINIMOS-NT. This includes control concept, data flow and special analysis of the requirements of the models concerning numerics and discretization.

Chapter 7 contains an overview of the different designs of ferroelectric memory cells and their read and write operations.

In order to demonstrate the abilities of the introduced simulation tool, several simulation results are presented in the subsequent chapter. The examples provide an overview of possible applications of the simulation tool.

The thesis is concluded by an outlook on remaining challenges.

Chapter 2

Ferroelectricity

IT HAS become common knowledge that there are materials with a permanent magnetic moment. The fact that there is a similar phenomenon for the electric moment as well is part of the curriculum of physical or related university education, but is usually regarded as only one of many exotic effects. Primarily this is caused by the fact that the number of applications of ferroelectric materials was limited and not of general interest. Until recently ferroelectrics have mainly been used for sonar detectors, ceramic capacitors, and phonograph pick-ups, but today there is a wide interest in taking advantage of their properties in the semiconductor industry, and the first products are already entering the market.

Ferroelectricity was discovered in 1920. The first known ferroelectric material was Rochelle salt. Unfortunately, Rochelle salt loses its ferroelectric properties if the composition is slightly changed, which made it rather unattractive for industrial applications. It was mainly regarded as an interesting physical effect. In 1945, ferroelectric behavior was reported for BaTiO_3 [LG96]. This material is of stable perovskite type, which is one of the fundamental crystal lattice structures. This discovery brought the perovskite type materials into the scope of investigations. Soon other perovskites with ferroelectric properties were discovered, thus opening the path to industrial application. Perovskites are still the most important ferroelectric materials.

2.1 Instabilities in Crystals with a Centrosymmetric Prototype

Temperature and/or pressure determine the structure (structural phase) of crystals. At high temperature the materials usually show highest symmetry. This phase is called the prototype phase.

Ferroelectricity is one of the possible effects caused by asymmetry of a material where the prototype phase is centrosymmetric. In the following an overview is given on the different types of asymmetry that evolve if the temperature drops beyond a certain level, the Curie Temperature T_C .

Typically, asymmetric structures show two or more states with the same energy, and depending on the energy barrier between them, one of these states can transform easily into the other, thus forming an instability in the lattice structure. If there are only two possible positions for the center ion, and both of them are situated at one of the symmetry axes of the lattice, the instability is called uniaxial.

An overview of the different types of uniaxial instabilities is given in Fig. 2.1.

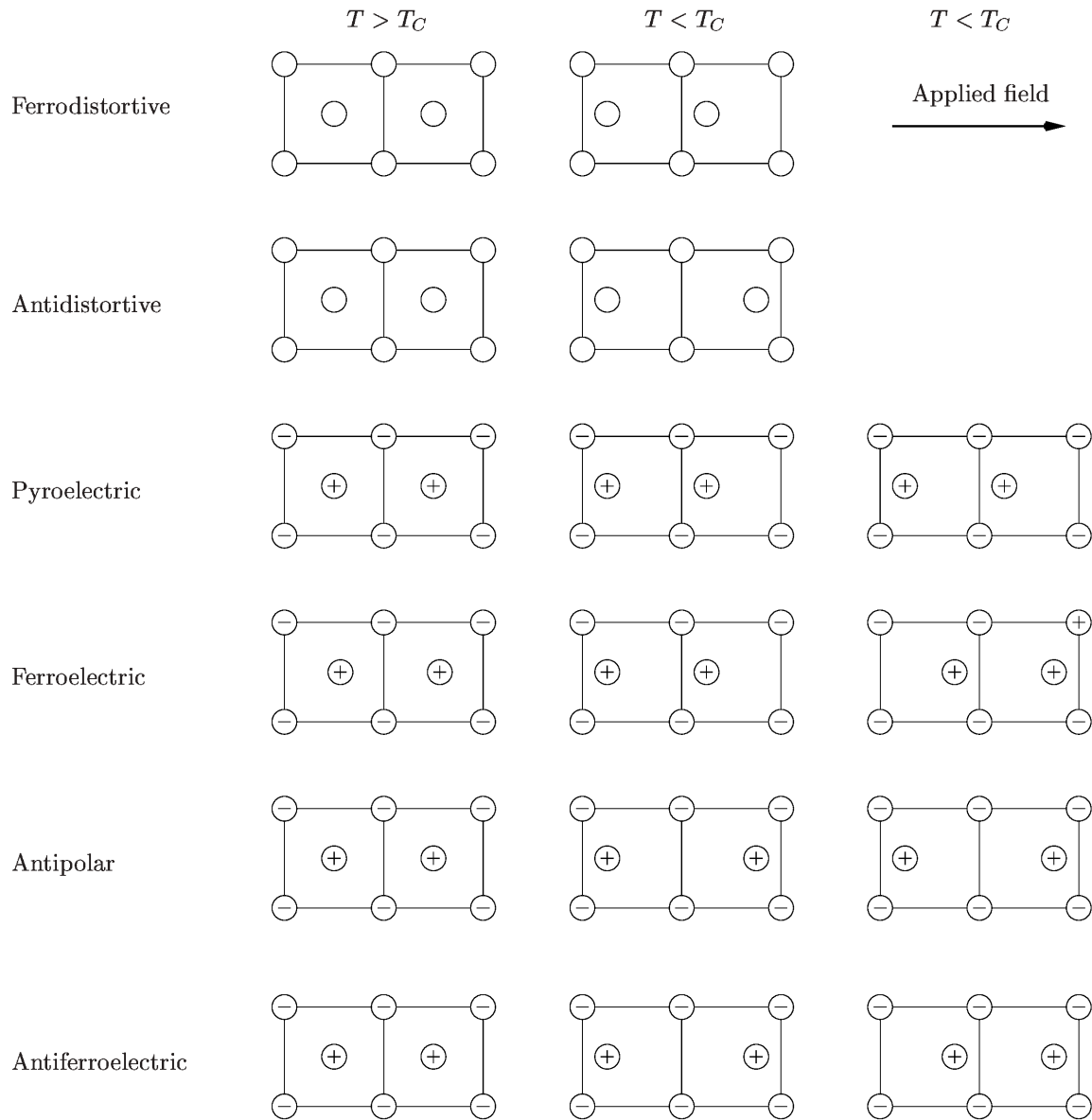


Figure 2.1: Fundamental types of uniaxial instabilities of centrosymmetric crystals (after Lines and Glass [LG96])

If the material is biaxial, any combination of the phase transitions outlined above is possible. This means that a material can show e.g. ferroelectric properties in one direction and antipolar ones into the other. Some of these possible transitions are outlined in Fig. 2.2

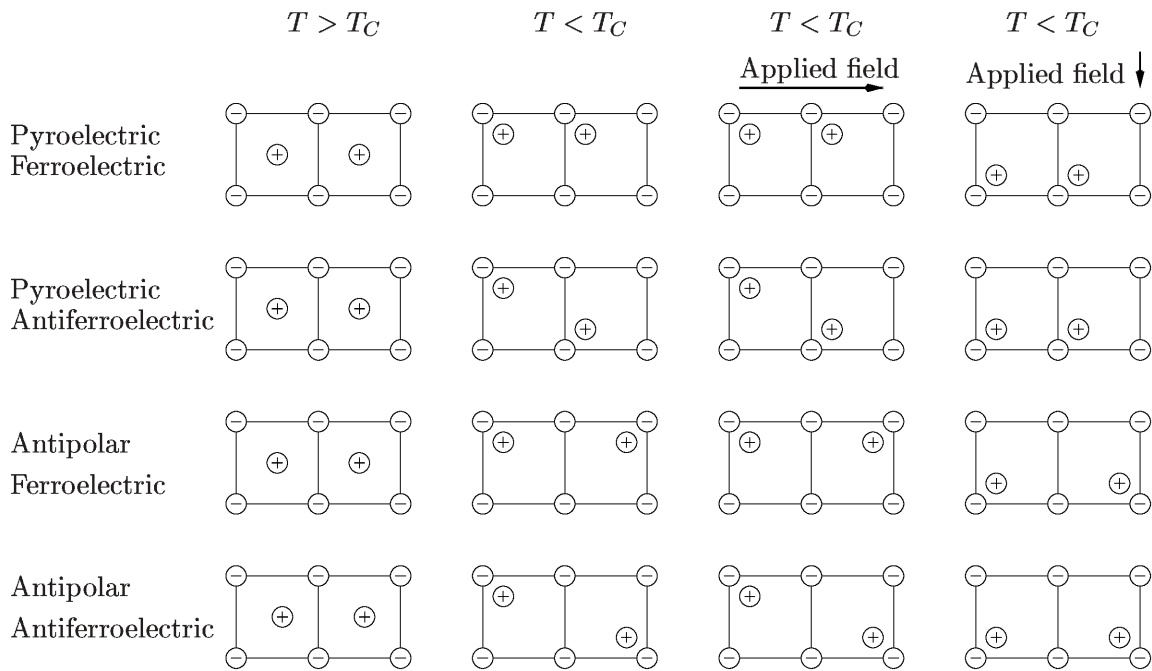


Figure 2.2: Fundamental types of biaxial instabilities of centrosymmetric crystals (after Lines and Glass [LG96])

2.2 Structural Properties of Perovskites

As outlined above, perovskites form the most important class of ferroelectric materials. They are named after the mineral perovskite CaTiO_3 (it was discovered later that CaTiO_3 shows only a distorted perovskite structure). The perfect structure follows the formula ABO_3 , where A is a mono- or divalent and B is a tetra- or pentavalent metal [Die97]. As outlined in Fig. 2.3, the A atoms form the corners of the 'cubic' cells, B atoms are in the center and the oxygen atoms are situated in the faces' centers. As the B atoms are enclosed in O_6 octahedra, this structure is also regarded as BO_6 .

2.2.1 Perfect Cubic Structure

If the material shows a perfect cubic lattice, no ferroelectricity can be observed. A typical perovskite showing no ferroelectric phase at room temperature is SrTiO_3 . Still, as the ABO_3 structure is set up by ionized atoms, an electric field will lead to a dislocation of these ions, which will raise an electric moment. Finally these effects will increase the overall displacement and the dielectric susceptibility $\chi = \epsilon_r - 1$.

2.2.2 Distorted Cubic Structure – Ferroelectricity

As already outlined in Section 2.1, ferroelectricity is caused by asymmetries in the lattice structure. If for example the Sr in SrTiO_3 is replaced by a Ba ion which has a bigger

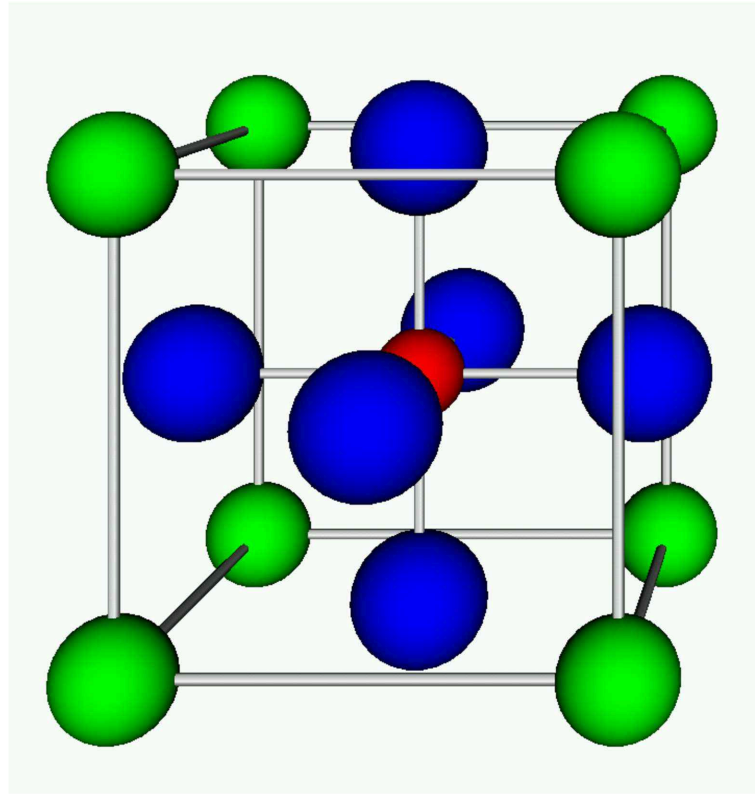


Figure 2.3: Lattice structure of a symmetric perovskite crystal

diameter, the cubic structure gets tetragonally distorted at room temperature and the height of the crystal increases compared to its base (base length= 3.98\AA , height= 4.03\AA) [Die97]. This distortion is schematically outlined in Fig. 2.4, the resulting polarization in Fig. 2.5. Fig. 2.6 shows the potential distribution around the small center ion B in the z-direction. The minimum does not occur in the center of the structure. Instead, the outlined double well energy structure, will evolve [LG96] along the z-axis of the crystal. Now there are two different energetically favored states for the positive center ion, both of them resulting in a dipole moment. Consequently the center ion will be trapped in one of these two positions as long as the thermal energy is lower than the barrier height. The crystal cell will carry a permanent polarization, which is called the spontaneous polarization P_S .

Depending on the temperature there are two other distorted crystal phases for BaTiO_3 , each of them with a different geometry of the unit cell. For temperatures beyond -80°C the crystal becomes rhombohedral, between -80°C and about -5°C monoclinic. This will raise different orientations and absolute values of the spontaneous polarization [Kit86]. The respective unit cells are sketched in Fig. 2.7 and Fig. 2.8.

Initially, all the spontaneous polarizations of individual cells will be randomly distributed throughout the material, so the resulting overall displacement will be zero.

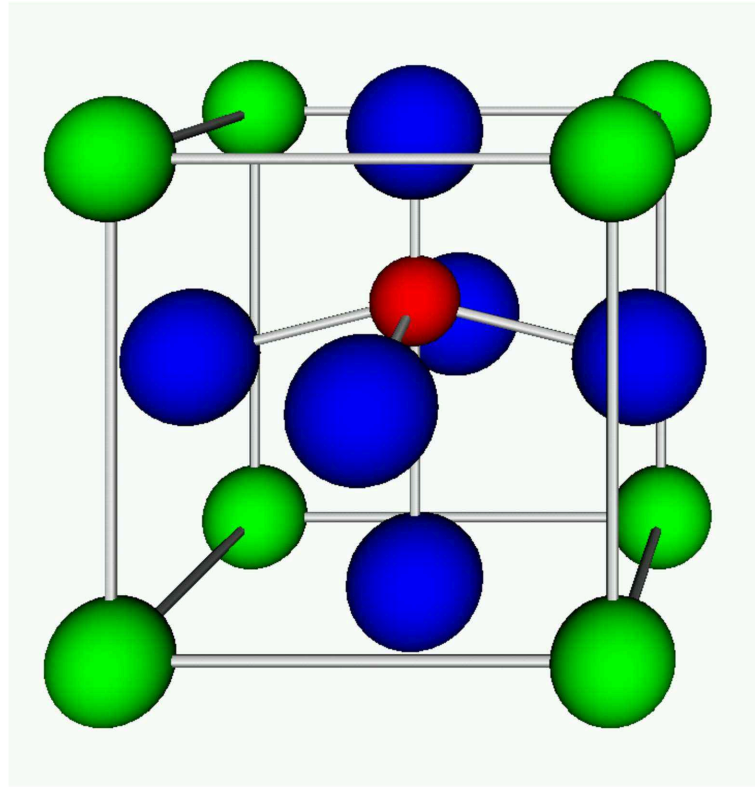


Figure 2.4: Tetragonally distorted crystal

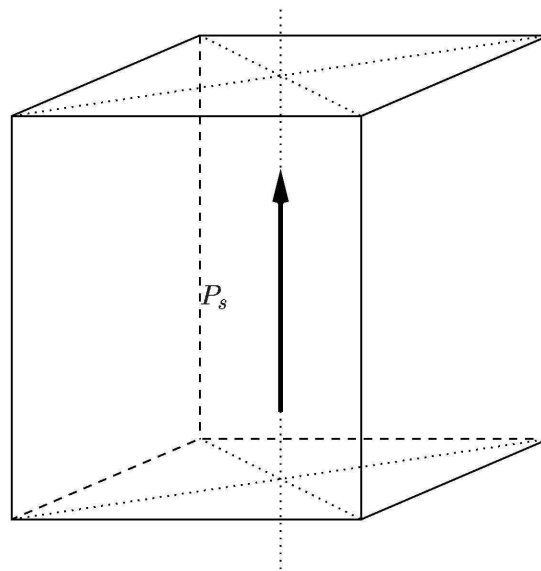


Figure 2.5: Polarization of a tetragonally distorted crystal

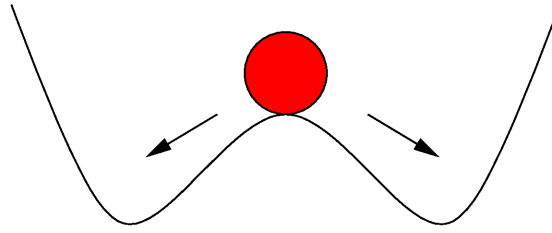


Figure 2.6: Potential distribution in the direction of the spontaneous polarization

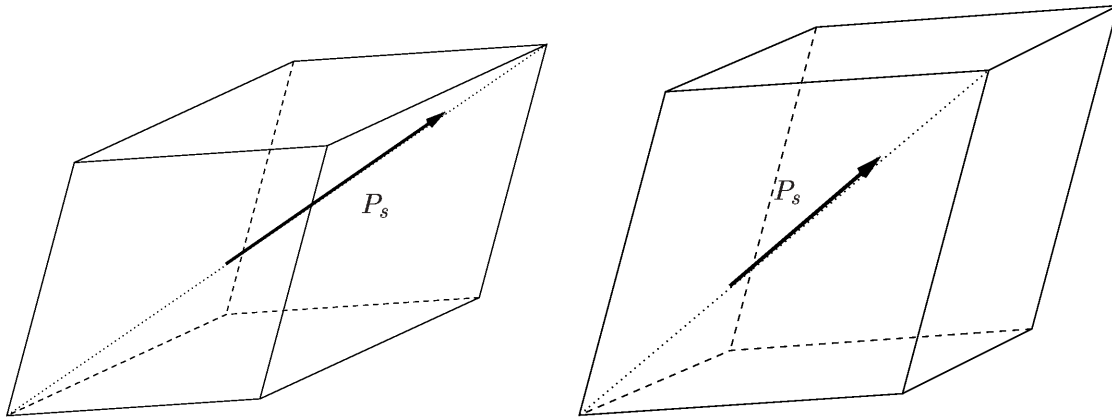


Figure 2.7: Rhombohedrally distorted crystal

Figure 2.8: Monoclinically distorted crystal

If an electric field is applied, the ions will be pushed towards the energetically better position, and if the applied field is big enough, the ions will cross the potential barrier. In an undistorted, perfect crystal this transition field is the same for each lattice cell. Impurities and stress modify the energy barriers locally and smoothen the resulting D/E characteristics.

When all the dipoles are organized into the same direction, the maximum contribution of the dipole moment to the displacement is reached. This component is called saturation polarization P_{Sat} .

If the electric field is reduced to zero again, many of the dipoles will be trapped in the last state causing a resulting polarization of the material, called remanent polarization P_{Rem} . If the electric field is turned into the other direction, the resulting polarization is decreased to zero. The field necessary to achieve this is called the coercive field E_c . This behavior leads to a hysteresis of the D/E characteristics, outlined in Fig. 2.9. The effects related to hysteresis can be summarized as follows:

- Hysteresis consists of many different branches (locus curves).
- By default these locus curves are nonsymmetric functions.
- The locus curves depend on the history.

Similar to magnetism the D/E characteristics can be separated into a linear and a nonlinear part,

$$D = \epsilon_r \cdot \epsilon_0 \cdot E + P_{\text{nonlin}}. \quad (2.1)$$

Even though wrong from a rigorous point of view, it has become quite common in the literature on ferroelectrics to denote the nonlinear part P_{nonlin} as polarization. As the nonlinear part stems from the switching dipoles, it will be denoted as P_{Ferro} throughout this work.

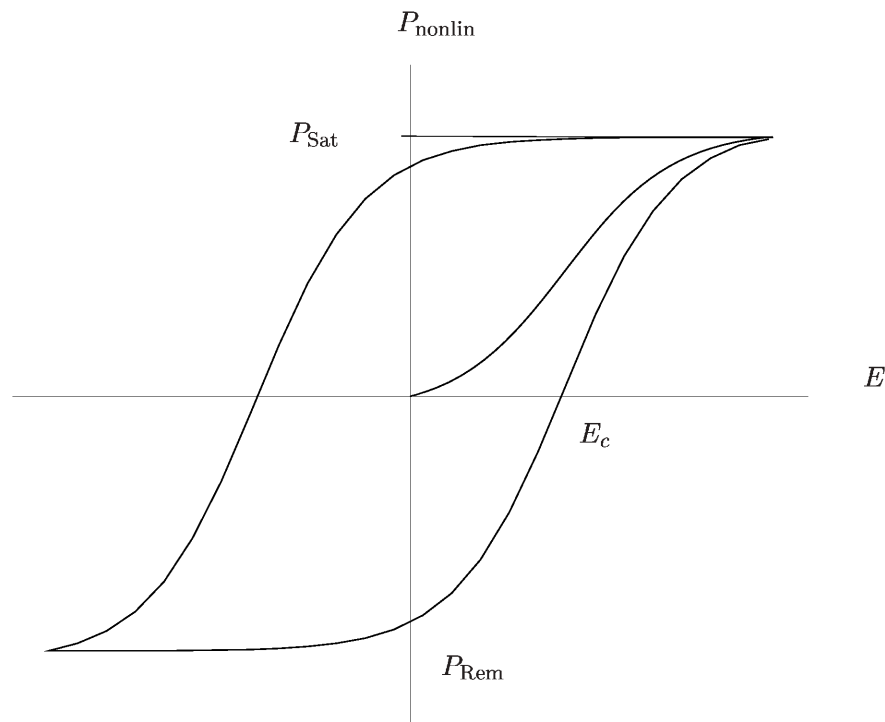


Figure 2.9: Hysteresis loop

2.3 Microstructure

Depending on the process, perovskite type ceramics show a great variety of microstructures. These structures vary from epitaxial films to fine grained polycrystalline. Apart from perfect epitaxial films, structures that are epitaxial only perpendicular to the substrate surface are quite common. In this case the grain boundaries cross the entire film, thus leading to a columnar microstructure.

Typical grain sizes vary between 3 and 100 μm for conventional titanate ceramics and 10 to 100nm for fine grained thin films [Die97].

2.4 Domains

Domains represent volumes of the same orientation of the dipoles. Similar to magnetism, domain structures also arise in ferroelectric materials, but of course the proper equations are different, and furthermore, the existence of free electric charge has consequences for the long time behavior of the material.

To allow an analysis of this subject, the material equation (2.1) and Poisson's equation

$$\operatorname{div} \vec{D} = \rho \quad (2.2)$$

are transformed with respect to the divergence of the electric field and the ferroelectric polarization P_{Ferro}

$$\operatorname{div} \vec{E} = \frac{1}{\epsilon_r \cdot \epsilon_0} \cdot (\rho - \operatorname{div} \vec{P}_{\text{Ferro}}). \quad (2.3)$$

In an infinite crystal the ferroelectric polarization \vec{P}_{Ferro} is uniform and $\operatorname{div} \vec{E} = \rho/\epsilon_r\epsilon_0$, as in non-ferroelectric dielectrics. In finite ferroelectrics, properties are more complicated. At the surface P_{Ferro} is reduced to zero, while in the neighborhood of defects $\operatorname{div} \vec{P}_{\text{Ferro}}$ does not vanish and acts, according to (2.3), as the source of an electric field, the so-called depolarization field.

The depolarization energy W_E plays an important role in the formation of the domains. When a crystal cools down from the paraelectric phase in the absence of fields, there is, as outlined previously, only a limited number of possible directions of the spontaneous ferroelectric polarization. In order to minimize the free energy, different regions polarize in one of those directions, thus forming the domain structure. If no electric field is applied, this structure usually shows no net polarization in a virgin crystal.

The other important contribution to the domain layout is the energy of the domain walls W_W . The final configuration will minimize the sum of both of these entries to the total energy.

Basically two different types of domain walls are common in ferroelectrics. The actual formation depends on the relative orientation of the distortion direction of two neighboring domains with different directions of the spontaneous polarization, the related angles being 90° and 180° , respectively. These two wall types are outlined in Fig. 2.10. As the unit cell is not symmetric, the 90° wall shows a distorted lattice structure. Furthermore, the center ions can be located at two equivalent positions, thus the respective figure shows two ions occupying the domain wall cells.

In principle also domain walls with a head to head scheme of ferroelectric polarization are possible (Fig. 2.11), but as they raise a large depolarization field, they are not favored in terms of the energy. Head to head walls have been observed in BaTiO_3 , but electro-microscopic examinations revealed a zigzagged domain wall layout (Fig. 2.12), which increased the overall wall length by a factor of 5.

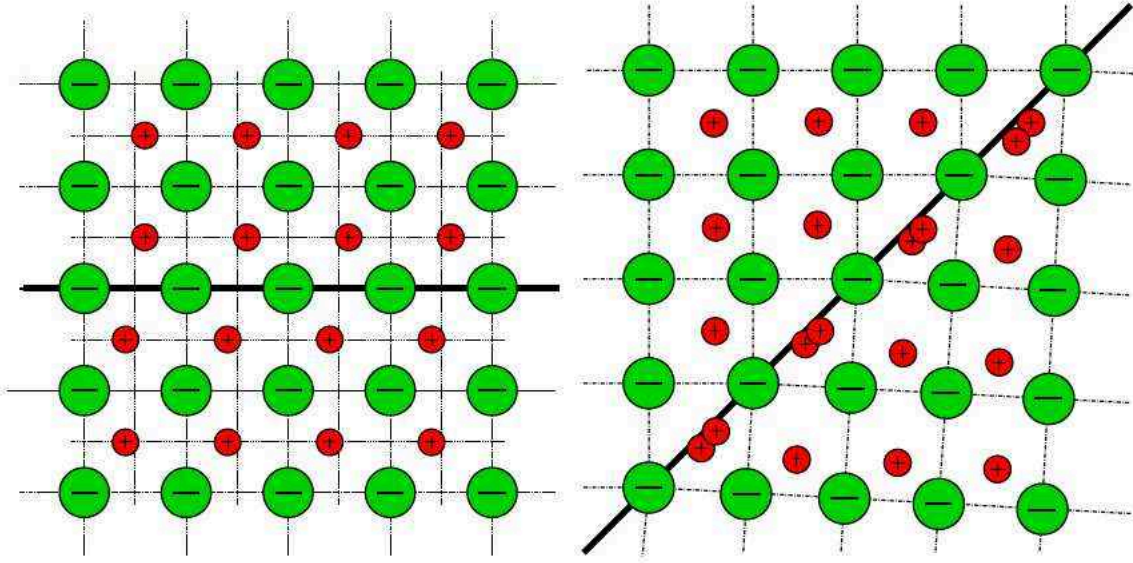


Figure 2.10: Structural model of a 180° and a 90° domain wall

In contrast to the magnetic equivalent, this field can be compensated by the flow of free charge inside and outside the medium

$$\rho = \int_0^t \sigma \cdot E \cdot dt, \quad (2.4)$$

where σ is the electric conductivity of the material. As the conductivities of ferroelectrics and the surrounding air are usually low, the equilibrium where the energy of the depolarization field

$$W_E = \frac{1}{2} \cdot \int_V D \cdot E \cdot dV \quad (2.5)$$

is zero is reached very slowly.

Consequently, after the depolarization field is compensated by the free charges of a conductive ferroelectric material, theoretically a single domain structure should evolve. In reality, this is very unlikely since material properties are not ideal.

2.4.1 Analysis of Domain Configuration

As a consequence of the above considerations, a domain configuration evolves, which minimizes the total free energy G . The free energy includes the two entries outlined above, the energy of the depolarization field W_E , stemming from the surface, and the energy of the domain walls W_W . With the energy term related to the shift of the ions W_{dip} , it finally reads as

$$G = W_{\text{dip}} + W_E + W_W. \quad (2.6)$$

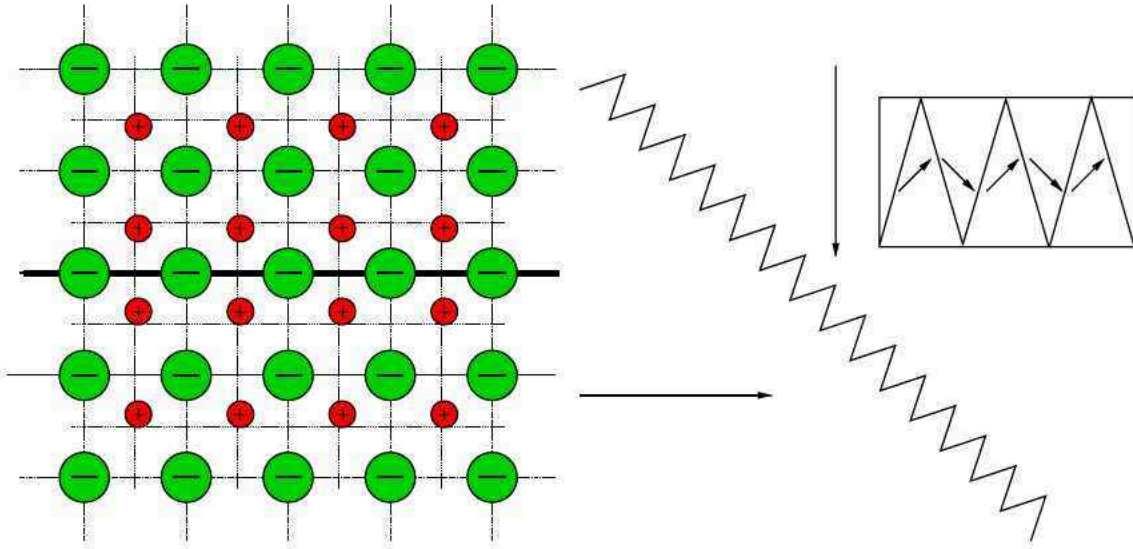


Figure 2.11: Head to head domain wall

Figure 2.12: Scheme of a zigzagged domain wall

The exact calculation of the energy term related to the dipoles, W_{dip} , is far from trivial. A simplified model that allows at least a rough analysis will be introduced later in Section 3.3.

The depolarization energy W_E depends on the crystal and domain geometry at the crystal surfaces. If the geometry is rather simple, analytic calculations are possible, thus giving a good insight into the mechanisms involved in the formation of domain structures. For this consideration it is assumed that the currents inside the ferroelectric material are neglectable and accordingly the surface charge is not compensated.

In the simplest case of a thin crystal with uniform polarization perpendicular to the surface, it is not surprising that the electric depolarization field is proportional to the polarization [LG96]

$$E = -\frac{1}{\epsilon_0}P. \quad (2.7)$$

Things get more complicated for multi domain structures. Still for a periodic domain structure as outlined in Fig. 2.13 an analytic description is possible. One obtains

$$W_E = \frac{\epsilon^* \cdot d \cdot P_0 \cdot V}{t_{\text{cryst}}} \quad (2.8)$$

for the depolarization energy, where d is the domain width, t_{cryst} is the crystal thickness, P_0 is the polarization in the center of a domain, V is the crystal volume, and ϵ^* is a coefficient depending on the dielectric permittivity [MF53]. Using the domain wall energy per unit area σ_{Wall} , the overall domain energy W_W in Fig. 2.13 is

$$W_W = (\sigma_{\text{Wall}}/d) \cdot V. \quad (2.9)$$

The wall energy itself consists of several independent contributions. These are the depolarization energy stemming from $\text{div } \vec{P}$ at the domain boundaries, the dipolar energy caused by

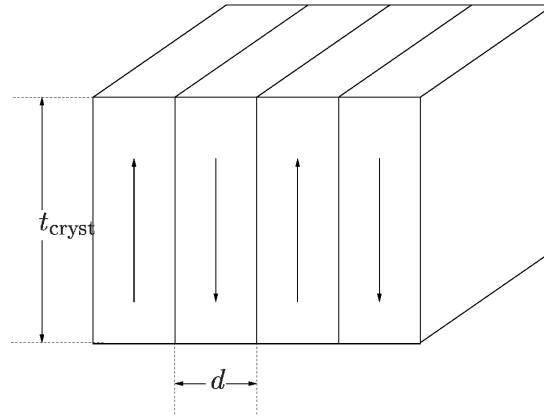


Figure 2.13: Periodic domain structure

the misalignment of the ferroelectric dipoles on both sides of the domain wall and the elastic energy.

The minimum of these two entries is

$$W_E + W_W = \frac{\epsilon^* \cdot d \cdot P_0 \cdot V}{t} + (\sigma_{\text{Wall}}/d) \cdot V, \quad (2.10)$$

and with respect to the domain width one reads

$$d = \sqrt{\frac{\sigma_{\text{Wall}} \cdot t_{\text{cryst}}}{\epsilon^* \cdot P_0^2}}. \quad (2.11)$$

Even this simple analysis delivers remarkable results. First, the resulting domain width is finite if the polarization in the material is not zero. This effect prevents any finite structure from showing a uniform polarization. The next remarkable result is that neither the energy of a domain wall nor the domain width can be zero. Finally, this states that a pure random distribution of the orientations of the dipoles is not possible, as the area between two of them already has to be regarded as a domain wall. This leads to the strong result that there have to be domains of finite size.

Chapter 3

Modeling of Hysteresis

DEPENDING on the purpose of the simulation, several different approaches to the simulation of hysteresis have been developed up to now. This chapter summarizes and discusses these approaches according to their ability to meet the constraints of device simulation.

3.1 Compact Modeling with Discrete Devices

Especially in the context of large scale integrated circuits, modeling of hysteresis with the standard devices provided by the well-known circuit simulator SPICE [Nag75] is very useful.

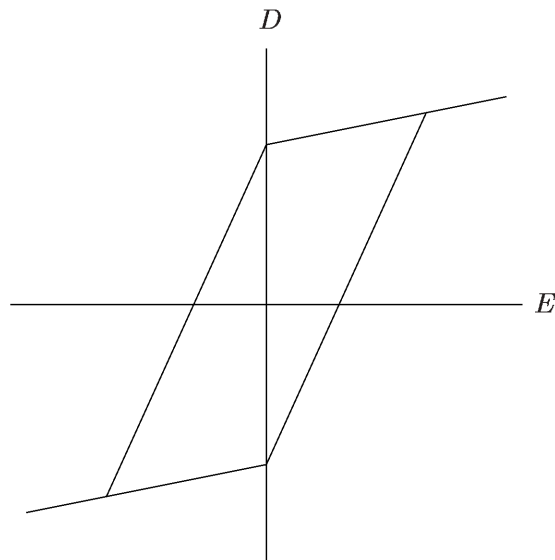


Figure 3.1: Parallelogram shaped hysteresis

The simplest model approximates the shape of the hysteresis in the form of a parallelogram, as sketched in Fig. 3.1. The circuit, as outlined in Fig. 3.2, consists of a history dependent voltage source V_P and two additional capacitors. These two capacitors are connected to the input voltage V_{IF} . In order to model bulk parasitics, two diodes are added to the circuit in parallel and in series. The output quantity of this model is the charge which is stored at the nodes 1 and 2.

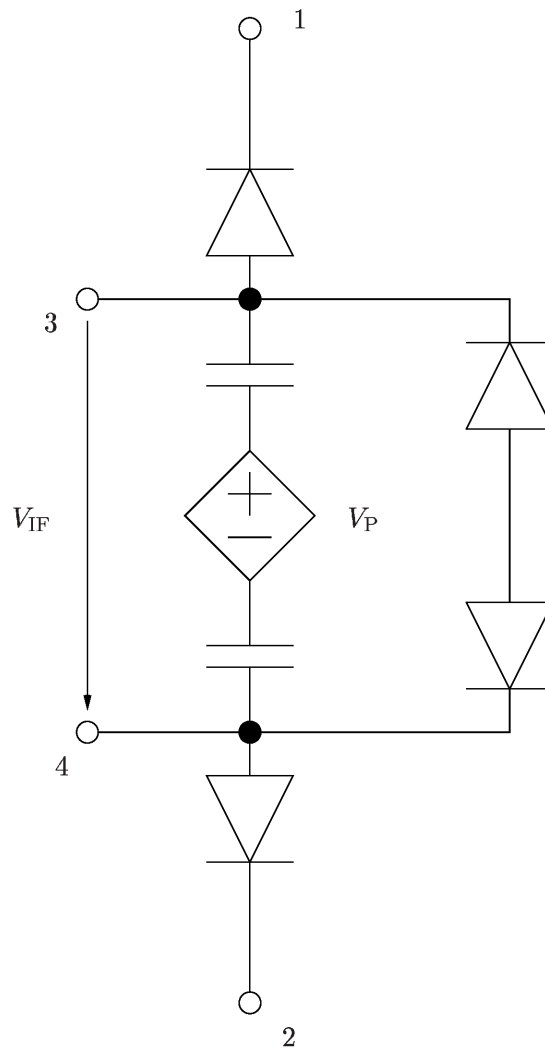


Figure 3.2: SPICE based compact model with parallelogram shaped hysteresis

It has to be mentioned that the shape of the hysteresis function resulting from this model, the parallelogram, only offers a poor fit to the physical properties, as it does not reproduce the shape very accurately.

In 1994 Dunn [Dun94] proposed an extension of this model which allows the simulation of transient behavior. This model simulates the relaxation currents with two exponential terms and two different time constants τ_1 and τ_2 as follows:

$$I(t) = I_0 \cdot (e^{-t/\tau_1} - e^{-t/\tau_2}). \quad (3.1)$$

These properties can be added to the SPICE model by a modification of the history dependent voltage source V_P . This modification is achieved by the introduction of additional RC circuits.

Different approaches were tried in the field of magnetic hysteresis by Brachtendorf et al. [BEL97], based on theoretical work of Jiles and Atherton [JA86]. These have an increased capacity to reproduce the actual shape of the hysteresis function.

3.2 Compact Modeling - Preisach Hysteresis

The basis for this approach was laid for magnetism by F. Preisach as early as 1938 [Pre35]. Later it was intensively tested for adsorption hysteresis and finally verified for magnetic MnAlGe by Barker et al. [BSHE83] in 1983. In 1997 Jiang et al [JZJ⁺97] proved that this model is applicable for ferroelectric materials as well and an excellent fit can be obtained.

The basic idea of this approach is modeling the material through a cluster of independent dipoles. Each of these dipoles can switch between two opposing states, thus showing a rectangular hysteresis as in Fig. 3.3. The according mathematical formulation is

$$\begin{aligned} \frac{dE}{dt} > 0 \quad \wedge \quad E < E_u &\Rightarrow P = -P_{\text{Part}} \\ &\quad \wedge \quad E > E_u &\Rightarrow P = +P_{\text{Part}} \\ \frac{dE}{dt} < 0 \quad \wedge \quad E < E_d &\Rightarrow P = -P_{\text{Part}} \\ &\quad \wedge \quad E > E_d &\Rightarrow P = +P_{\text{Part}}. \end{aligned} \quad (3.2)$$

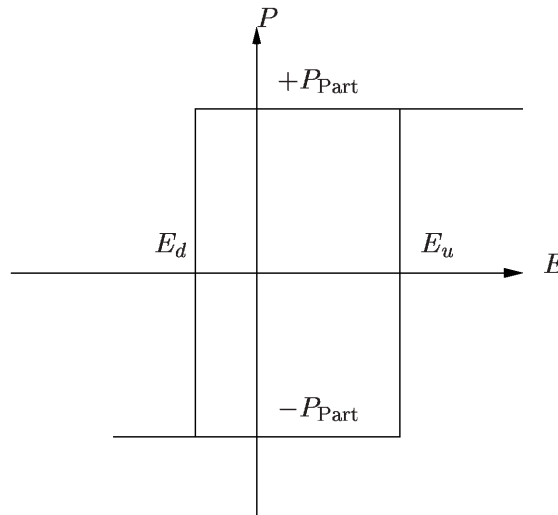


Figure 3.3: Hysteresis loop for an individual particle

E_u is the transition field in the 'up' direction, E_d the transition field in the 'down' direction. As outlined in the figure, the transition fields are not symmetrical and furthermore not even restricted to a specific sign. This means that E_d might, e.g., be positive as well as negative. P_{Part} is the polarization of a single dipole. The next assumption is that these transition fields are statistically distributed. $F(E_u, E_d)$ is the distribution function, its integral has to be 1. For the Preisach model this distribution function contains all the relevant hysteresis information.

According to this description the overall polarization can be easily calculated as

$$P = P_{\text{Sat}} \cdot \int_{A_{\text{up}}} F(E_d, E_u) \cdot dA + (-P_{\text{Sat}}) \cdot \int_{A_{\text{down}}} F(E_d, E_u) \cdot dA, \quad (3.3)$$

where A_{up} is the area in the $E_u - E_d$ plane where the dipoles are oriented upwards and A_{down} the area where the dipoles are oriented downwards.

A possible distribution function is outlined in Fig. 3.4. It shows a peak at a certain point $E_u = -E_d = E_0$ and is furthermore expected to be symmetrical around the line $E_u = -E_d$.

This simple model leads to remarkable results for the analysis of ferroelectric materials, and, as mentioned, also shows an excellent correspondence to measured data. In order to allow a graphical analysis of the hysteresis, the range of the values is restricted from 0 to a maximum transition field E_{max} for the transition field E_u , and from 0 to $-E_{\text{max}}$, for the other transition

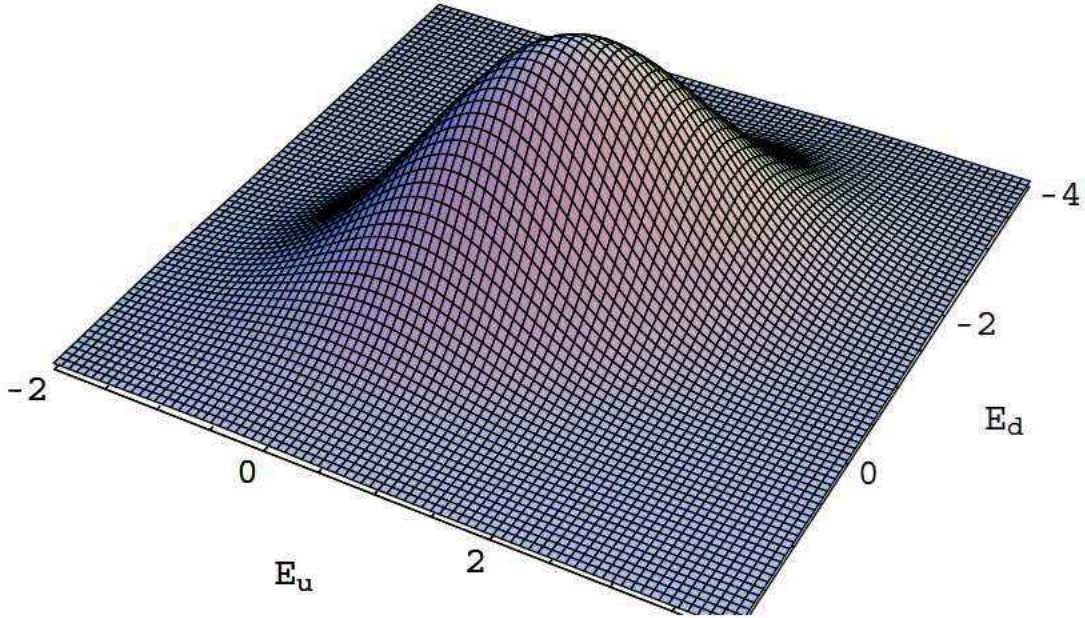


Figure 3.4: Polarization density function $F(E_d, E_u)$

field E_d . As shown below, this does not reduce the universality of the obtained conclusions. In order to illustrate the state of the dipoles, a top view of the distribution function, the Preisach-Everett diagram is plotted [BSHE83].

3.2.1 Turning Point

It is assumed that the whole device is polarized into negative saturation with the applied electric field smaller than $-E_{\max}$. Then the electric field is increased up to a first operating point A with a respective field strength E_A . The dipoles will start to turn according to the distribution of the transition fields. According to (3.3) the overall polarization reads as

$$P = P_{\text{Sat}} \cdot \int_{-\infty}^{E_A} \int_0^{E_{\max}} F(E_u, E_d) \cdot dE_d \cdot dE_u + (-P_{\text{Sat}}) \cdot (1 - \int_{-\infty}^{E_A} \int_0^{E_{\max}} F(E_u, E_d) \cdot dE_d \cdot dE_u) \quad (3.4)$$

The state of the dipoles is plotted in the Preisach-Everett (PE) diagram Fig. 3.5. The light/dark red areas represent the dipoles with positive/negative polarization.

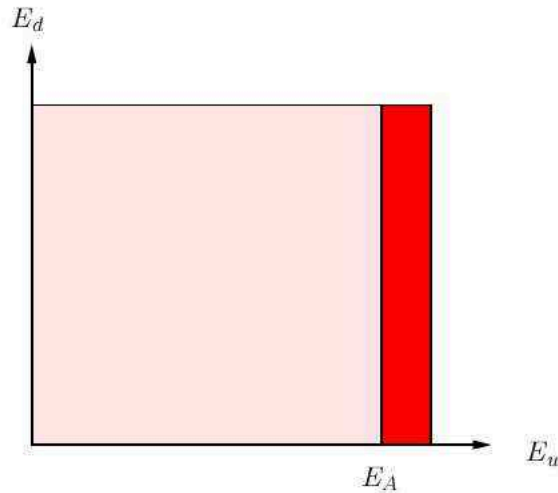


Figure 3.5: Preisach-Everett diagram, increasing electric field

For actual simulations the hysteresis is not calculated by integration of the distribution function, but by an analytic function that matches the measurements for a particular material. In brief, not the distribution function is evaluated, but its integral. Fig. 3.6 shows the related first locus curve.

Next the direction is changed again and the electric field is decreased to $E_B < E_A$. It has to be considered that no dipoles with already negative orientation can be taken into account for transition, so the switching criterion has to be applied to the remaining dipoles only. The resulting Preisach-Everett diagram for the next branch of the hysteresis is shown in Fig. 3.7.

The polarization will decrease according to the distribution until finally all of the dipoles are oriented in the same direction again and the hysteresis loop closes. Fig. 3.8 shows this loop

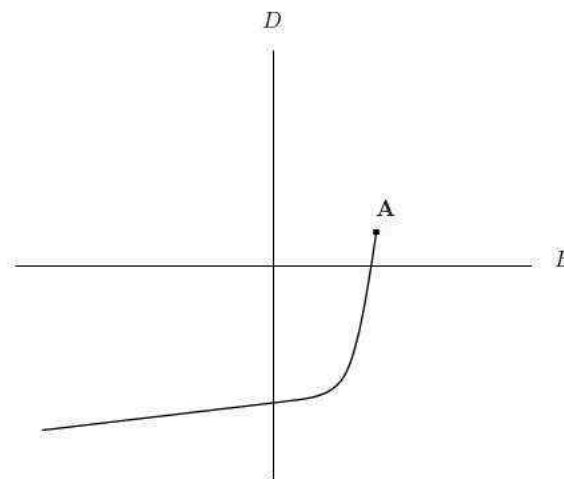


Figure 3.6: Hysteresis loop, increasing electric field

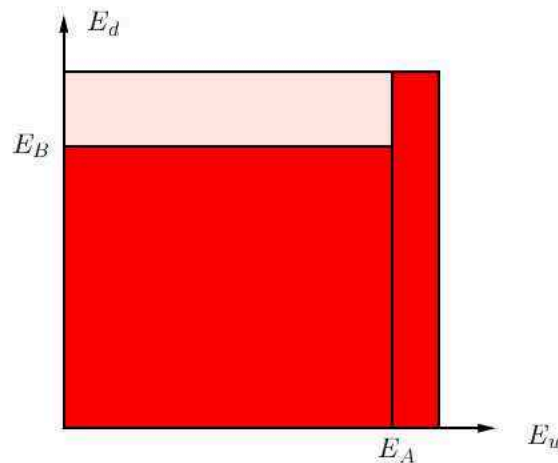


Figure 3.7: Preisach-Everett diagram, turning point

and, in order to allow a comparison, the saturation loop is plotted as well. These loops and all the following ones were calculated simulating a capacitor.

3.2.2 Depolarization

Preisach hysteresis allows the simulation of the well-known effect of depolarization: If the response of a triangularly shaped signal with constantly decreasing amplitude as it is applied for depolarization of ferroelectric materials is calculated, the scheme outlined above has to be followed. It is assumed that the electric field is reduced to an operating point E_B and then increased again to the next operating point E_C . The according Preisach-Everett diagram is plotted in Fig. 3.9.

It is obvious that the dipoles that are already in the up direction (light red color) do not have to change their state. If the row of turning points with decreasing amplitude is extended, a

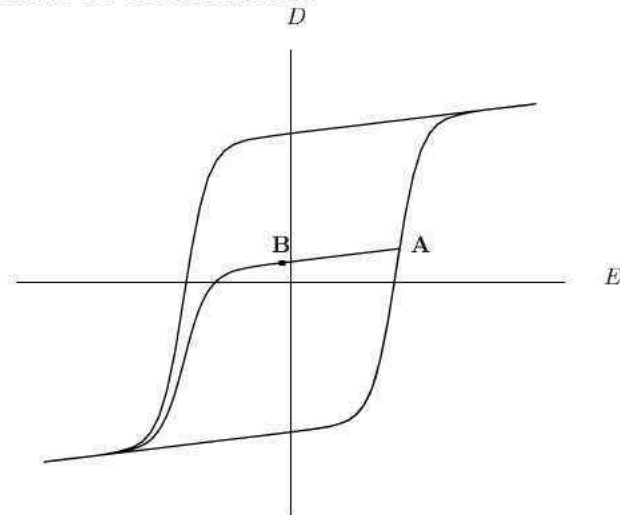


Figure 3.8: Resulting hysteresis loop for a single turning point

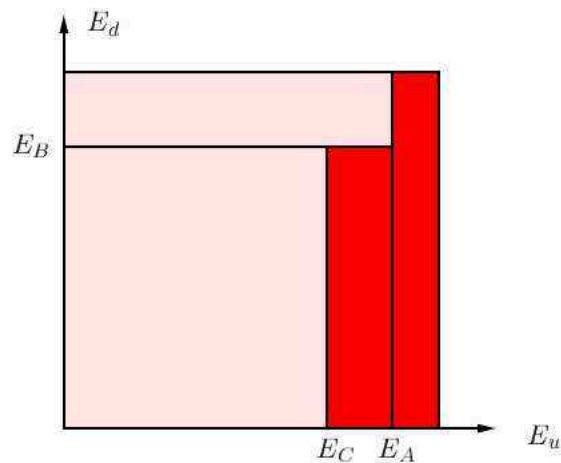


Figure 3.9: Preisach-Everett diagram after two turning points

distribution with the size of the up and down areas fairly equivalent, as outlined in Fig. 3.10, will evolve.

Consequently, the resulting polarization will be almost zero at zero applied field, thus reproducing a well-known physical fact. The hysteresis curve which documents the depolarization process is plotted in Fig. 3.11.

3.2.3 Subcycles

One of the big advantages of the Preisach hysteresis is that it can describe subcycles very accurately. If long term effects like accommodation are neglected, the hysteresis loop hits the operating point of the last local electric field maximum (minimum). This effect has been

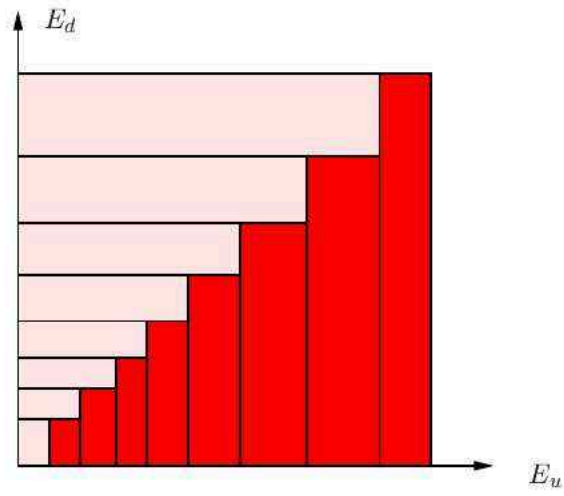


Figure 3.10: Preisach-Everett diagram, depolarization

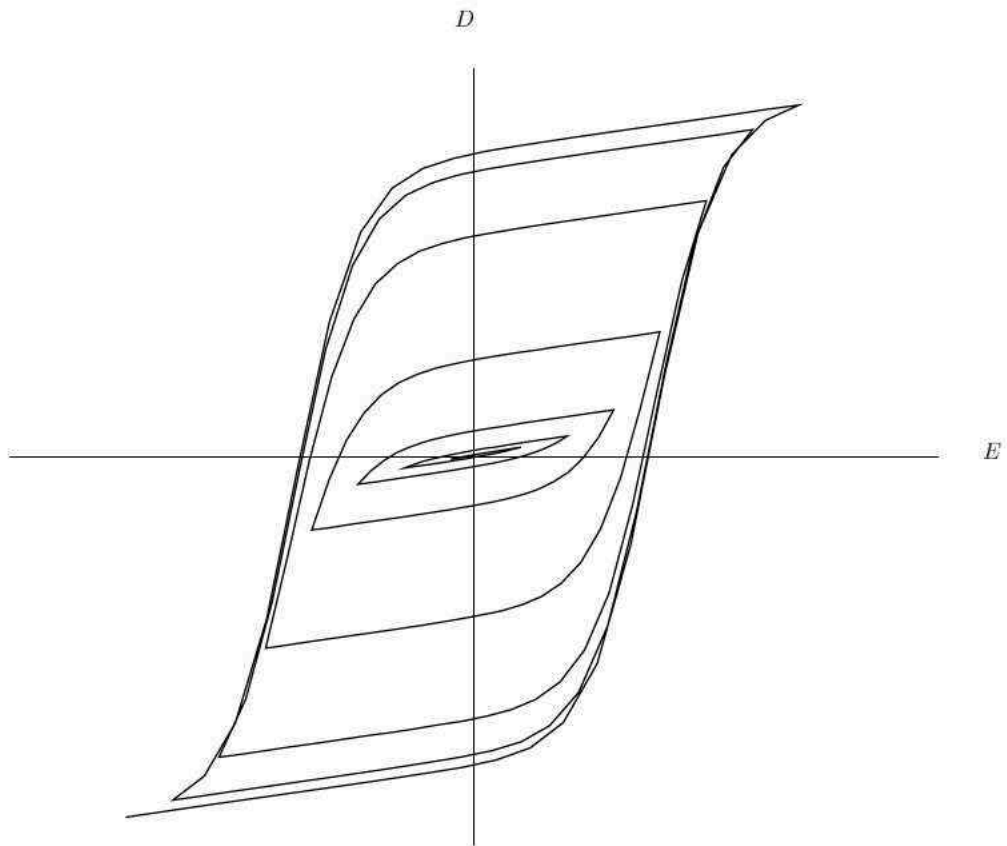


Figure 3.11: Hysteresis loop for depolarization

observed for ferroelectric [JZJ⁺97] and ferromagnetic materials [BSHE83] as well. In this section it will be outlined how the model achieves this.

The analysis starts right with the situation outlined in Fig. 3.9. Contrarily to the previous section, it is assumed that no turning point occurs, which means that the electric field is still increasing in size. If the electric field reaches the same value as at the first turning point E_A , dipole distribution and consequently polarization have to be identical. This means that each subcycle has to start and end at the same point (Fig. 3.12).

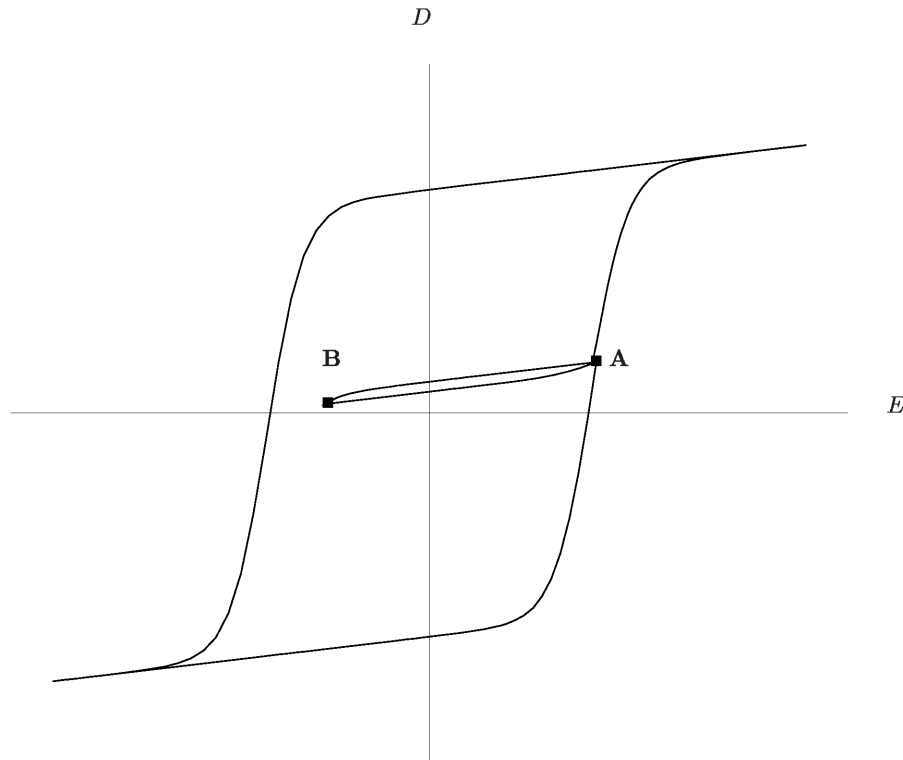


Figure 3.12: Minor loop

3.2.4 Memory Wipe Out

An interesting feature of ferroelectric or ferromagnetic materials is the effect of memory wipe out. This effect occurs if the amplitude of the electric field is increased again after several depolarization cycles have been performed. This is sketched in Fig. 3.13. Starting from negative saturation two subcycles with decreasing amplitude are applied until the operating point D is reached. As outlined in the previous subsection, the local subloop of the hysteresis has to hit the last turning point C. If the electric field still increases and finally gets higher than the last local maximum E_C , which is shown in the PE-diagram in Fig. 3.9, the PE-diagram will transform into the form outlined in Fig. 3.5. This is identical to the situation before the last subcycle CDC was applied to the material. This means that this subcycle has no influence on the future behavior of the material, so the hysteresis will proceed to operating point A, and, if the field is further increased, along the saturation loop.

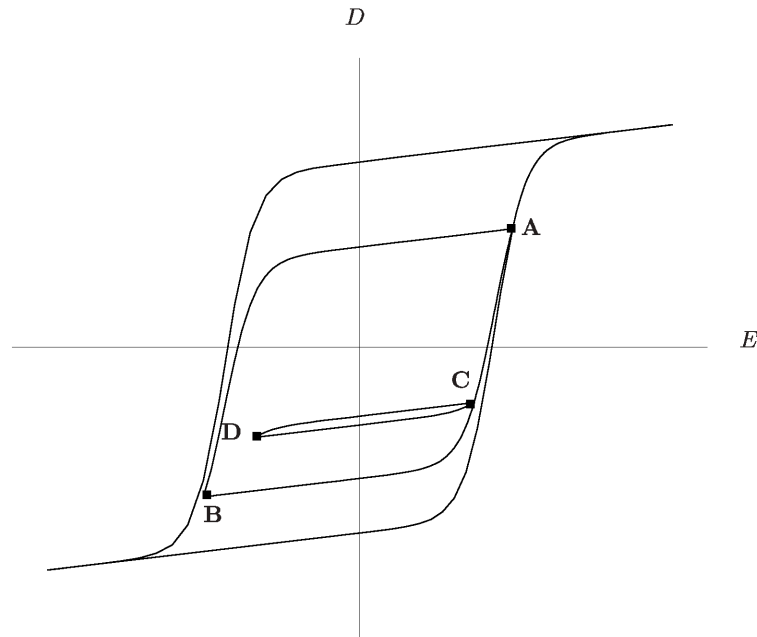


Figure 3.13: Memory wipe out

3.3 Lattice Models – Minimized Free Energy

The minimized free energy model concentrates on the double well structure of distorted perovskite structures. A one-dimensional lattice model was developed by Omura et al [OAI91], based on previous work on isomorphous ferroelectric phase transition by Ishibashi, which was published in 1992 [Ish92]. It relies on the minimization of the free energy which is modeled by a fourth order approach for the energy of the center ion stemming from the lattice cell and a coupling term describing the interaction between the ions of neighboring cells:

$$f = \sum_{n=1}^N \frac{\alpha}{2} \cdot p_n^2 + \frac{\beta}{4} \cdot p_n^4 + \frac{\kappa}{2} \cdot (p_n - p_{n-1})^2 - p_n \cdot E. \quad (3.5)$$

p_n is the dipole moment of the n th dipole, κ is the coupling coefficient. α is a function of the temperature, namely

$$\alpha = a \cdot (T - T_0), \quad a > 0. \quad (3.6)$$

T_0 is the Curie Temperature. Consequently

$$\alpha < 0 \quad (3.7)$$

is true for the ferroelectric phase of the material, and finally it is assumed that

$$\beta > 0. \quad (3.8)$$

The overall polarization is given by

$$P = \sum_{n=1}^N p_n. \quad (3.9)$$

The model assumes the existence of permanent dipoles with random distribution (Fig. 3.14). These dipoles serve as centers for the nucleation of domains.

The two allowed dipole moments are restricted by the model to $p_n \geq 1$ for the positive nuclei and $p_n \leq -1$ for the negative ones.

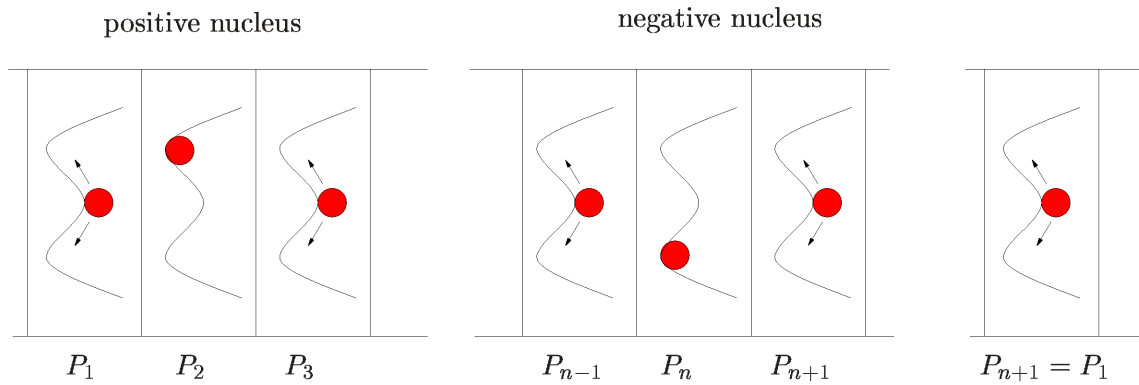


Figure 3.14: One-dimensional lattice model, atoms in the double minimum potential interact with their neighbors, cyclic boundary condition $p_1 = p_{n+1}$

The simulation starts at an equilibrium state where all the 'free' dipoles are negatively polarized and the time-dependent expansion of the domains that occurs around the nucleation centers is examined. Therefore a viscosity coefficient γ is introduced which takes into account the switching delay of the individual dipoles. The resulting evolution of polarization is given by the Landau Khalatnikov kinetic equation [Bau99]

$$\gamma \cdot \frac{dp_n}{dt} = -\frac{\partial f}{\partial p_n} \quad (3.10)$$

and finally with (3.5) as

$$\gamma \cdot \frac{dp_n}{dt} = -\{\alpha \cdot p_n + \beta \cdot p_n^3 - \kappa \cdot (p_{n+1} - 2 \cdot p_n + p_{n-1}) - E\}. \quad (3.11)$$

Simulation is carried out by application of a time dependent signal

$$E = f(t) \quad (3.12)$$

and numerical solution of the resulting set of (3.11). The typical shape of the resulting hysteresis is plotted in Fig. 3.15.

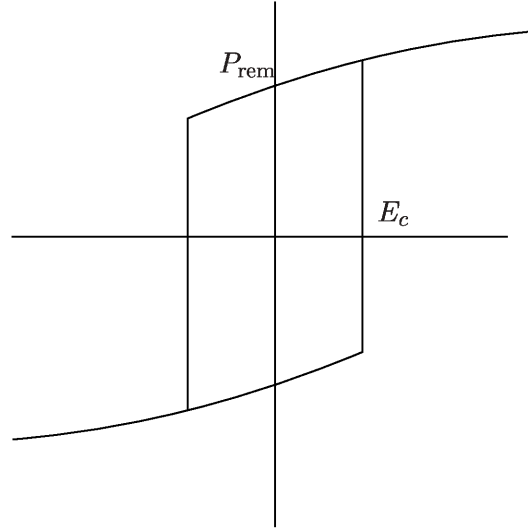


Figure 3.15: Hysteresis of the free energy model

This approach was extended to two-dimensional lattice structures by Omura et al. [OAI92] in 1992. The functional for the free energy had to be modified in order to include the increased number of possible coupling partners as follows

$$f = \sum_{m,n}^{M,N} \left\{ \frac{\alpha}{2} \cdot p_{m,n}^2 + \frac{\beta}{4} \cdot p_{m,n}^4 + \frac{\kappa_1}{2} \cdot (p_{m,n} - p_{m-1,n})^2 \right. \quad (3.13)$$

$$\left. + \frac{\kappa_2}{2} \cdot (p_{m,n} - p_{m,n-1})^2 + \frac{\kappa_1}{2} \cdot (p_{m,n} - p_{m-1,n-1})^2 - p_{m,n} \cdot E \right\}. \quad (3.14)$$

The Landau Khalatnikov equation reads then

$$\gamma \cdot \frac{dp_{m,n}}{dt} = - \frac{\partial f}{\partial p_{m,n}}. \quad (3.15)$$

This first approach did not consider the influence of the depolarization field. Instead the electric field was assumed to be constant in the entire simulation area. The influence of depolarization was finally added by Baudry in 1999 [Bau99], who implemented Poisson's equation into the system.

The basic intent of the free energy method is to gain insight into the material properties and the main focus is the correct qualitative reproduction of physical effects. Typical simulation setups analyze areas of a size of about 50×50 dipoles.

3.3.1 Lattice Models

Alternatively to the fourth order approach, there are more elaborate models for free energy and structural transitions [WR97], [RW95] which are therefore closer to the actual physical

properties, but are numerically even more expensive. This approach is used for the temperature dependent analysis of lattice structure and phase transitions.

3.4 Discussion of the Models

This section discusses the models introduced in this chapter with respect to their ability to meet the constraints of device simulation.

The use of ferroelectric materials in highly integrated circuits has a comparatively short history. Up to date no canonic device structure has been found and the designs are in a steady flow of modifications. One goal of this thesis was to design a tool capable of dealing with the actual questions concerning ferroelectric devices, but also extendable for any future developments. This demands a real two-dimensional treatment of the ferroelectric properties.

The SPICE based approaches are very fast, but the weak point of the concept is its inflexibility. Any change of the shape of the hysteresis, e.g., requires the development of a different model circuit. Furthermore, analysis which includes any geometry dependence is far out of reach.

At first glance this also seems to be the case for the Preisach hysteresis, which would mean that only the lattice models would remain as objects for implementation. Unfortunately, this approach suffers from various disadvantages.

First, the numerical effort and the complexity of the problem are not related. For simple one-dimensional problems, e.g., a whole lattice of sufficient size has to be calculated, while a compact model only demands the solution of an analytic equation. Another drawback of the lattice method is that simulation of distorted lattices is only possible when an actual distortion or variation of the parameters is added to the equation set, which will increase the complexity of the simulation and, even more unpleasantly, the setup of the simulation input. In addition the properties of the impurities inside a device are not included in the default material data sheet. Thus when using this approach some distribution function of the coupling parameters would have to be fitted in order to reproduce any measured hysteresis loop. Obviously such behavior does not increase the appeal of the model for device simulation, especially considering the fact that the reproduction of any measured hysteresis loop does not need a lot of fitting effort if a compact model is used.

No principle difficulty, but also unpleasant is the fact that lattice models employ a specific numerical concept. It is possible to include their simulation approach into a two-dimensional device simulator, but the different numerical concept will lead to very long simulation times, as the equation system for the ferroelectric material will have to be solved decoupledly from the semiconductor equations.

More appropriate for device simulation is a model that combines the speed of a compact model for simple tasks with the ability to calculate general two-dimensional problems and uses the same numerical concept as state-of-the-art device simulators, the box integration method. This can be achieved by application of an extended two-dimensional compact model to the material equations of the device simulator. Consequently, the Preisach hysteresis

Approach	Numerical effort	Arbitrary structures	Necessary Device Data
Compact model	low	no	Hysteresis
2-d Compact Model	moderate	yes	Hysteresis
Lattice Models	high	yes	Double well structure, impurities

Table 3.1: Comparison between different simulation approaches

model, being the most accurate compact model, was selected for the implementation into the device simulator MINIMOS-NT.

Chapter 4

Two-Dimensional Simulation

MINIMOS-NT is a generic device simulator that uses the box integration method. Therefore it was necessary to adapt the Preisach hysteresis model, which is outlined in Section 3.2, in such a way that it fulfills the requirements of this numerical method. As already outlined in Section 3.4, the material is supposed to comply with the Preisach hysteresis in any local point, and the resulting field equations have to be solved.

The flux equation used for the box integration method is the third Maxwell equation [Max91]:

$$\operatorname{div} \vec{D} = \rho \quad (4.1)$$

Hysteresis is modeled with the material equation (2.1), which can be separated into a linear part and a nonlinear part. The nonlinear part P_{Ferro} which is responsible for the hysteresis, is modeled by the Preisach hysteresis. Considering the fact that a different locus curve has to be calculated for each box boundary, it is necessary to choose an analytic function for the calculation of the hysteresis, thus replacing the integral of the distribution function (3.4). Functions of the general form

$$P = k \cdot f(E \pm E_c, k) + P_{\text{off}} \quad (4.2)$$

can easily be applied where the function f serves as the shape function of the hysteresis. If $P_{\text{off}} = 0$ and $k = 1$, f will be one branch of the saturation loop. Through modification of the parameters k and P_{off} all the possible locus curves of the hysteresis can be simulated. E_c is the coercive field of the polarization.

As can easily be seen, (4.1) is a vector equation and (4.2) is a scalar equation. Several algorithms had to be developed for the extraction of \vec{D} out of D , each depending on a specific task. They will be described in Section 4.2.

4.1 Shape Functions

To this day two different types of the shape function f have been implemented into the simulator, the tanh and the arctan function.

4.1.1 The arctan Shape Function

The arctan function covers the physical properties of SBT($\text{SrBi}_2\text{Ta}_2\text{O}_9$) in a very accurate way [DBL98]:

$$P = \frac{2}{\pi} \cdot k \cdot P_{\text{Sat}} \cdot \arctan\left(2 \cdot (E \pm E_c) \cdot \frac{k}{w}\right) + P_{\text{off}} \quad (4.3)$$

w is the shape parameter necessary to match the remanent polarization P_{Rem} . k and P_{off} are used for the simulation of subcycles. For the calculation of these parameters the equation system

$$\begin{aligned} P_{\text{old}} &= \frac{2}{\pi} \cdot k \cdot P_{\text{Sat}} \cdot \arctan\left(2 \cdot (E_{\text{old}} \pm E_c) \cdot \frac{k}{w}\right) + P_{\text{off}} \\ P_{\text{turn}} &= \frac{2}{\pi} \cdot k \cdot P_{\text{Sat}} \cdot \arctan\left(2 \cdot (E_{\text{turn}} \pm E_c) \cdot \frac{k}{w}\right) + P_{\text{off}} \end{aligned} \quad (4.4)$$

has to be solved. As this equation system cannot be solved analytically, a Newton procedure is applied [Dir86]. This leads, if compared to the tanh shape function (4.1.2), to a slight increase of computation time and more sophisticated numerical problems.

4.1.2 The tanh Shape Function

Although this type, contrarily to the arctan shape function, allows the analytic calculation of the subcycle parameters k and P_{off} , it provides a less accurate fit, especially for low voltages [UGH⁺99]. The implementation of this function, as introduced by Jiang et al. [JZJ⁺97], is

$$P = k \cdot P_{\text{Sat}} \cdot \tanh\left(w \cdot (E \pm E_c)\right) + P_{\text{off}}. \quad (4.5)$$

The resulting equation system reads as

$$\begin{aligned} P_{\text{old}} &= k \cdot P_{\text{Sat}} \cdot \tanh\left(w \cdot (E_{\text{old}} \pm E_c)\right) + P_{\text{off}} \\ P_{\text{turn}} &= k \cdot P_{\text{Sat}} \cdot \tanh\left(w \cdot (E_{\text{turn}} \pm E_c)\right) + P_{\text{off}}. \end{aligned} \quad (4.6)$$

For the calculation of the subcycle two different sets of equations are obtained, depending on whether an initial polarization cycle is calculated or not. In the case of an initial cycle the turning point has the values

$$\begin{aligned} P_{\text{turn}} &= P_{\text{Sat}} \\ E_{\text{turn}} &= \infty. \end{aligned} \quad (4.7)$$

Consequently, the parameters for the locus curves are

$$k = \frac{P_{\text{old}} - P_{\text{Sat}}}{P_{\text{Sat}} \cdot (\tanh(w \cdot (E_{\text{old}} - E_c)) - 1)} \quad (4.8)$$

$$P_{\text{off}} = P_{\text{Sat}} \cdot (k - 1) \quad (4.9)$$

if the electric field increases, and

$$k = \frac{P_{\text{old}} + P_{\text{Sat}}}{P_{\text{Sat}} \cdot (\tanh(w \cdot (E_{\text{old}} + E_c) + 1))} \quad (4.10)$$

$$P_{\text{off}} = P_{\text{Sat}} \cdot (k - 1) \quad (4.11)$$

if the electric field decreases. In general the parameters for the subcycles are calculated as

$$k = \frac{P_{\text{old}} - P_{\text{turn}}}{P_{\text{Sat}} \cdot (\tanh(w \cdot (E_{\text{old}} \pm E_c)) - \tanh(w \cdot (E_{\text{turn}} \pm E_c)))} \quad (4.12)$$

$$P_{\text{off}} = P_{\text{turn}} - k \cdot P_{\text{Sat}} \cdot \tanh(w \cdot (E_{\text{turn}} \pm E_c)). \quad (4.13)$$

The signs depend on whether the electric field strength increases or decreases.

4.1.3 Comparison between the Shape Functions

As already mentioned above, the arctan function provides a more accurate fit for the physical properties, but is numerically more expensive. In order to compare the shapes of the two different functions, they are plotted in such a way that they appear as similar as possible, as Fig. 4.1 shows. The coercive field is kept constant and the shape parameter w is manipulated in order to minimize the average deviation.

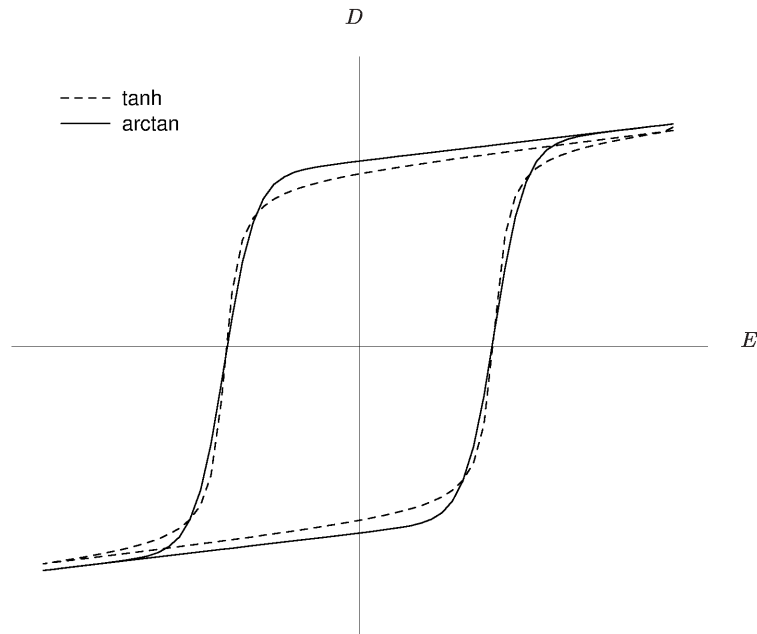


Figure 4.1: Comparison of the arctan and the tanh shape function

4.2 Two-Dimensional Algorithm

As outlined above, an algorithm has to be found which allows the reduction of the two-dimensional Poisson equation to a set of scalar equations.

4.2.1 Two-Dimensional Properties

The two-dimensional properties of hysteretic materials are more complex than they seem at first glance. The fact that the electric field might not only change its magnitude but also its orientation increases the complexity. These properties appear in form of a lag angle α between the electric field and the displacement. This effect was discovered as early as 1908 by Weiss and Planer [WP08].

So far this phenomenon has been studied only in the context of magnetism, where it is responsible for an additional energy loss [Pfü94]. For the simulation of large scale integration devices energy loss is of comparatively minor significance, but an accurate calculation of the orientations of the electric field and the displacement field is mandatory.

4.2.2 Single Crystals – Polycrystals

As can easily be deduced from the introduction of the ferroelectric properties, presented in Chapter 2, single crystals are anisotropic. Depending on the number and location of the energy minima in the lattice, there are either one or two axes of anisotropy. The schematic overview of these states is given in Fig. 4.2 and Fig. 4.3 for a material with two axes of anisotropy.

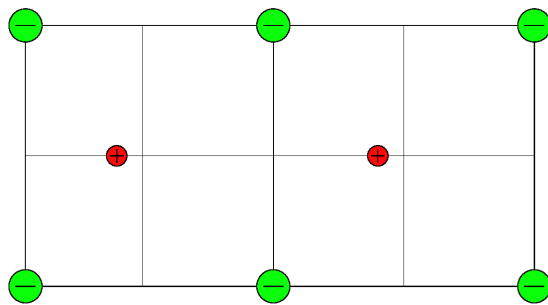


Figure 4.2: Location of the center ion, first axis of anisotropy

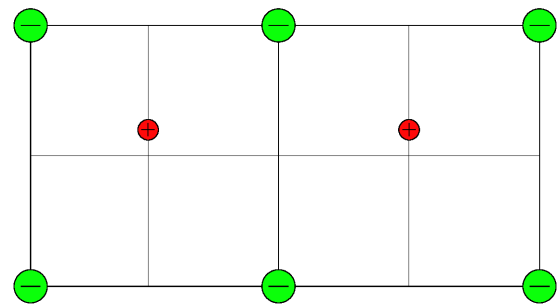


Figure 4.3: Location of the center ion, second axis of anisotropy

If the size of the single crystals is small compared to the dimensions of the device and their orientation is random, the material will lose its anisotropic properties. Of course this case can be simulated by a setup consisting of several anisotropic single crystals, but one should keep in mind that the obtained results will be valid just for this unique configuration which might or might not be representative. In this case an approach that does not depend on the direction is quite useful. In order to keep the generic approach of the simulator, models for both of these cases were developed.

4.2.3 Polarization in an Orthogonal Direction

The basic key for developing a rigorous approach to two-dimensional hysteresis is to find a useful formulation for the following problem: A piece of ferroelectric material has a remanent polarization \vec{P}_{Rem} , as sketched in Fig. 4.4. Then an electric field is applied in the perpendicular direction.

The newly applied electric field will raise a polarization component P_{\parallel} in the same direction as the field. This is plotted in Fig. 4.5.

Regarding the fact that there was no prior polarization in this direction, an initial polarization curve (dashed line) is used. The finite number of dipoles introduces the saturation polarization as a hard limit. Regarding the domain structure of the material and neglecting the rotation of the dipoles, it can be assumed that the sum of magnitudes of the newly raised and the remanent component will not exceed the saturation polarization P_{Sat} .

$$\|\vec{P}_{\text{Rem}}\| + \|\vec{P}_{\parallel}\| \leq P_{\text{Sat}} \quad (4.14)$$

For the model presented in this thesis the component $\|\vec{P}_{\text{Rem}}\|$ will be reduced in order to fulfill (4.14), due to the fact that there is no field component in this direction. The resulting polarization is plotted in Fig. 4.6.

Even in the case that (4.14) does not fulfill the exact physical properties, there has to be a similar, more general expression the form of:

$$\|\vec{P}_{\text{Rem}}\| + \|\vec{P}_{\parallel}\| \leq f(\|\vec{E}\|). \quad (4.15)$$

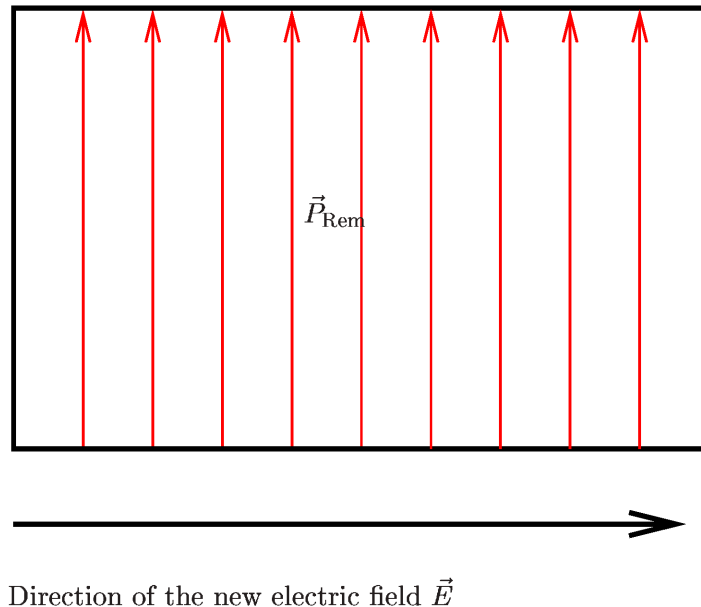


Figure 4.4: Application of an electric field orthogonal to the remanent polarization

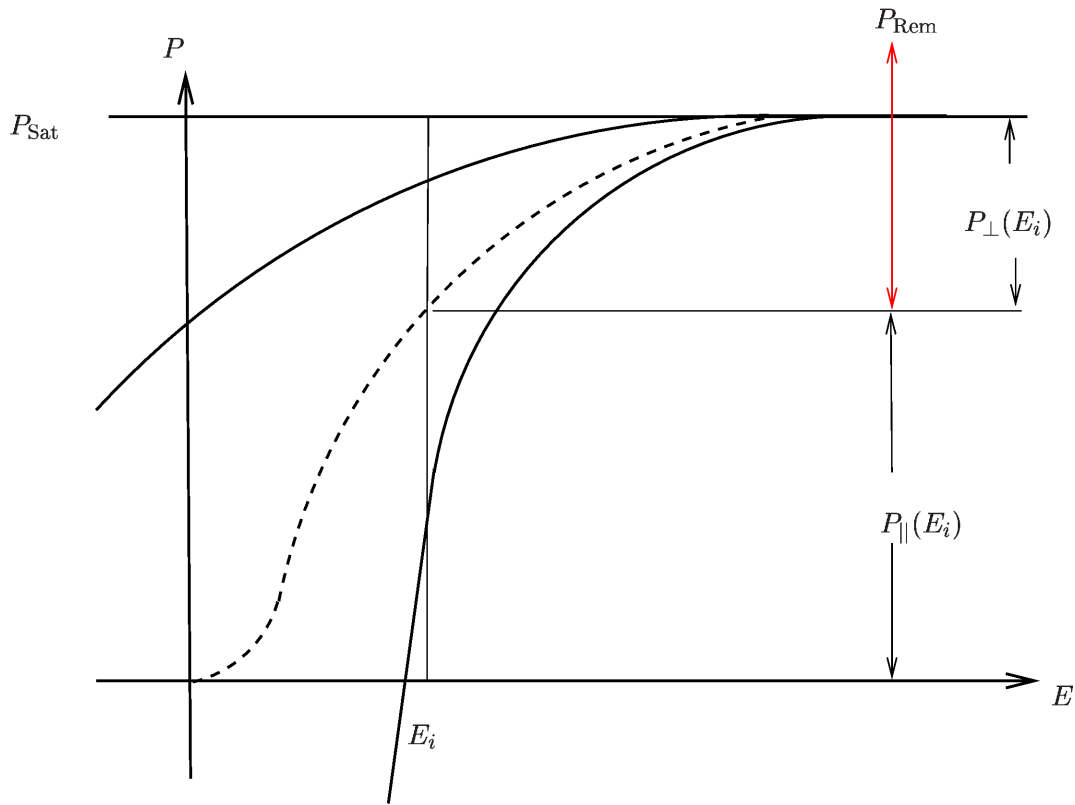


Figure 4.5: Construction of the polarization components

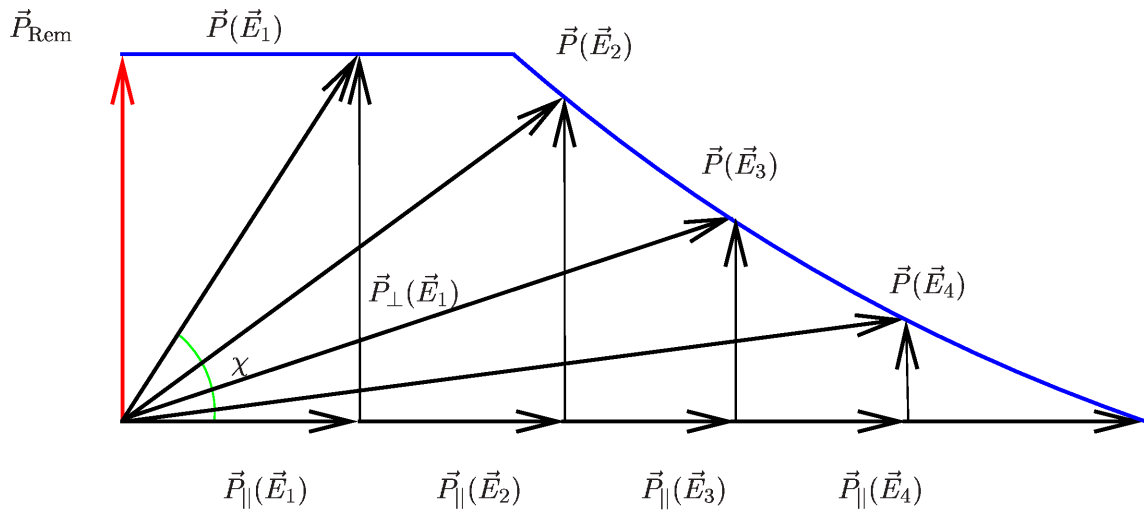


Figure 4.6: Construction of the lag angle

4.2.4 Algorithm for Anisotropic Materials

Basically, there are two different reasons for including anisotropy into a TCAD tool for ferroelectric materials. First, the ferroelectric materials show strong anisotropy and inclusion of it will meet the physics in an accurate way, thus allowing a deeper insight into the properties inside the device. Second, the ever decreasing device geometries and the thin film thicknesses lead to a regime where anisotropy cannot be neglected.

Satisfying this generic approach, the new algorithm is capable of dealing with materials with one or two anisotropy axes with arbitrary orientations. For the first basic steps of anisotropy simulation all dipoles are assumed to be oriented in one of the anisotropy axes.

Since rotation processes which might occur at high fields are neglected, the dipoles have to switch between the anisotropy axes. Furthermore it is presumed that the number of dipoles and domains is still big enough that they do not influence the macroscopic field properties.

Uniaxial Materials

This is the simplest approach for two-dimensional simulation. The only important quantity necessary to obtain the polarization is the strength of the electric field in the direction \vec{X} of the anisotropy axis:

$$P = f(\vec{E} \cdot \vec{X}). \quad (4.16)$$

Thus the polarization vector reads as

$$\vec{P} = f(\vec{E} \cdot \vec{X}) \cdot \vec{X}. \quad (4.17)$$

Biaxial Materials

Simulation of more than one anisotropy axis requires a sophisticated simulation approach. As outlined above, the dipoles have to be oriented in the axes directions, but they are not bound to a particular direction. This means that transitions between all of the four states outlined in Fig. 4.2 and Fig. 4.3 are possible.

Nevertheless it has to be taken into consideration that the number of dipoles is finite, which sets a hard limit to the sum of the polarization components of all the axes directions. When this limit is reached, the polarization components have to be reduced correspondingly. This is done following the ratio between the polarizations in the respective directions. The implemented algorithm is outlined in Fig. 4.7.

4.2.5 Algorithm for Materials without any Favored Direction

As already mentioned, grain sizes of ferroelectric ceramics can get as small as 10nm. This means that in many cases we do not deal with ideal monocrystals but with structures formed by several grains. The orientations of these grains are not easy to find. As outlined above, the

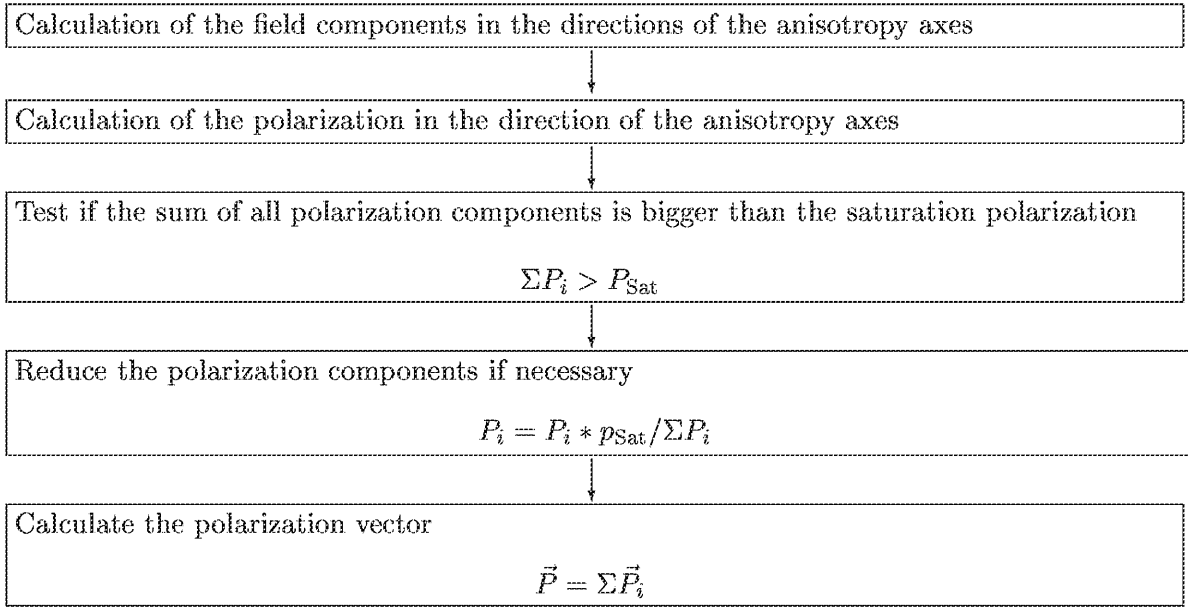


Figure 4.7: Algorithm for materials with more than one axis of anisotropy

material as a whole shows uniform and, due to the randomly spread orientations, isotropic properties.

Following the ideas outlined in the previous section, the basic principle of this model is to split the polarization \vec{P}_{old} and the electric field \vec{E}_{old} of the previous operating point into components in the direction of the next applied electric field \vec{E}_1 , resulting in

$$\vec{P}_{\text{old},\parallel} = \vec{P}_{\text{old}} \cdot \vec{E}_1 \cdot \frac{\vec{E}_1}{\|\vec{E}_1\|} \quad (4.18)$$

$$\vec{E}_{\text{old},\parallel} = \vec{E}_{\text{old}} \cdot \vec{E}_1 \cdot \frac{\vec{E}_1}{\|\vec{E}_1\|} \quad (4.19)$$

as well as

$$\vec{P}_{\text{old},\perp} = \vec{P}_{\text{old}} \cdot \vec{E}_{1,\perp} \cdot \frac{\vec{E}_{1,\perp}}{\|\vec{E}_{1,\perp}\|} \quad (4.20)$$

$$\vec{E}_{\text{old},\perp} = \vec{E}_{\text{old}} \cdot \vec{E}_{1,\perp} \cdot \frac{\vec{E}_{1,\perp}}{\|\vec{E}_{1,\perp}\|} \quad (4.21)$$

in the orthogonal direction

$$\vec{E}_{1,\perp} = \begin{pmatrix} \vec{E}_{1,y} \\ -\vec{E}_{1,x} \end{pmatrix}, \quad (4.22)$$

which is graphically outlined in Fig. 4.8.

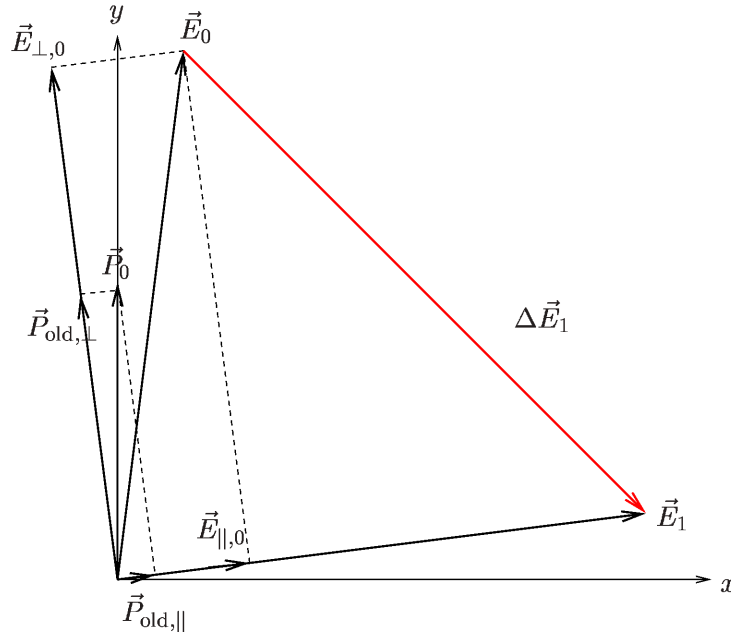


Figure 4.8: Splitting of the field vectors

With these geometric operations, the two-dimensional problem gets reduced to two one-dimensional scalar problems, with the additional advantage that this geometric approach also works in three dimensions. Now the concept of Preisach hysteresis, outlined in the previous chapter, can be applied to each of these scalar problems.

For a general approach to two-dimensional hysteresis effects an inhomogeneous field distribution has to be assumed. This prevents the usage of a simple one-dimensional hysteresis model which would use an identical locus curve for the complete ferroelectric region. According to the algorithm presented above, two different locus curves $f_{loc,||}$ and $f_{loc,\perp}$ have to be calculated for each grid point. These are outlined in Fig. 4.9.

According to the Preisach model, the parameters w and k of the locus curves are calculated using the projections of the old directions of the old electric field $\vec{E}_{old,||}$, $\vec{E}_{old,\perp}$, the old polarization field $\vec{P}_{old,||}$, $\vec{P}_{old,\perp}$, and the turning points $\vec{P}_{turn,||}$, $\vec{P}_{turn,\perp}$.

The component $P_{||,1}$ in the direction of the electric field is calculated by entering the signed length of the electric field vector into the equation of the local locus curve f_{local}

$$P_{||,1} = f_{loc,||}(\pm \|\vec{E}_1\|). \quad (4.23)$$

The actual algorithm required to achieve the signed length $\pm \|\vec{E}_1\|$ quantity will be discussed in Section 6.2.2. The input for the locus curve is, according to geometrical properties, zero in the perpendicular direction. Thus with the component

$$P_{1,\perp,init} = f_{loc,\perp}(0) \quad (4.24)$$

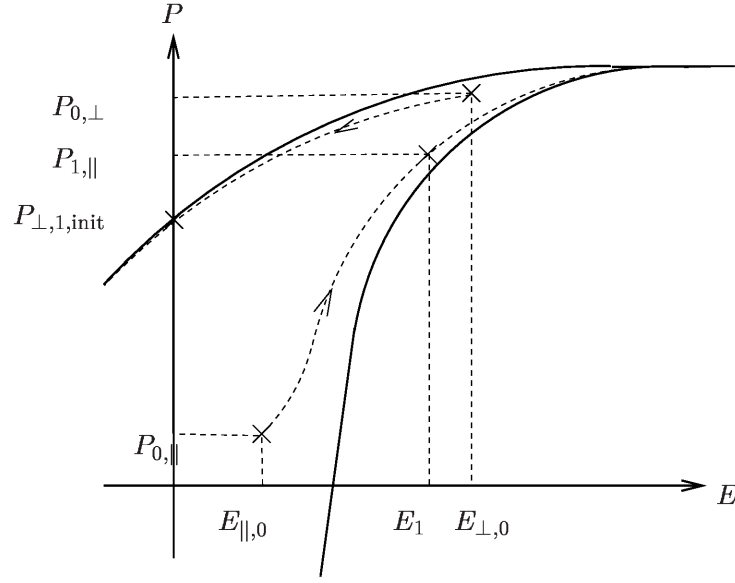


Figure 4.9: Calculation of the initial guess

the polarization in the perpendicular direction is obtained. The two polarization components, which were given in (4.23) and (4.24), constitute an initial guess

$$\vec{P}_{\text{init}} = P_{\parallel,1} \cdot \frac{\vec{E}_{1,\parallel}}{\|\vec{E}_{1,\parallel}\|} + P_{\perp,1,\text{init}} \frac{\vec{E}_{1,\perp}}{\|\vec{E}_{1,\perp}\|} \quad (4.25)$$

for the next polarization which is plotted in Fig. 4.10.

Following the model for the polarization in perpendicular direction, outlined in Section 4.2.3, the scalar values of the two components are added and compared to the saturation polarization P_{Sat} .

The vanishing electric field in the perpendicular direction makes it easier to switch the dipoles which are oriented in this direction than to switch the dipoles which are oriented in the direction of the electric field and, consequently, hold by it. The perpendicular component \vec{P}_{\perp} is reduced appropriately with respect to the limit

$$\|P_{\perp}\| = P_{\text{Sat}} - \|P_{\parallel,1}\|. \quad (4.26)$$

This is shown schematically in Fig. 4.10 and Fig. 4.11 and leads to the actual polarization vector

$$\vec{P}_1 = \vec{P}_{\parallel,1} + \|P_{\perp}\| \cdot \frac{\vec{P}_{\perp,1}}{\|\vec{P}_{\perp,1}\|}. \quad (4.27)$$

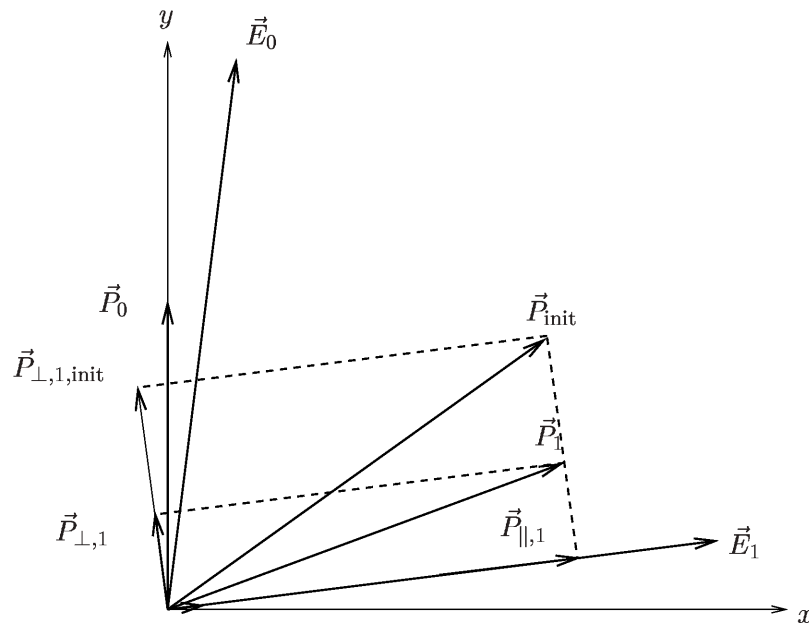


Figure 4.10: Calculation of the polarization

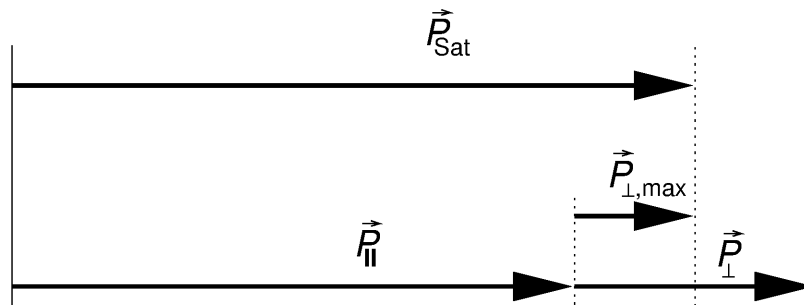


Figure 4.11: Reduction of the orthogonal component

4.2.6 Comparison of the Two-Dimensional Approaches

Obviously, simulation of more than one anisotropy axis will increase memory consumption. The entire history of the material has to be stored for each of the axis directions.

The reduction of one two-dimensional problem to several one-dimensional ones usually shows better convergence behavior for anisotropy simulation.

4.2.7 Simple, One-Dimensional Model

If the device geometry and the field distributions are one-dimensional, like it is the case for planar capacitors, a simplified model can be applied. This model takes advantage from the

fact that the resulting electric field will be perpendicular to the contacts and, if an orthogonal grid is applied for discretization, to the box boundaries. If this is the case, the polarization can be calculated using the electric field strength in the direction perpendicular to the box boundary only, thus reducing the numerical effort significantly.

4.3 Comparison of the Two-Dimensional Model to Measurements

A key question for the simulation model is whether it is justified to ignore the existence of domains and to treat the material as a continuum. Indeed, experimental data for PZT directly deposited on Ti/Pt electrodes show a dependence of ferroelectric properties on the thickness of the film, thus questioning this approach. These difficulties were solved by the assumption of a non-ferroelectric blocking layer (Fig. 4.12) at the interface of the contact electrodes.

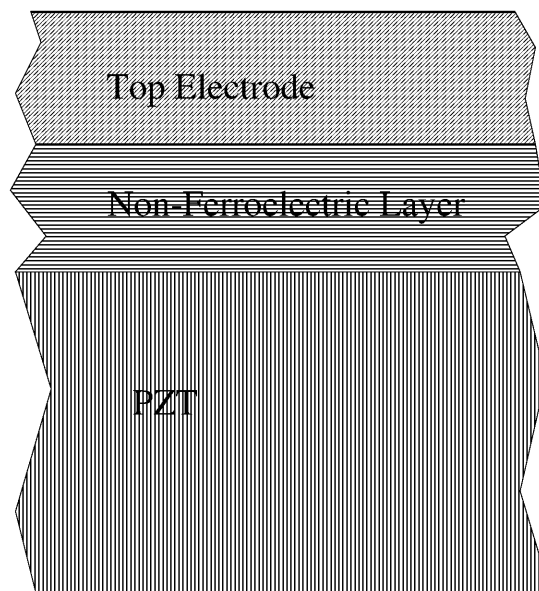


Figure 4.12: Non-ferroelectric blocking layer

Thus good correspondence of the measured data to the continuum approach was obtained [LDTvV94]. These calculations were carried out using a one-dimensional continuum model. The decisive parameter for the blocking layer is the ratio between its relative dielectric constant ϵ_{bl} and its thickness d_{bl} . The reported, specimen dependent, values of ϵ_{bl}/d_{bl} are $20\text{-}30\text{nm}^{-1}$.

Later experiments with $\text{La}_{0.5}\text{Sr}_{0.5}\text{CoO}_3$ electrodes immediately matched the expected predictions of linear scaling of field properties [CPW97], thus giving further evidence that the model is appropriate.

Chapter 5

Frequency Dependent Simulation

LIKE ALL dielectrics, the permittivity of ferroelectrics shows a distinct frequency dependence. Typical clock frequencies of integrated circuits have long entered a regime where the frequency dependence of basic material parameters like coercive field and remanent polarization can no longer be neglected. At high frequencies hysteresis widens and the coercive field increases, which is of fundamental interest for the extraction of parameters for write- and read-cycles like applied voltage or pulse length.

5.1 Modeling

For precise simulation a model was developed which allows the analysis of the transient behavior. Simulation in the frequency domain, simulation through simple modification of the hysteresis parameters might be numerically less complex, but will lead to reduced capabilities in comparison with the time domain. Especially in the context of arbitrarily shaped signals and relaxation effects an approach in the time domain is mandatory.

Depending on the concept several different approaches are commonly used. As already outlined in Section 3.2, frequency dependence can be added to compact models by the introduction of additional RC circuits. Other approaches calculate the change of direction of the dipoles with the help of field dependent transition probabilities [TAH⁺97], or, the speed of domain wall movement, if the focus lies on the analysis of material properties [Ish92][Sco95].

According to the concept of the device simulator MINIMOS-NT, an analytic model based on differential equations was developed. A common approach for the frequency dependence of linear dielectric materials [Fas87] was extended. The approach started out from the static, nonlinear equation

$$P_{\text{stat}} = f(E(t)). \quad (5.1)$$

Next a transient term was added to the electric field

$$E(t) = E_{\text{stat}} + \tau_{\text{ef}} \cdot \frac{dE}{dt}, \quad (5.2)$$

where E_{stat} is the static component of the electric field and τ_{ef} a material dependent time constant. Then the actual electric field is calculated and entered into (5.1), thus forming the first term for the transient equation

$$P_{\text{ef}} = f(E(t)). \quad (5.3)$$

Basically, this term shifts the hysteresis curves and increases the coercive field. Still following the approach for linear materials, a transient term stemming from the change of the polarization

$$P_{\text{pol}} = -\tau_{\text{pol}} \cdot \frac{dP}{dt} \quad (5.4)$$

is added. Again τ_{pol} is a time constant. In addition to increasing the coercive field, this term also flattens the hysteresis.

Experimental data show that these two terms can be adapted into the physical properties in a limited range of frequencies only. In order to improve this, a third term, which represents the nonlinearity of the material,

$$P_{\text{nonlin}} = s_h \cdot k_{\text{nonlin}} \cdot (P - P_{\text{ef}}) \cdot \frac{dE(t)}{dt}, \quad (5.5)$$

is added, resulting in

$$P = P_{\text{ef}} + P_{\text{pol}} + P_{\text{nonlin}}. \quad (5.6)$$

s_h is a sign flag indicating whether the electric field is increased or decreased. k_{nonlin} is a material dependent coefficient. This term appears to be a good fit and also allows also a physical interpretation as it increases with the distance between the polarization component stemming from the electric field and the actual polarization.

5.2 Discretization

Both transient equations (5.2) and (5.6) are discretized with a forward Euler scheme, which guarantees reasonable stability.

Discretization of (5.2) leads to

$$E_1 = E_{\text{stat}} + \tau_{\text{ef}} \cdot \frac{E_1 - E_0}{t_1 - t_0}. \quad (5.7)$$

All the terms with the index 1 are related to the new time step, the ones with the index 0 to the old time step. By applying simple mathematics one gets

$$E_1 = \frac{E_{\text{stat}} + \tau_{\text{ef}} \cdot E_0}{1 + \tau_{\text{ef}}} \quad (5.8)$$

for the explicit form. Similarly (5.6) reads as

$$P_1 = P_{\text{stat}} - \tau_{\text{pol}} \cdot \frac{P_1 - P_0}{t_1 - t_0} + s_h \cdot k_{\text{nonlin}} \cdot (P - P_{\text{ef}}) \cdot \frac{E_1 - E_0}{t_1 - t_0} \quad (5.9)$$

and the explicit equation as

$$P_1 = \frac{P_{\text{stat}} + \tilde{c} \cdot P_0}{1 + \tilde{c}}, \tilde{c} = \frac{\tau_{\text{pol}}}{1 + s_h \cdot k_{\text{nonlin}} \cdot \frac{E_1 - E_0}{t_1 - t_0}}. \quad (5.10)$$

5.3 Comparison to Measurement

The extraction of time- and material-parameters is a very sensitive task for successful transient simulation. In the context of this work, these parameters have been extracted for two different specimen of PZT, which were produced by two different industrial suppliers.

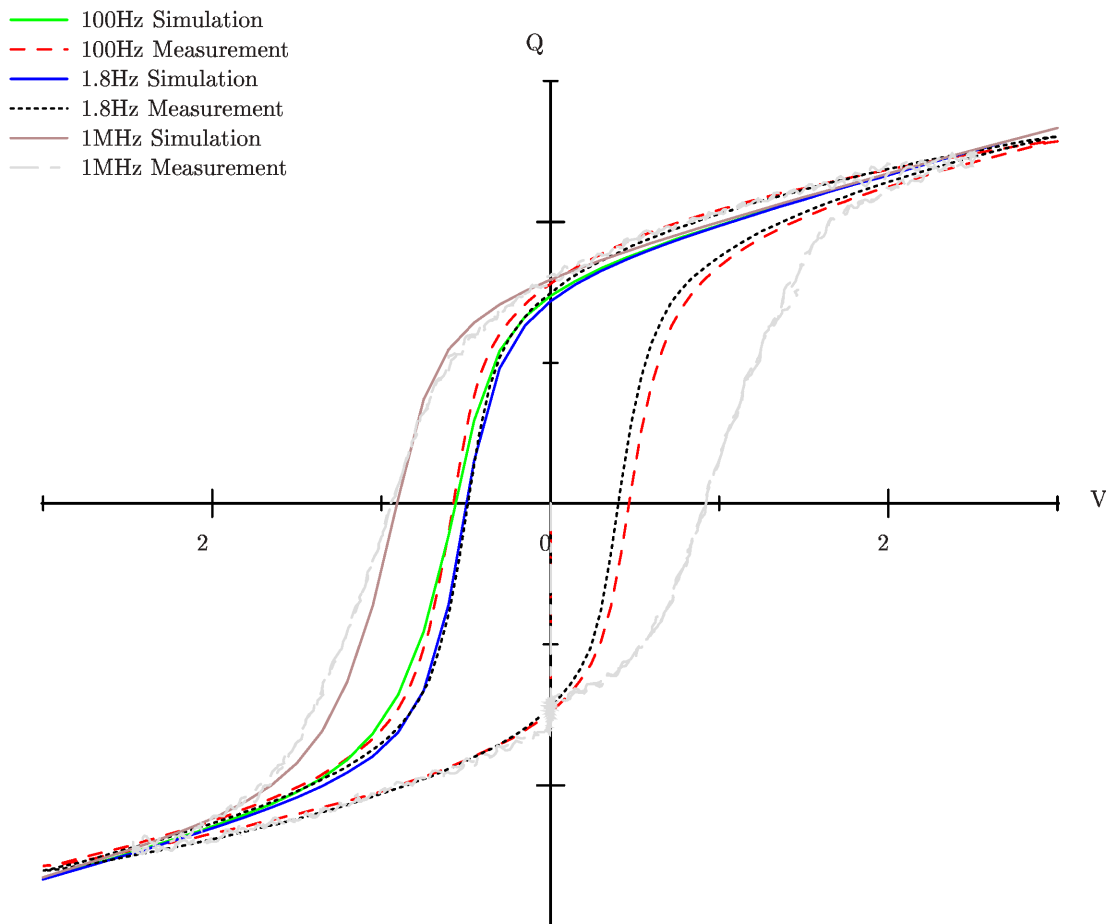


Figure 5.1: Comparison simulation to measurement, Supplier 1

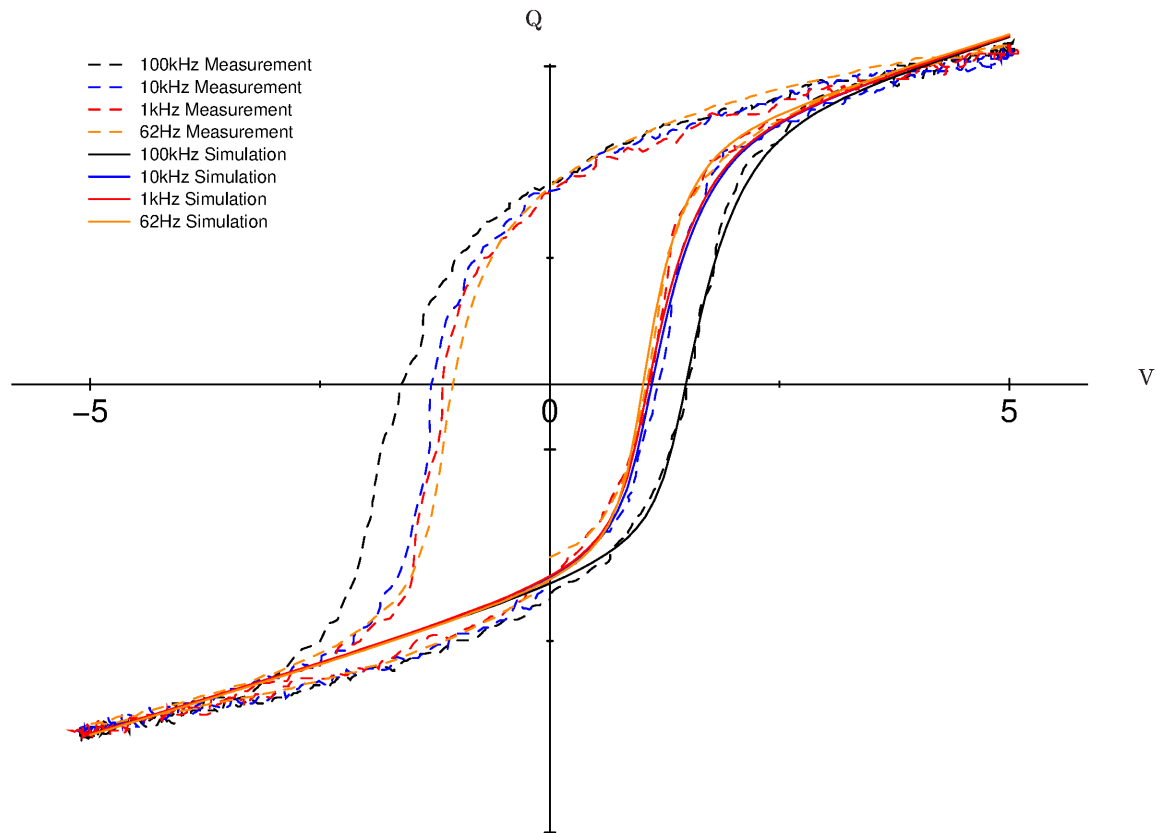


Figure 5.2: Comparison simulation to measurement, Supplier 2

For both materials similar values for the material parameters were found, and a good fit between the simulated and the measured Q/V characteristics was obtained. These Q/V characteristics are plotted in Fig. 5.1 and Fig. 5.2.

In both figures full cycles of the measured hysteresis curve are plotted in dashed lines. A close analysis of the data shows that the up loop and the down loop do not show a perfect symmetry. This is related to non ideal material properties which can be introduced into the simulator by application of two different sets of hysteresis parameters for the respective direction. As this is of minor relevance for the analysis of frequency dependence, the investigations were focused on one out of these two branches.

The measured data available for the second specimen covered the complete frequency range up to 100kHz, without any gap. This allows the extraction and analysis of the frequency dependence of decisive material properties like coercive field and remanent polarization. The coercive field is of highest importance for the device performance, as it specifies the strength of the field necessary to change the information inside the device and thus the supply voltage. Fig. 5.3 compares the prediction of the simulation with the measured values. The measured data are plotted point by point, the simulation results in a straight line. At higher frequencies

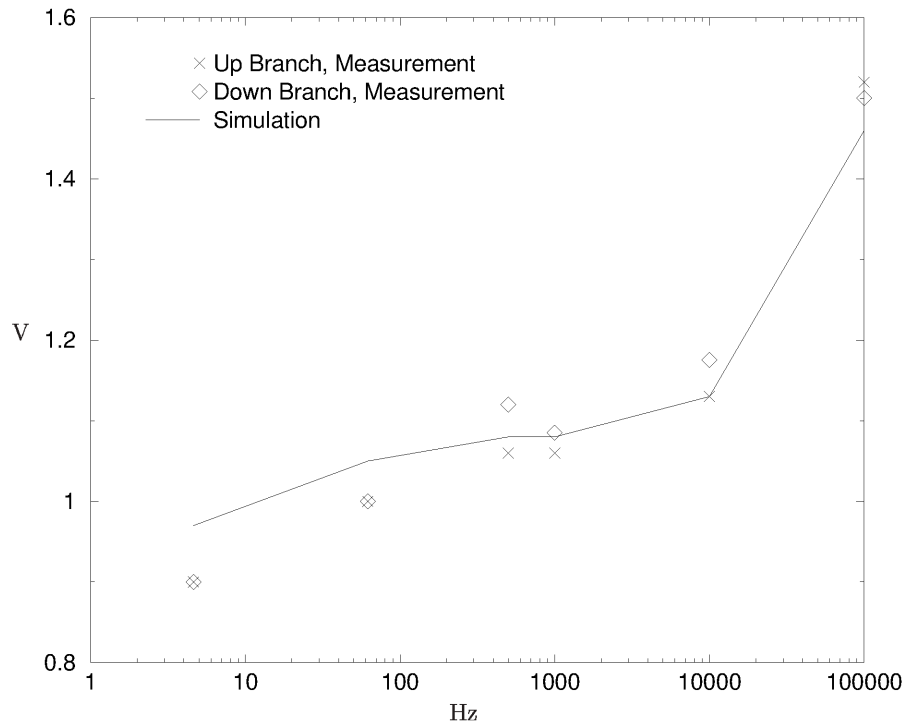


Figure 5.3: Comparison simulation to measurement, coercive field

the coercive fields in the up and down direction show a significant discrepancy, therefore both values are plotted.

5.4 Extraction of the Parameters

The fact that ferroelectric hysteresis is definitely nonlinear makes the extraction of the material parameters rather difficult, as the transient terms are very sensitive since they depend on the derivatives of the hysteresis. Furthermore, useful data are not easy to obtain, since high frequency measurements on ferroelectrics are still extremely unreliable. In addition the presented model is new and no prior knowledge on the parameter values can be used.

As a first step in order to extract these material parameters, an applicable algorithm which adapts the simulated data to the measured data had to be developed. Fig. 5.4 outlines the most promising out of various tested algorithms.

With this algorithm the parameters used for the simulations in the previous Section were extracted. The fact that similar values of the parameters are obtained for both materials is a good indicator for the reliability of the transient model. The parameter set obtained for sample two was used for all subsequent calculations.

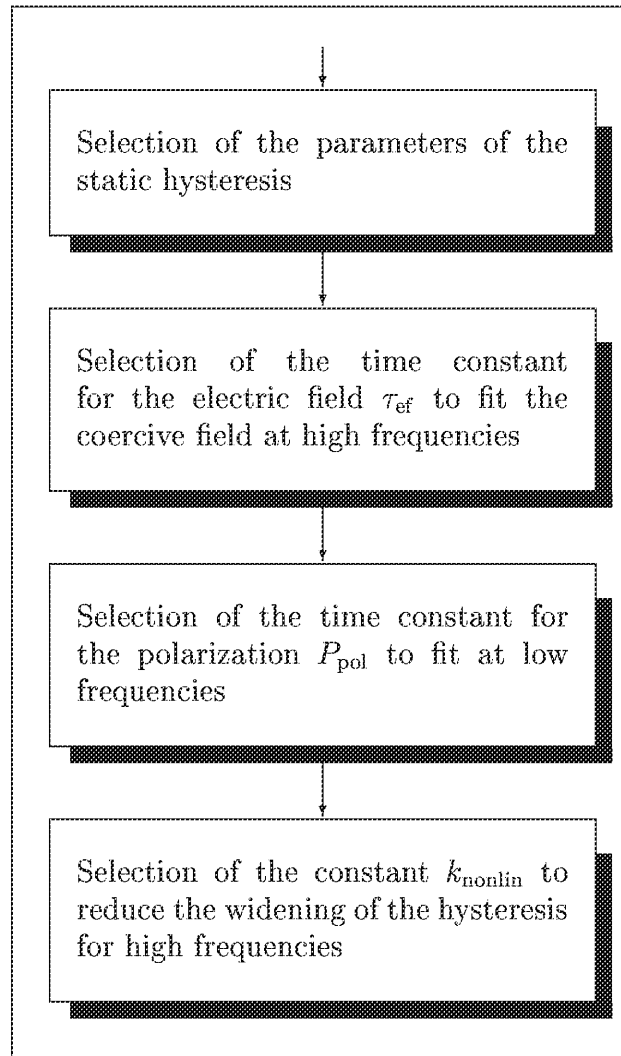


Figure 5.4: Algorithm to fit the parameters

5.5 Analysis of Signal Response

From the viewpoint of communication engineering, a ferroelectric capacitor is a nonlinear and, as a consequence of hysteresis, time variant system. Consequently, standard approaches for the analysis of signal response in linear time invariant (LTI) systems cannot be applied. Instead a more detailed analysis of the properties is necessary. Actually, any signal response shows a strong dependence on shape, amplitude and frequency of the input signal.

5.5.1 Frequency and Amplitude Dependence of the Coercive Field

The analysis of the frequency and amplitude dependence of the coercive field provides an introduction to the complexity of response properties. A triangular signal is applied to a

ferroelectric capacitor. The parameter set used is extracted from the measurements outlined in Fig. 5.1. Depending on the amplitude of the input signal, different ratios between frequency and coercive field are obtained (Fig. 5.5). The most obvious nonlinear effect in the plotted area is that, due to hysteresis, the coercive field does not grow linearly if the applied amplitude is increased.

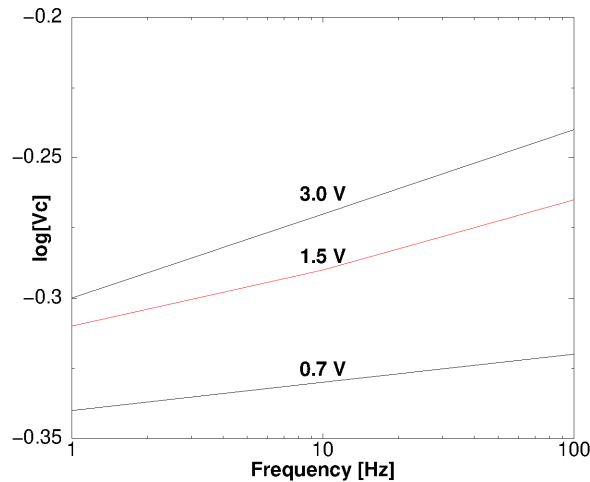


Figure 5.5: Coercive voltage as a function of frequency and peak voltage

5.5.2 Pulse Shape and Amplitude

The derivative of the static hysteresis curve has a distinct maximum near the coercive field and a minimum at saturation. Accordingly, the transient effects caused by the related transient term (5.4) show similar properties.

Consequently the response will depend on the pulse shape. The different hysteresis curves obtained for sinusoidal and triangular pulses are plotted in Fig. 5.6 and Fig. 5.7. A comparison between these two plots shows two systematic differences

- The coercive field increases much faster when sinusoidal pulses are applied.
- The hysteresis loop shows a higher tendency to close when triangular pulses are applied.

The first of these two effects is caused by the higher derivative of the sinusoidal input signal at 0V, which increases the related transient term (5.3).

The second effect is related to the fact that sinusoidal pulses remain near their amplitude for a comparatively longer period. This leads to an increased relaxation, as the derivative of the static hysteresis curve has a distinct minimum near saturation, which minimizes transient effects caused by the related transient term (5.4).

This behavior can clearly be seen in Fig. 5.8, which shows the results obtained for a series of sinusoidal pulses with different amplitudes at a fixed frequency of 1MHz. As expected, field

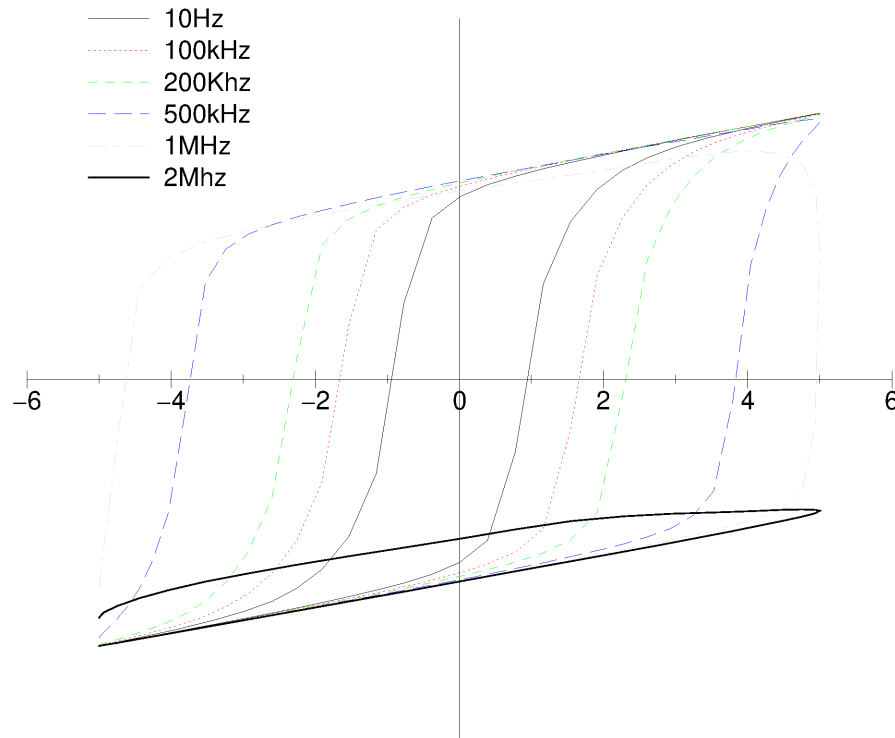


Figure 5.6: Signal response as function of frequency, sinusoidal pulse

reversal occurs near the turning point, where the term (5.4) has its minimum, independently of the amplitude.

5.5.3 Switching of a Capacitor

With the new model, the analysis of ferroelectric memory cells for arbitrary variation of the contact voltage is possible. This analysis is performed for a capacitor which is based on the material of supplier 2, the respective set of parameters is used. Fig. 5.9 shows the current and the charge as functions of time when a voltage step is applied to a capacitor, Fig. 5.10 shows these quantities for a triangular signal with included delay.

Especially in the first of these two figures the behavior of the ferroelectric material leads to a significant difference to a linear dielectric. The dipole relaxation does not follow an exponential function as might have been expected, and the maximum current does not appear immediately after the voltage step. As a consequence of (5.2), the electric field inside the device cannot change immediately, so the entire hysteresis curve has to be swept during the relaxation period, which causes the unexpected smoothness of the charge characteristics and the shift of the maximum current to the right.

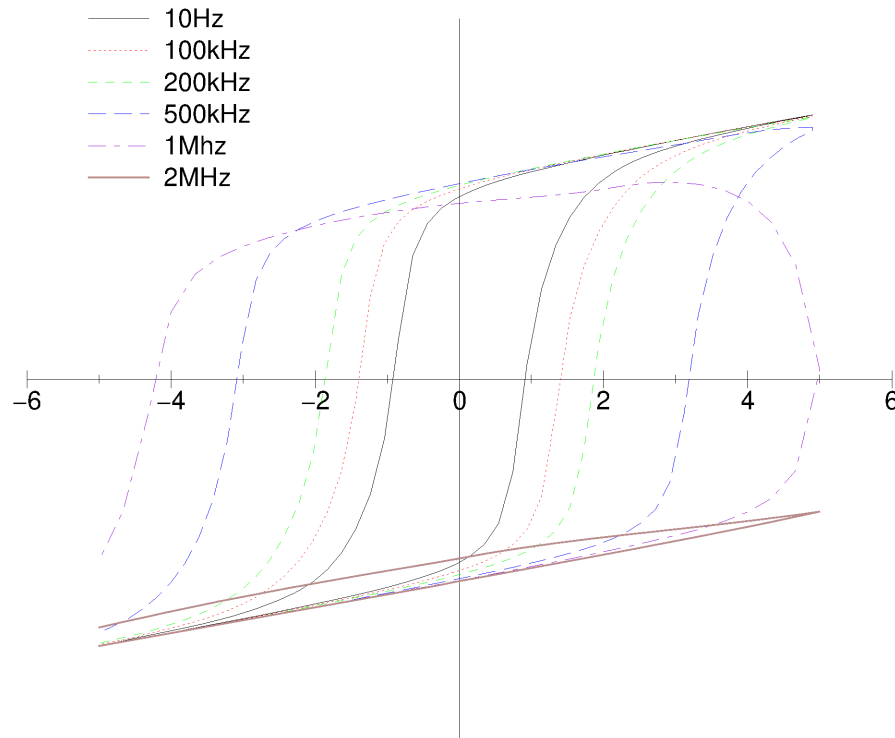


Figure 5.7: Signal response as function of frequency, triangular pulse

5.6 Measurement of Frequency Dependence

To the day of this writing no tools have been available which allow a direct extraction of the ferroelectric hysteresis for frequencies higher than 1000 Hz. The standard technique for high-frequency measurements is the Sawyer-Tower circuit [MNS⁺90] which is schematically outlined in Fig. 5.11.

In order to produce the high-frequency input signal $V_i(t)$, a function generator is used. The circuit itself consists of the ferroelectric capacitor C_F and a series capacitor C_S . The voltage between these two is evaluated with a digitizer.

For an exact equivalent circuit the series resistance of R_F and the input impedance R_i of the digitizer have to be considered. R_F is preferably quite high, reasonable values are in the range of 1000M Ω . The typical value for the input impedance R_i is 1M Ω .

MINIMOS-NT allows the simulation of small circuits consisting of discretized and concentrated devices, including the Sawyer-Tower circuit. As the simulation is performed in the time domain, also the initial oscillation of the circuit is obtained. Depending on the initial state of the ferroelectric capacitor and the ratio of the resistances, these oscillations can lead to a significant offset of the output voltage V_{Out} , and as outlined in Fig. 5.13 several cycles might be necessary until the hysteresis loop gets symmetrical.

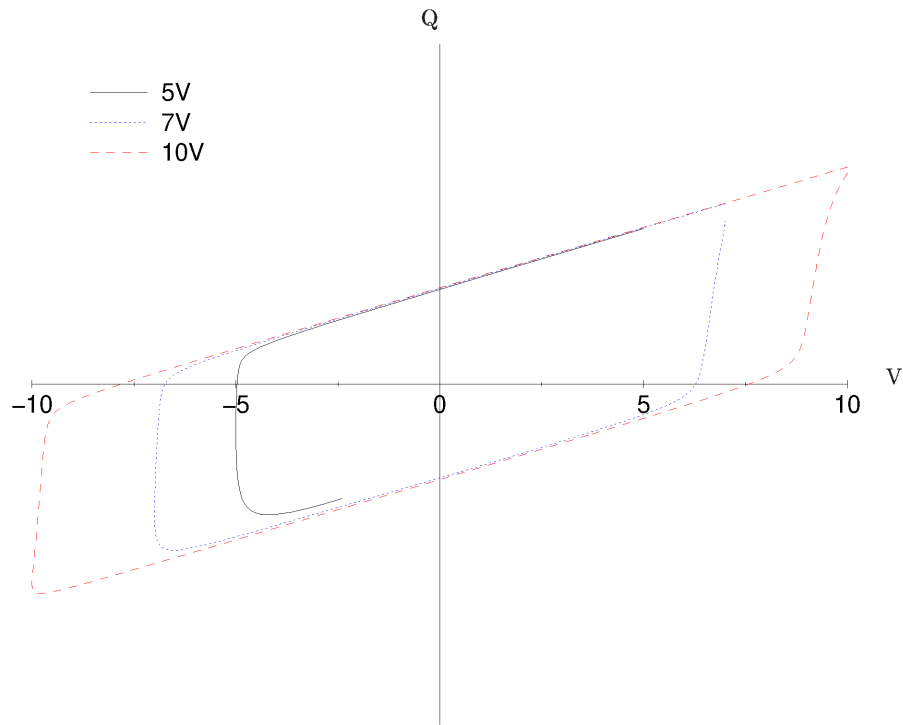


Figure 5.8: Signal response as function of amplitude, sinusoidal input with 1MHz

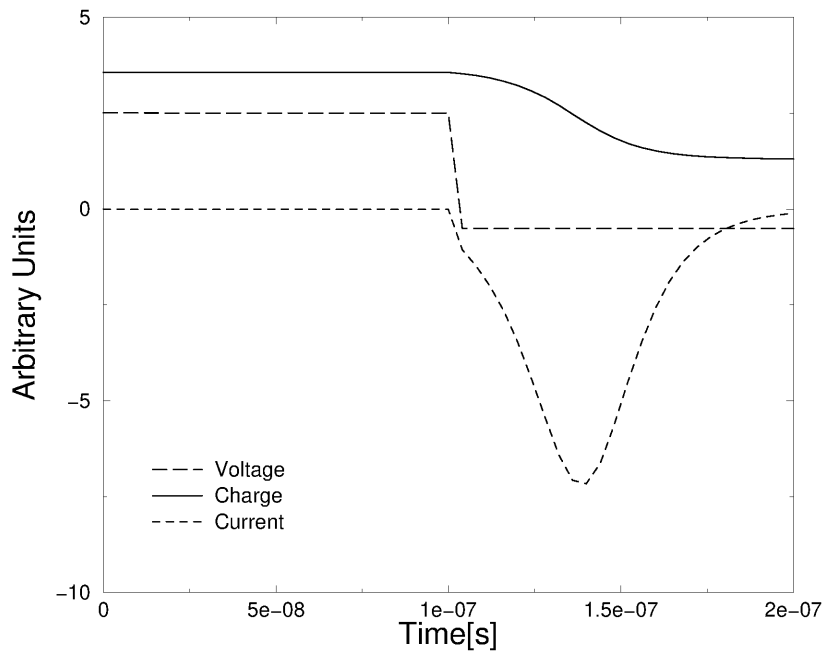


Figure 5.9: Charge and current response of a voltage step

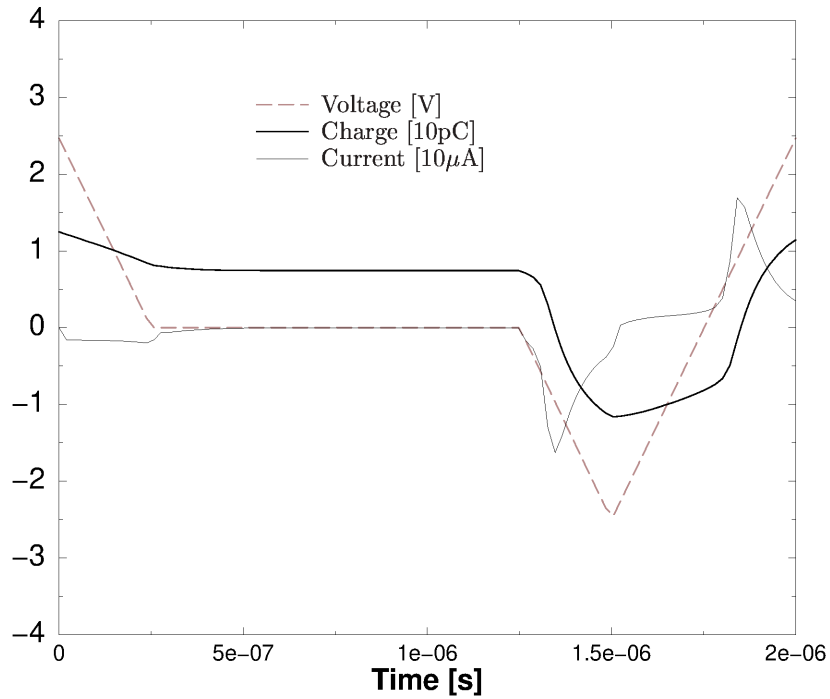


Figure 5.10: Charge and current response of a transient simulation

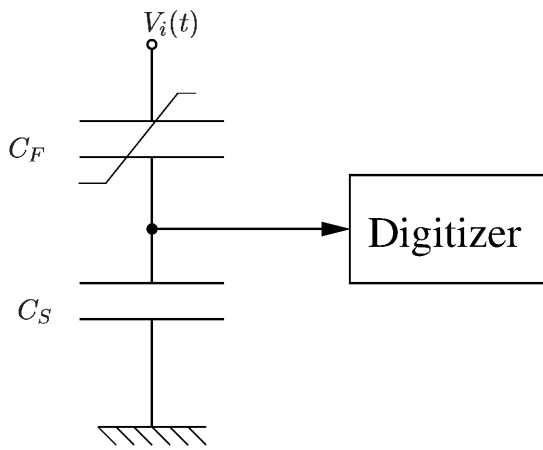


Figure 5.11: Sawyer-Tower circuit

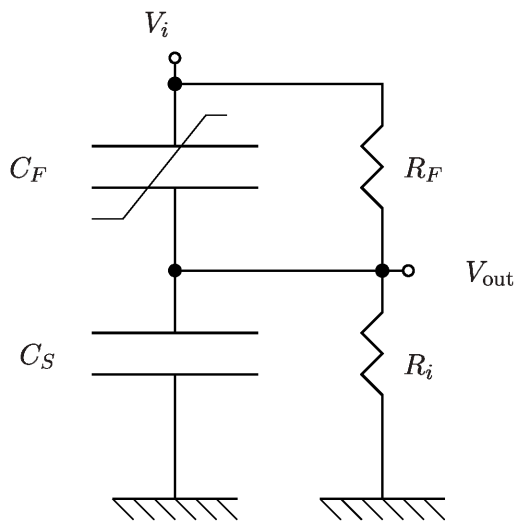


Figure 5.12: Equivalent circuit diagram

Unfortunately, the Sawyer-Tower circuit does not reproduce the exact properties. Prior measurements show that if the series resistance applied is too high, the output will be heavily distorted.

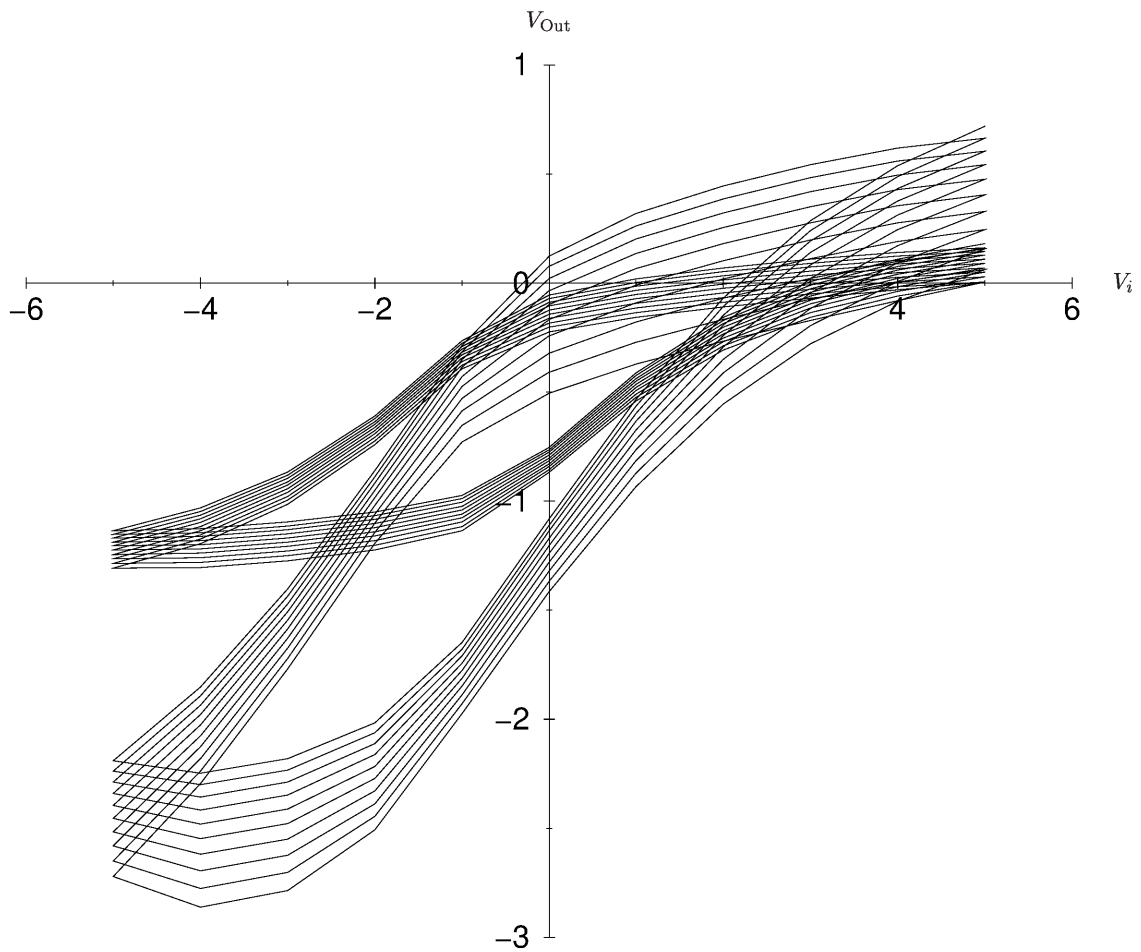


Figure 5.13: Initial oscillations of the Sawyer-Tower circuit for different ratios of the resistors

Fig. 5.14 gives the results obtained by simulations which show a good correspondence to the reported measured data [MNS⁺90]. Also initial oscillations which occur until a stable curve is reached are included in the figure.

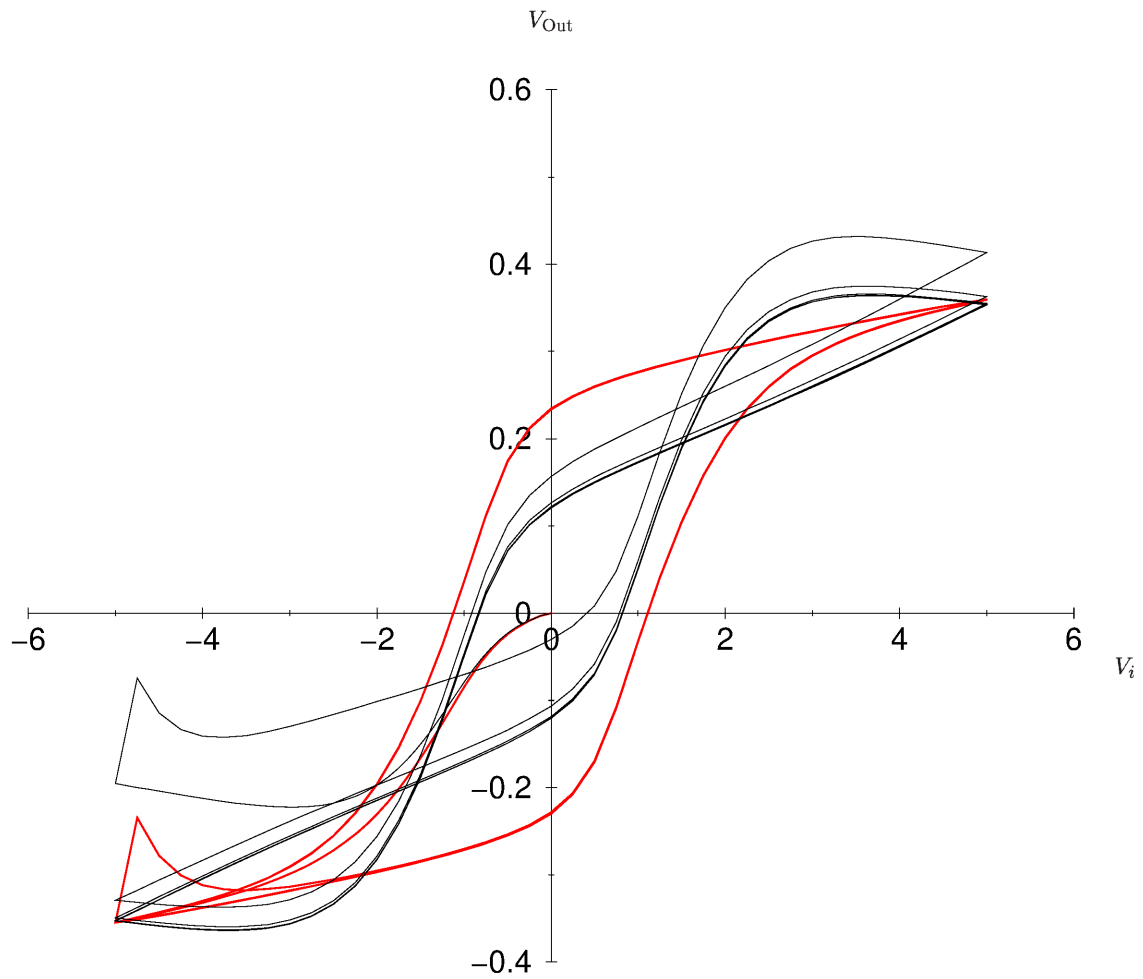


Figure 5.14: Distorted output signal

Chapter 6

Implementation

THE ALGORITHMS outlined in the previous sections were implemented into the device simulator MINIMOS-NT. Special care was taken in order to keep the implementation as modular as possible, so that later on an easy extension to the features that have not be entered into the simulator yet, like long time effects or temperature- and stress-dependence, can be applied.

The simulation passes through three different phases, starting with a preprocessor where the input data is evaluated and transformed into the internal data structure, the numerical calculations themselves, and a postprocessing where the internal data are transformed back to the output format required by the visualization tool and the contact quantities are calculated.

6.1 Preprocessing

The goal of this phase of the simulation is to provide the user with an interface. Also several calculations have to be carried out only once since their results do not depend on the system of partial differential equations which has to be solved numerically, and therefore it is convenient to include these here.

6.1.1 User Interface

The user interface of MINIMOS-NT consists of two different parts, one containing geometry and basic material properties like doping, the other one the control structure.

The control concept of MINIMOS-NT, the so called input deck [BDG⁺98], is very elaborate, which is especially useful for the development of any new code. This includes iteration schemes, damping schemes, several model parameters, arbitrary signal shapes for the input voltage and much more. The concept itself is modular and allows to hide well tested parameters from inexperienced users, thus securing easy handling.

Basically, three different types of input deck data can be distinguished:

- Control Parameters

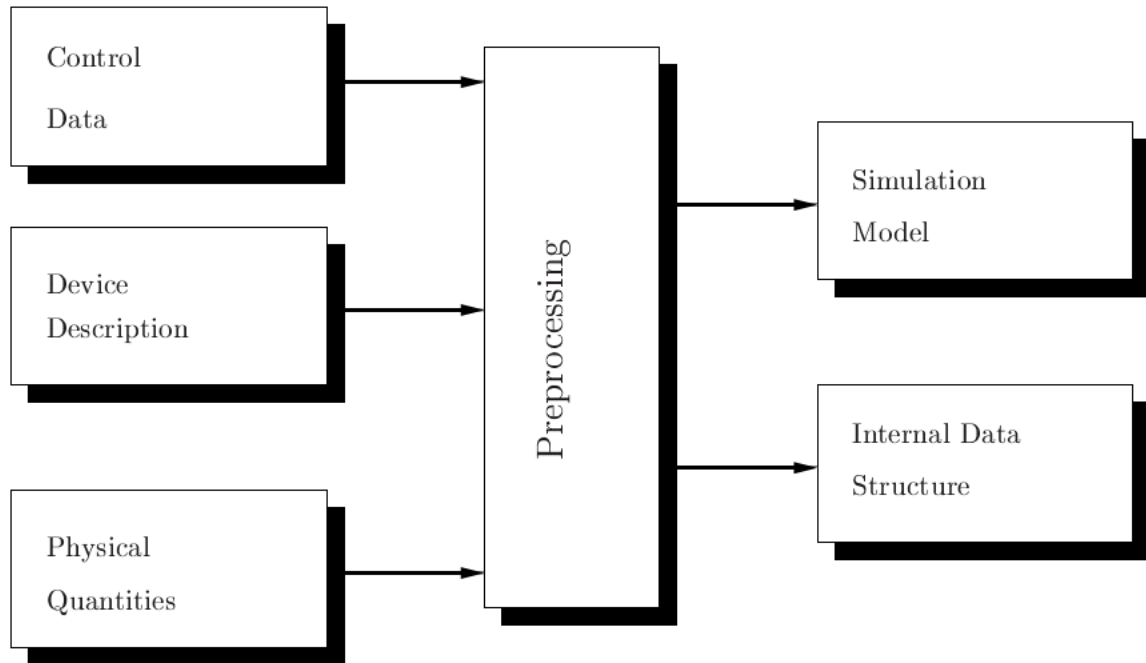


Figure 6.1: Schematic overview of preprocessing

- Device Description
- Physical Input Quantities

The resulting scheme is outlined in Fig. 6.1. A typical input deck for the simulation of ferroelectrics is plotted following this paragraph. It was used for the simulation of one of the hysteresis curves of Fig. 5.13. The first subsection of the inputdeck, the **Solve** section holds all the relevant information concerning the ferroelectric material, the respective keywords will be explained throughout this chapter. Since the geometry is split into different segments it has to be specified which of them contain ferroelectric materials. This is done in the **Phys** section.

```

#include <defaults.ipd>
Solve
{
  RelaxFerro = 8e9;
  RelaxFerroEf = 6.4e5;
  RelaxFerroExp = 0.6e8;
  ShapeFerro = 0.006;
  PsatFerro = 0.18;
  ECoercFerro = 165;
  FerroHysteresisModel = 1;
  AxesNumber = 1;
  FerroAxisI = 0;
  Anisotropy = no;
}
  
```

```

    Ferroid = yes;
    FerroTrans = yes;
    transient = yes;
    startTime = 0.0 s;
    endTime = 8e-5s;
    maxStepSize = endTime/800 ;
    minStepSize = maxStepSize ;
}
FCAP : DeviceDefaults
{
    Input { file = "pzt"; }
    Output {
        attributes = "";
        file = "pzt_out";
    }
    +LeftContact = 0.0 V;
    +RightContact = 0.0 V;
    Phys
    {
        ferro = "Insulator1";
        +Insulator1 { permittivity = "Pure";
        Permittivity
        {
            Pure
            {
                epsr = 400;
            }
        }
    }
    +LeftContact{ Contact { Ohmic { Ew = -0.55 eV; }}}
    +RightContact{ Contact { Ohmic { Ew = -0.55 eV; }}}
}
}
Iterate { Scheme : SchemeDefaults.DD_Ferro;}
Curve
{
    file = "mix_100khz";
    Response
    {
        +Vin = V("in");
        +VFCAP = V("A");
    }
}
Log
{
    deviceInfo = if ( yes, "*", "");
    iterationInfo = no;
}
Grid
{
    gridRefinement = 1.0;
}

```

```

IterateConfig
{
    maxDamp = 1.0;
    minDamp = 0.0000000008;
    iterationLimit = 350;
    iterationLimitStep = 150;

    finalNorm = 1e-5;
    transform = yes;
}
Num
{
    directSolver = yes;
}
Geometry
{
    deviceWidth = 1 um;
}
Circuit
{
R1 : ~Devices.R {N1 = "A" ; N2 ="gnd"; R = 1 MOhm; }
C1 : ~Devices.C {N1 = "gnd" ; N2 ="A"; C = 10nF; }
F : ~FCAP { RightContact = "in" ; LeftContact = "A" ;}
R2 : ~Devices.R { N1 = "in" ; N2 ="A" ; R = 10000 MOhm; }
Vin : ~Devices.V { P= "in"; M= "gnd";
    V0 = crv("contact_100khz.crv", "t", "Volt", ~Extern.t);}
}

```

Control Parameters

It is necessary to apply control parameters in order to define basic features of the simulator, e.g. which models have to be used, the iteration limits and so on. An overview of the part of the control concept dealing with the simulation of ferroelectrics is given in Fig. 6.2.

The keywords used for the simulation of ferroelectric materials are listed in Table 6.1.

Keyword	Values	Default
Ferroid	yes, no	no
Anisotropy	yes, no	no
FerroTrans	yes, no	no

Table 6.1: Control parameters

The keyword `Ferroid` functions as a switch which decides whether the simplified one-dimensional algorithm, outlined in Subsection 4.2.7 is applied or not. This keyword is set to `no` by default.

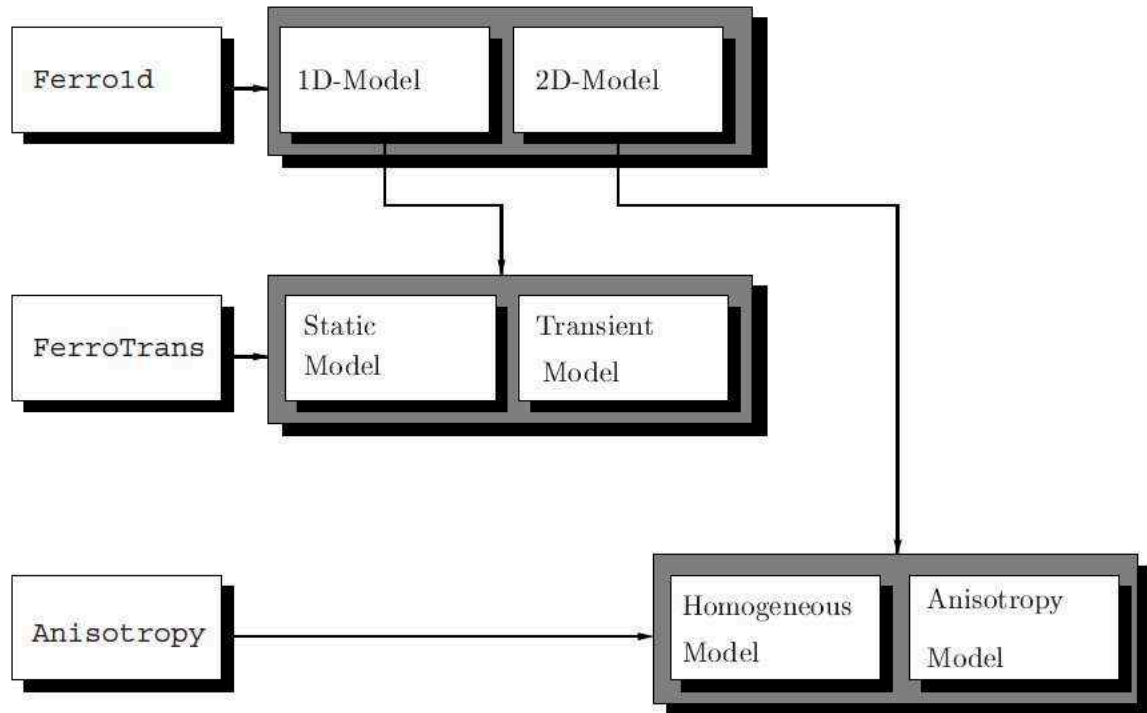


Figure 6.2: Control concept

The keyword `Anisotropy` distinguishes whether the model for anisotropy (value set to `yes`) or the model for homogeneous properties (value set to `no`) is used. This keyword is set to `no` by default.

The keyword `FerroTrans` distinguishes whether the transient model is used or not. This keyword is set to `no` by default.

Physical Input Quantities

In the `Device` sections of the input deck, contact quantities have to be added. By default the contact voltage is specified and the currents are calculated, but MINIMOS-NT also allows the calculation of the contact voltage when the current is specified and a mixed simulation where the current is specified on some contacts and the voltages on others. For transient simulations these quantities can be entered as functions of time.

Device Description

The device description consists of the geometry and a special list of keywords necessary for describing the properties of the ferroelectric material. An overview of these keywords and their default values is given in Table 6.2.

Keyword	Values	Default
PsatFerro	Real	0
ECoercFerro	Real	0
ShapeFerro	Real	0
FerroHysteresisModel	1,2	1
FerroAxesNumber	1,2	1
FerroAxisI	0...1	0
FerroAxisII	0...1	0
RelaxFerro	Real	0
RelaxFerroEf	Real	0
RelaxFerroExp	Real	0

Table 6.2: Device description

The geometry is stored in a separate file which is specified in the Input section of the input deck. In order to enter a ferroelectric material into the device, the command `ferro = segname` in the Phys section has to be added. The ferroelectric properties of the specified segment have to be declared in the Solve section. According to the implemented model, three parameters are necessary to describe the hysteresis: `PsatFerro` for the saturation polarization P_{Sat} , `ECoercFerro` for the coercive field E_c , `ShapeFerro` for the shape of the hysteresis. Using these parameters the remanent polarization P_{Rem} and the parameter w are calculated.

If the material is anisotropic, the axes properties are specified with the keyword `FerroHysteresisModel`. It is used to toggle between the different shape functions. If this keyword is set to 1 the tanh is selected, if set to 2, the arctan shape function is selected.

The number of axes is specified with the keyword `FerroAxesNumber`. Default is one. The keyword `FerroAxisI = 0...1` specifies the first anisotropy axis. The value entered is the cosinus of the angle to the x-axis, and default is zero. `FerroAxisII = 0...1` specifies the second axis. The value entered is defined the same way as for the first axis.

The three parameters for the transient simulation are :

`RelaxFerro`, the time constant for the polarization τ_{pol} , `RelaxFerroEf`, the time constant for the electric field τ_{ef} , and `RelaxFerroExp`, the value of the nonlinear parameter k_{nonlin} . All of these keywords are set to zero by default.

6.1.2 Calculations

As already outlined above, some calculations can be performed decoupledly from the system of differential equations.

A typical example for this type of calculations is the transformation of input data from SI units to internal units. The internal units are necessary in order to guarantee good numerical properties [Sch97].

Another task which can be fulfilled in the preprocessing unit concerns the hysteresis parameters: To allow an easy switch between the different types of shape function, a mapping function was implemented. Thus both functions are controlled with the same keyword `ShapeFerro`. If the \tanh shape function is used, the parameter remains unchanged,

$$w = \text{ShapeFerro}, \quad (6.1)$$

whereas for the \arctan function the parameter w is calculated in such a way that the remanent polarization P_{rem} is identical. This transformation reads

$$w = \tan\left(\pi \cdot \tanh(\text{ShapeFerro} \cdot E_c) \cdot 2\right). \quad (6.2)$$

Another typical task of preprocessing is the inclusion of models which take long term effects and temperature dependence into consideration. These topics are being heavily investigated today [GLB⁺98], and the extraction of useful models is expected in the near future.

Finally, an on-grid representation of the macroscopic device description of physical input quantities has to be calculated. The resulting data flow is outlined in Fig. 6.3.

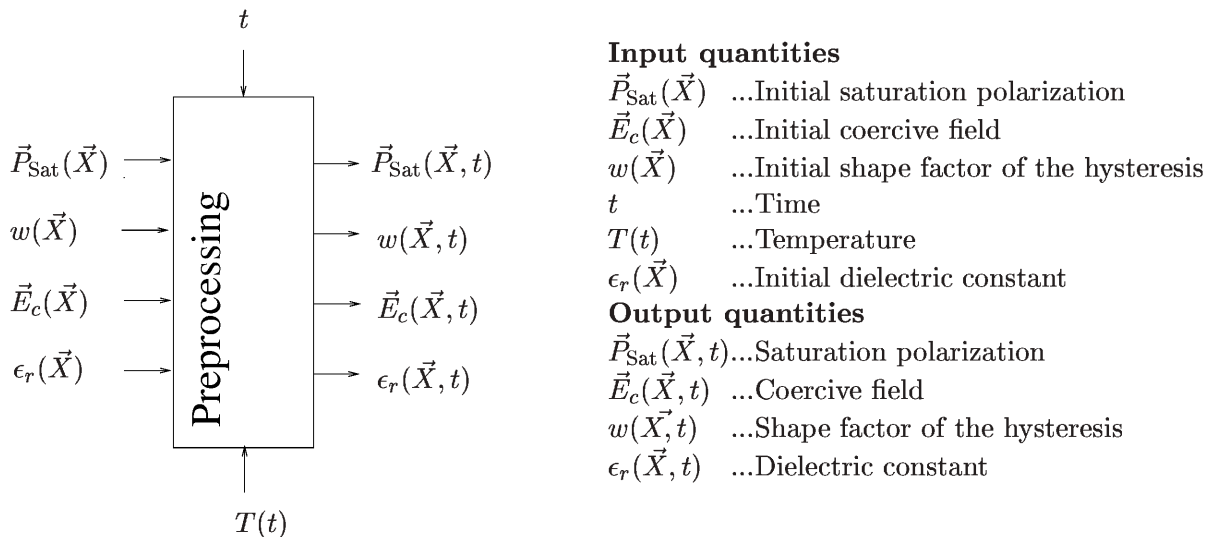


Figure 6.3: Data flow of preprocessing

6.2 Numerical Calculation

In this phase the equation sets concerning the models outlined in the previous chapters are collected and solved.

As a consequence of the general approach, the following numerical aspects have to be considered in order to allow a two-dimensional simulation with the box integration method:

- Discretization

- Memory management
- Nonsymmetry of the locus curves
- Influence of previous operating points
- Detection of the correct locus curve

6.2.1 Discretization

For the box integration method a flux vector has to be calculated at each box boundary. MINIMOS-NT offers an elegant approach where the vector quantities only have to be stored at the grid points and the resulting quantities at the boundaries are reconstructed [Fis94]. The electric field E_{ik} , e.g., which occurs at the boundary between the boxes i and k , is calculated using the following algorithm: The component perpendicular to the boundary $E_{ik,x}$ is calculated as the gradient of the potentials Φ_i and Φ_k ,

$$E_{ik,x} = (\Phi_i - \Phi_k)/d_{ik}, \quad (6.3)$$

where d_{ik} is the distance between the two grid points. The parallel component $E_{ik,y}$ is calculated in two steps. First, the electric fields \vec{E}_i and \vec{E}_k , which occur at the grid points, are calculated by a second order Taylor expansion with the potentials of all the neighboring gridpoints and the gridpoint itself as arguments [Fis94].

In order to get the correct representation at the boundary, a linear extrapolation between the parallel components of the neighboring electric fields \vec{E}_i and \vec{E}_k is performed,

$$E_{ik,y} = (\vec{E}_{i,y} - \vec{E}_{k,y})/2. \quad (6.4)$$

6.2.2 Nonsymmetry of the Locus Curves - Sign Handling

In contrast to most of the functions used in device simulation, the locus curves of hysteresis are nonsymmetrical functions of the applied electric field \vec{E} if $E_c \neq 0$. As will be shown in this Subsection, this leads to an increase of numerical complexity.

The straightforward scheme used to calculate the flux quantity of the box integration, the displacement \vec{D} would be

$$\vec{D} = f(\vec{E}) \rightarrow \vec{D} = f_{\text{scalar}}(\|\vec{E}\|) \cdot \frac{\vec{E}}{\|\vec{E}\|}. \quad (6.5)$$

f is the vector function describing the dependence between \vec{D} and \vec{E} , f_{scalar} is its scalar equivalent. Obviously this scheme has to fail, as it only allows positive arguments of the function f_{scalar} . A criterion has to be established which decides whether the argument of the function is treated as positive or negative, thus modifying f_{scalar} :

$$f_{\text{scalar}}(\|\vec{E}\|) \rightarrow f_{\text{scalar}}(\pm\|\vec{E}\|). \quad (6.6)$$

In order to achieve this, the direction of the field is compared of the with the box boundary. In local coordinates using the box boundary as y axis the criterion reads as

$$E_x \geq 0 \rightarrow +\|\vec{E}\| \quad (6.7)$$

$$E_x < 0 \rightarrow -\|\vec{E}\|. \quad (6.8)$$

In order to obtain the correct sign of the function argument also the term $\vec{E}/\|\vec{E}\|$ of (6.5) has to be modified, assuring that it always points to the same half-room. The complete discretization reads as

$$\vec{D} = f_{\text{scalar}}(\pm\|\vec{E}\|) \cdot \frac{\pm\vec{E}}{\|\vec{E}\|}, \quad (6.9)$$

where the sign in the last term is chosen accordingly to the rule defined in (6.7) and (6.8).

6.2.3 Detection of the Locus Curves

Calculating the locus curves for a new operating point is a sophisticated task. As outlined in Fig. 6.4, one of two possible locus curves has to be chosen at each operating point, depending on the history of the electric field [JZJ⁺97].

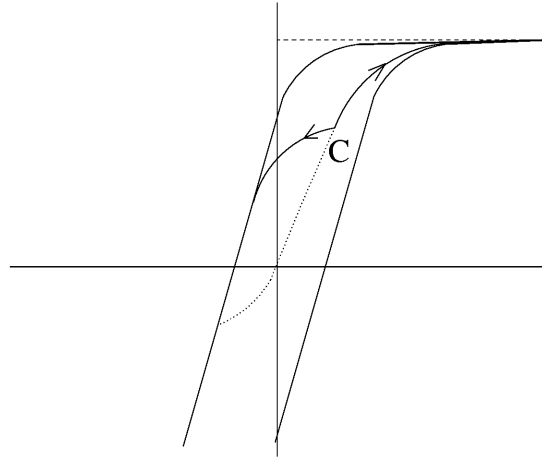


Figure 6.4: Possible locus curves in an operating point

As a consequence of the two-dimensional algorithm, the common starting point C of these two branches will move during the nonlinear iteration. In fact it highly depends on the actual orientation of the electric field at a particular iteration step. Therefore, it cannot be guaranteed that always the same branch is used in the numerical equation system during the iteration process. Regarding the different derivatives of the two functions this will lead to poor convergence and in the worst case to oscillations of the nonlinear iteration.

As this shows, a preselection of the appropriate branch is necessary in order to achieve convergence, especially for the simulation of complex structures. A suitable approach for

detecting the direction of the change of the electric field is solving a linearized equation system.

The equation

$$\vec{D} = \epsilon \cdot \vec{E} + f(\vec{E}) \quad (6.10)$$

is transformed by keeping the nonlinear part constant.

$$\vec{D} = \epsilon \cdot \vec{E} + f(\vec{E}_{\text{old}}) = \epsilon \cdot \vec{E} + \vec{P}_{\text{old}} \quad (6.11)$$

With this method an approximation of the electric field at the new operating point is obtained.

The parallel component of the old field vector to this approximation is calculated and the result is interpreted with respect to the orientation of the new field vector as outlined in Fig. 6.5 and Fig. 6.6.

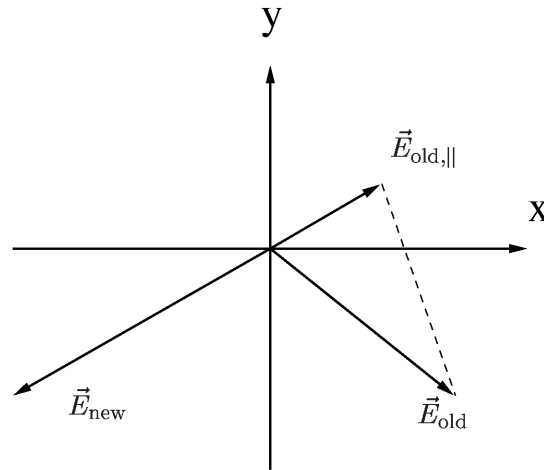


Figure 6.5: Detection of the change of the electric field, electric field decreases.

With this information it is now possible to select the correct branch of the hysteresis curve. The complete scheme is outlined in Fig. 6.7.

6.2.4 Calculation - Data flow

The previous sections gave a complete survey of the numerical details which had to be solved in order to allow the implementation of the two-dimensional algorithms outlined in Chapter 4 into the simulator. Summarizing all of the information the total data flow is obtained and is plotted in Fig. 6.8 in details.

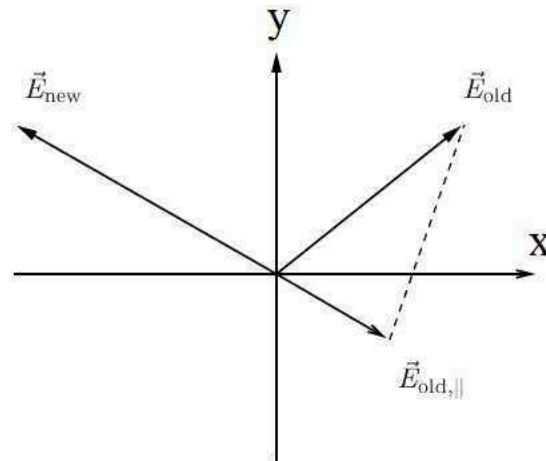


Figure 6.6: Detection of the change of the electric field, electric field increases.

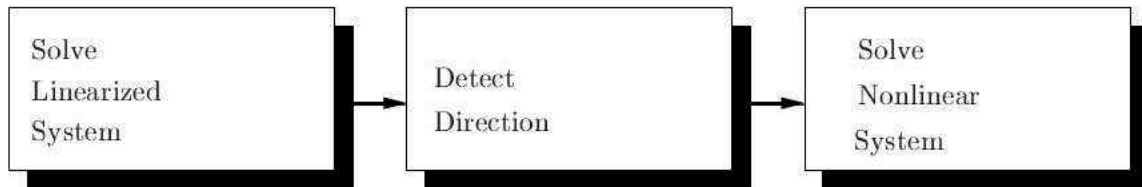


Figure 6.7: Modified trivial iteration scheme

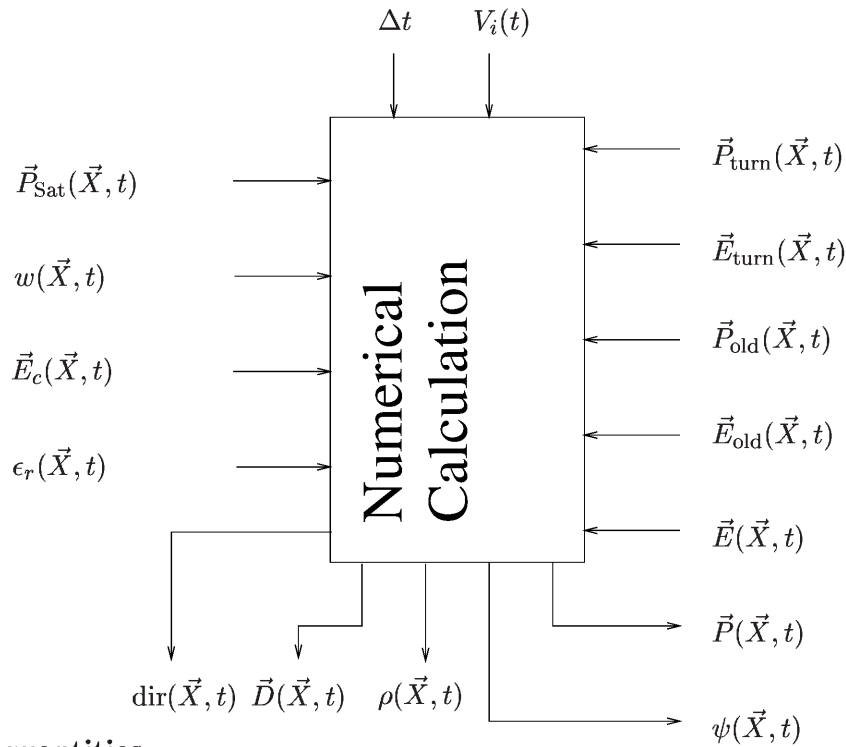
6.3 Postprocessing

In this phase several operations which are not coupled to the nonlinear equation system are performed. One of these tasks is the calculation of the overall contact charge Q out of the charge density ρ . The other task of this phase is the management of the history information. As already outlined in Section 3.2, the electric field and polarization of the last turning point are decisive for the calculation of the subcycles of the hysteresis. Therefore, history of the devices is evaluated and the turning points which are needed for the next operating points, namely E_{next} and P_{next} are provided. A schematic overview of these tasks is given Fig. 6.9.

6.3.1 Memory Management

As already outlined, the current value of polarization does not only depend on the current value of the electric field, but also the entire history has to be considered. For the implemented models, the relevant information of the device history consists of the electric field strength and the polarization at the turning points of the applied electric field.

Whereas the electric field at the boundary can easily be extracted from the potential at the grid points, this is not possible for the polarization. Therefore, the memory management of MINIMOS-NT was expanded in two ways: First, the values of all polarization and electric field

**Input quantities**

- $V_i(t)$...Voltage at contact i
 $\vec{P}_{\text{Sat}}(\vec{X}, t)$...Saturation polarization
 $w(\vec{X}, t)$...Shape factor of the hysteresis
 $\vec{E}_c(\vec{X}, t)$...Coercive field
 $\epsilon_r(\vec{X}, t)$...Relative dielectric constant
 $\vec{E}(\vec{X}, t)$...Electric field
 $\vec{E}_{\text{old}}(\vec{X}, t)$...Electric field at previous operating point
 $\vec{E}_{\text{turn}}(\vec{X}, t)$...Electric field at the last significant turning point
 \vec{P}_{old} ...Polarization at the previous operating point
 $\vec{P}_{\text{turn}}(\vec{X}, t)$...Polarization at the last significant turning point
 Δt ...Time step

Output quantities

- $\vec{D}(\vec{X}, t)$...Displacement
 $\vec{P}(\vec{X}, t)$...Polarization
 $\text{dir}(\vec{X}, t)$...Direction of the change of the electric field
 $\text{dir}_{\text{old}}(\vec{X}, t)$...Direction of the change of the electric field
 $\psi(\vec{X}, t)$...Potential
 $\rho(\vec{X}, t)$...Charge density

Figure 6.8: Data flow of the numerical calculation

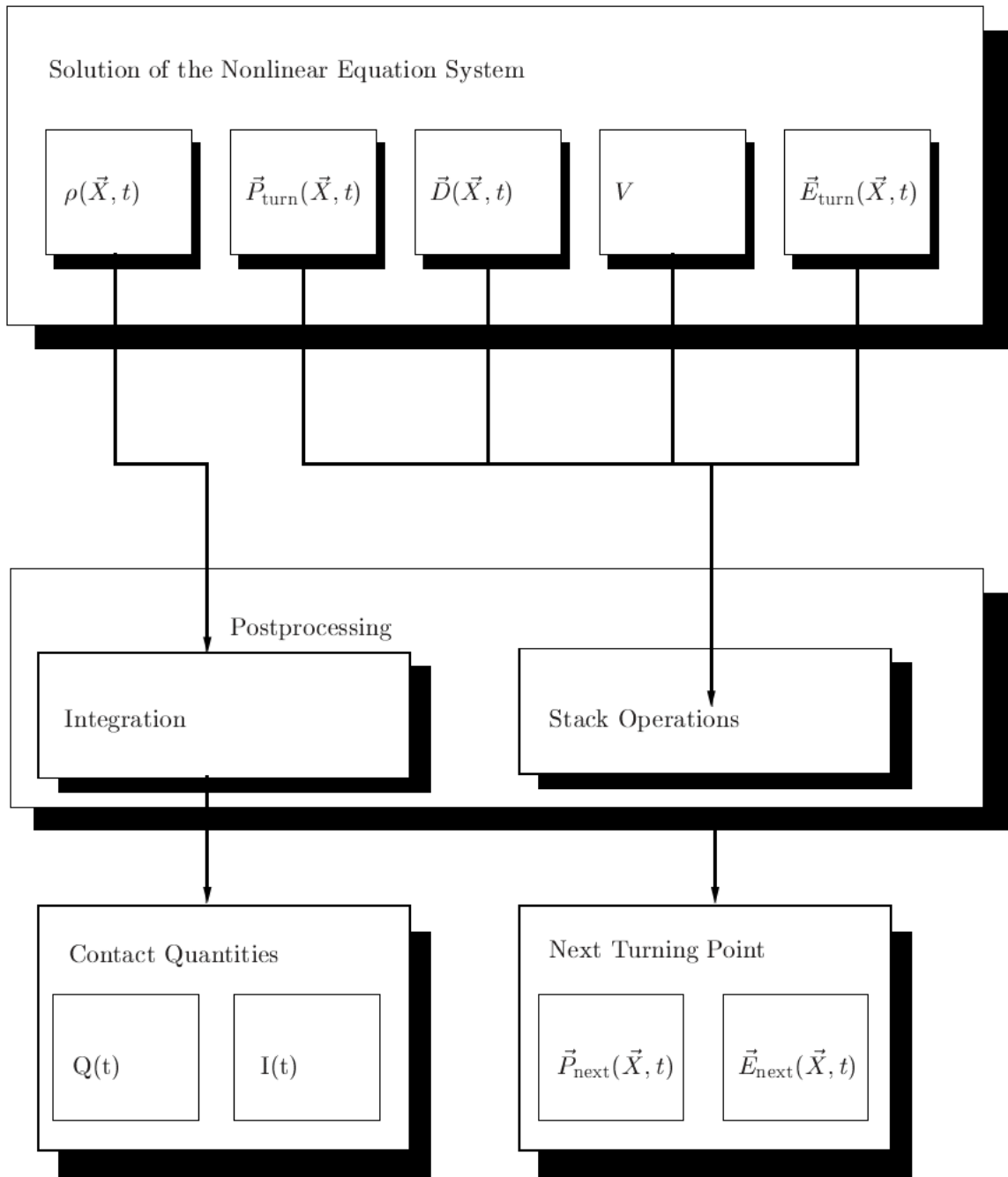


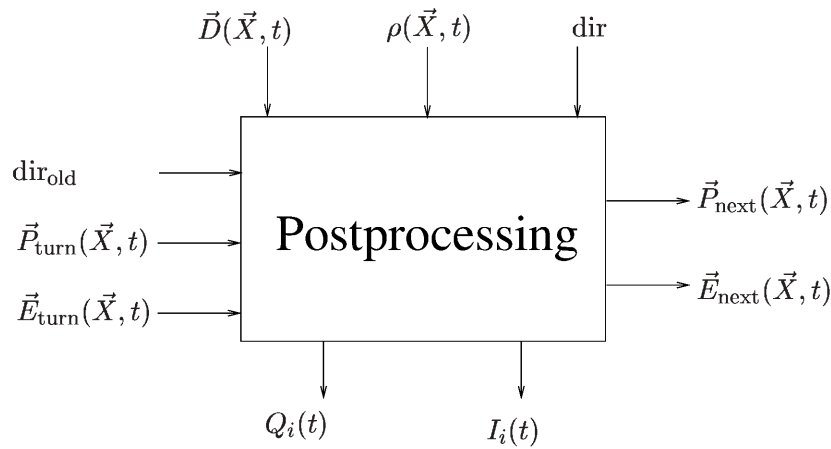
Figure 6.9: Overview of postprocessing

quantities, which cannot be recovered from the on-grid quantities of the previous operating point, are to be memorized ($\vec{P}, \vec{P}_{\text{turn}}, \vec{E}_{\text{turn}}$). Second, at each of the boundaries a stack has to be set up which contains the entire information on the device history.

The occurrence of a turning point is detected by comparison of the current direction with the previous one. If the direction changes, the values of the previous operating point are pushed to the stack, following the principle of the Preisach hysteresis concept concerning memory wipe-out (Subsection 3.2.4). The value of the electric field is compared to its precursor on the stack, and if the new value is higher, the old value is removed from the stack.

6.3.2 Data Flow of Postprocessing

The detailed concept of the data flow of postprocessing is plotted in Fig. 6.10. As outlined in the previous subsections, the distributed contact quantities are integrated and the turning point for the next operating point is calculated.



Input quantities

$\vec{D}(\vec{X}, t)$...Displacement

$\text{dir}(\vec{X}, t)$...Direction of the change of the electric field

$\text{dir}_{\text{old}}(\vec{X}, t)$...Direction of the change of the electric field at the previous operating point

$\rho(\vec{X}, t)$...Charge density

Output quantities

$\vec{E}_{\text{turn}}(\vec{X}, t)$...Electric field at the significant turning point

$\vec{P}_{\text{turn}}(\vec{X}, t)$...Polarization at the significant turning point

$\vec{E}_{\text{next}}(\vec{X}, t)$...Electric field, significant turning point for next operating point

$\vec{P}_{\text{turn}}(\vec{X}, t)$...Polarization, significant turning point for next operating point

$Q_i(t)$...Charge at contact i

$I_i(t)$...Current at contact i

Figure 6.10: Data flow of postprocessing

Chapter 7

Ferroelectric Non-volatile Memory Cells

USING FERROELECTRIC materials for non-volatile memories is a very promising approach. Table 7.1 shows a comparison of ferroelectric memories, electrically erasable and programmable read-only memories (EEPROMs), and Flash memory. As the latter devices have been produced for several years now they represent a quite mature technology. This gives them some advantage in terms of integration density [PBOZ97]. Nevertheless, advanced state-of-the-art stacked capacitor-transistor designs show similar cell sizes as EEPROMs [ATM⁺98]. Already existing prototypes like the ferroelectric memory field effect transistors (FEMFET) are even expected to reach the density of Flash memory.

As can be seen from Table 7.1, non-ferroelectric devices require less power for read cycles. But in terms of overall power consumption and write speed ferroelectrics offer far superior properties [SG00][SMN⁺95]. They also do not require any voltage different from the supply voltage, which is a significant advantage.

Type	Area/Cell (normalized)	Read Access Time	Write Access Time	Energy per 32b Write	Energy per 32b Read
EEPROM	2	50ns	10 μ s	1 μ J	150pJ
Flash Memory	1	50ns	100ns	2 μ J	150pJ
Ferroelectric Memory	2-5	100ns	100ns	1nJ	1nJ

Table 7.1: Comparison of different types of non-volatile memories, after Sheikoleslami [SG00]

Basically, ferroelectric memory cells can be separated into two different design types, outlined in Fig. 7.1, depending on whether the ferroelectric material is integrated into the read/write transistor or not. In the latter case a capacitor is used for data storage. The capacitors can be placed either immediately in the vicinity of the read/write transistor or in a separated array of capacitors somewhere on the chip.

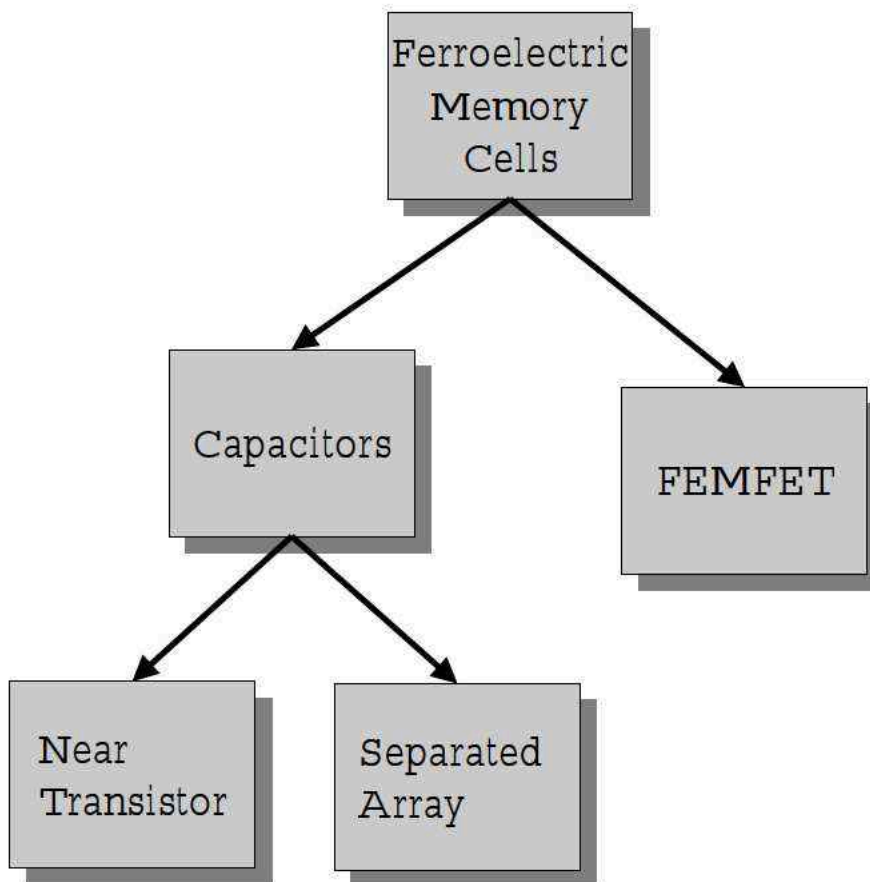


Figure 7.1: Overview of the different ferroelectric memory designs

7.1 The Transistor Capacitor Memory Cell

The most common design for ferroelectric non-volatile memory is similar to the classical DRAM structure. It consists of a capacitor used for information storage and a transistor for the read and write operations. Such cells can be fabricated by using a conventional LSI CMOS process and adding the capacitor afterwards in another layer above the transistor [KTM⁺97], thus leading to the structure sketched in Fig. 7.2.

Starting out from this basic cell two different circuit designs are used, namely a double cell and a single cell design.

7.1.1 Double Cell Design

The double cell (2C2T) structure which is outlined in Fig. 7.3 was introduced by Evans and Womack in 1988 already [EW88]. For write operation the bit line (BL) and the inverse bit line ($\overline{\text{BL}}$) are set to the wanted states (V_{sup} for logical “1” and ground for logical “0”) by the sense

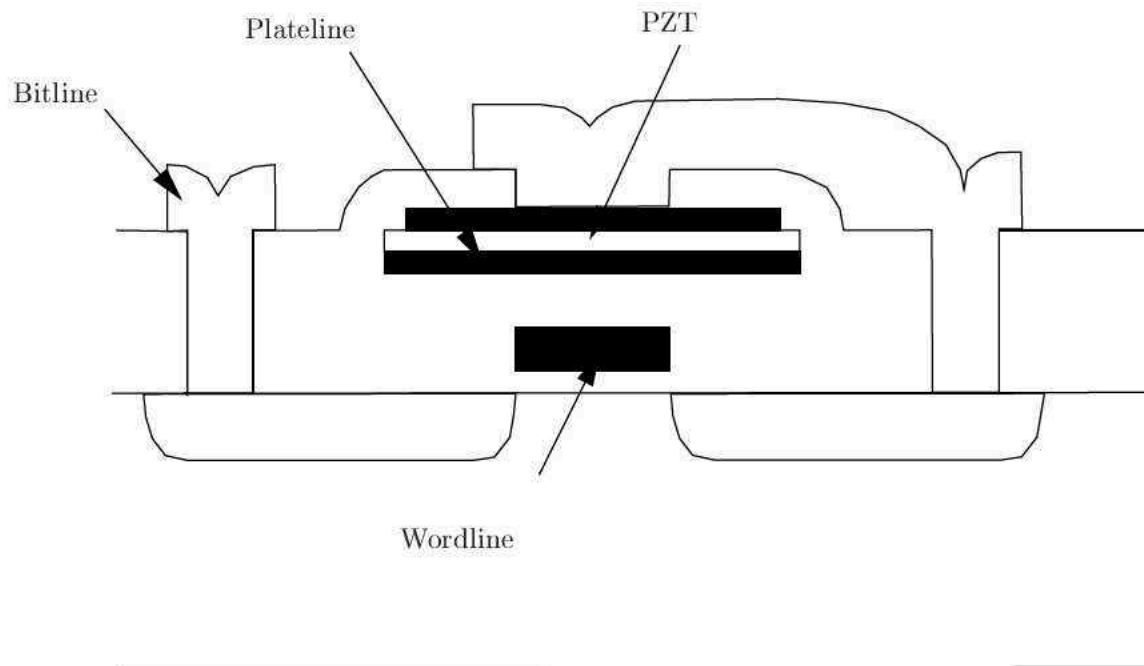


Figure 7.2: Cross section of a stacked transistor–capacitor structure

amplifier. Plate line and word line have to be activated simultaneously. Depending on the branch of the double structure two different operating points will evolve at the capacitors. Due to the ferroelectric properties the charge difference which represents different polarizations in the materials, will remain at this level even when the sense amplifier is turned off after write operation.

During read operation the charge at the two bit lines will differ, and accordingly a potential will occur at the two entries of the sense amplifier. The amplifier itself will drive the potential back to the initial write potential, thus restoring the original state immediately after a write operation [JCJ⁺97]. The timing diagram of read and write operations is given in Fig. 7.4.

7.1.2 Single Cell Design

In order to achieve higher integration densities single-transistor single-capacitor structures have become the state-of-the-art design for ferroelectric memories.

The equivalent circuit is plotted in Fig. 7.5. The operating principle is based on moving the charge between the bit line capacitor C_B and the ferroelectric capacitor C_F . The drawback of this method is that an external reference voltage has to be generated in order to allow the evaluation of the memory state.

During write operation, the memory cell is accessed by raising the wordline (WL) voltage, which turns the access transistor in ON state, and at the same time pushes the ferroelectric capacitor into negative saturation, no matter whether the cell was in the “1” or “0” state. In the second half of the write cycle, the plateline (PL) voltage is raised. As the transistor

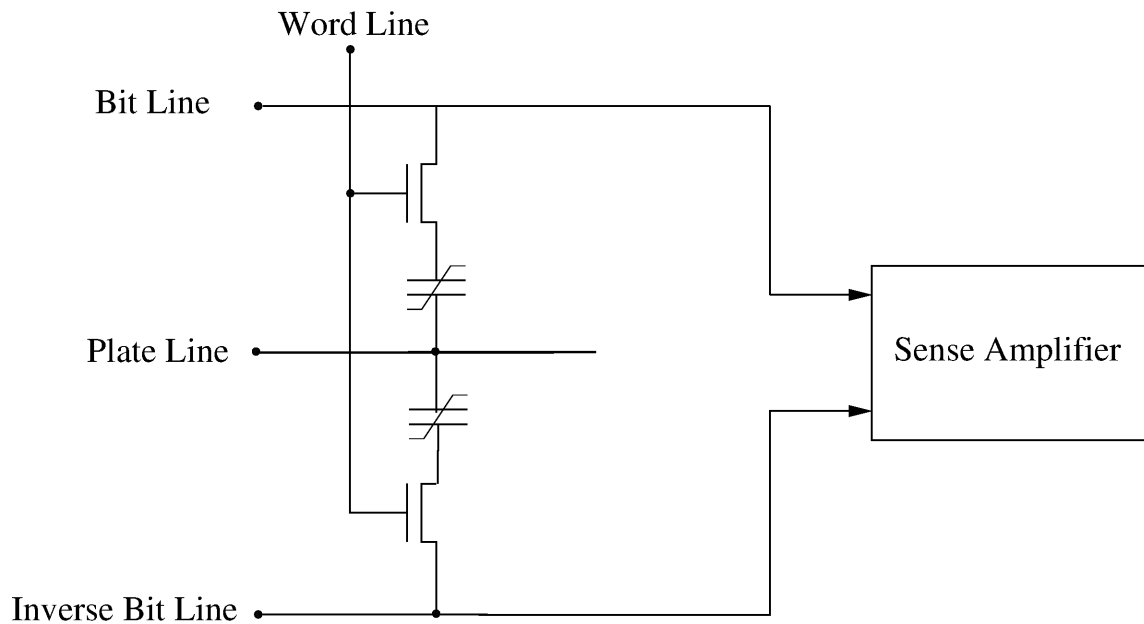


Figure 7.3: 2C2T circuit

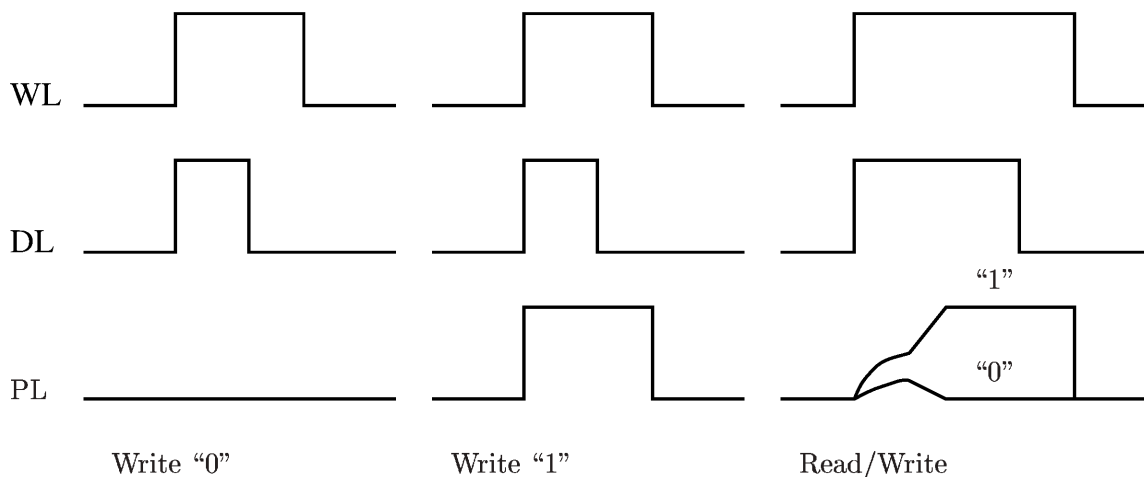


Figure 7.4: Sense scheme of a 2C2T circuit

is in the ON state, the potential difference between bitline (BL) and plateline modifies the operating point of the capacitor. In case of “0”, the bitline is not raised and C_F will be in positive saturation, and after the write cycle is finished, C_F will be defined by the positive remanent polarization P_{Rem} . If the bitline is raised and a “1” is written, the potential difference will be insignificantly low and C_F will be at the negative remanent polarization $-P_{Rem}$, and remain there after the write cycle.

Fig. 7.8 shows the timing diagram of the read cycle. At first the bitline is actively set to 0V. After the bitline capacitor is discharged, writeline and plateline are activated using the supply voltage V_{DD} . Now C_F and C_B form a capacitive voltage divider between plateline and ground. Depending on the information in the memory cell, the operating points of the

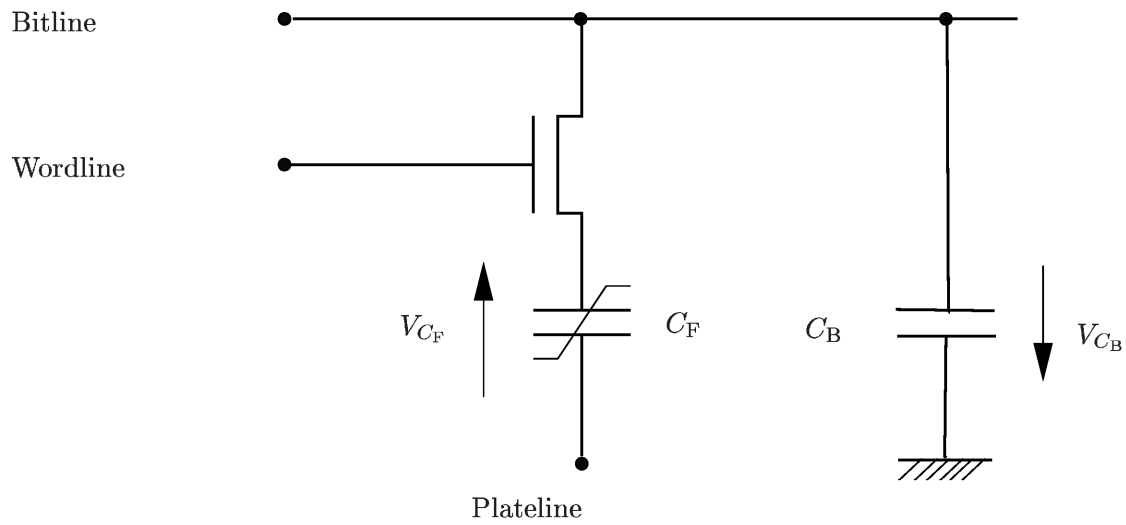


Figure 7.5: 1C1T circuit

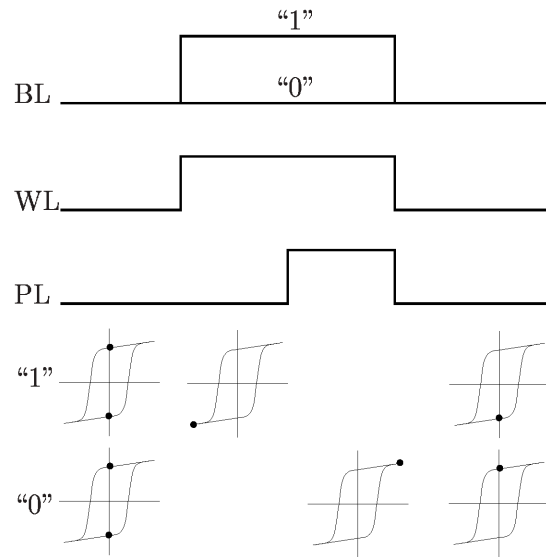


Figure 7.6: Sensing scheme of the write operation of the 1C1T circuit

ferroelectric material differ, and so does the capacity of C_F . If the ferroelectric hysteresis is approximated by two different capacitors (Fig. 7.7), the bitline voltage reads as

$$V_0 = \frac{C_0}{C_0 + C_B} V_{DD} \tag{7.1}$$

if the stored information is “0” and

$$V_1 = \frac{C_1}{C_0 + C_B} V_{DD} \tag{7.2}$$

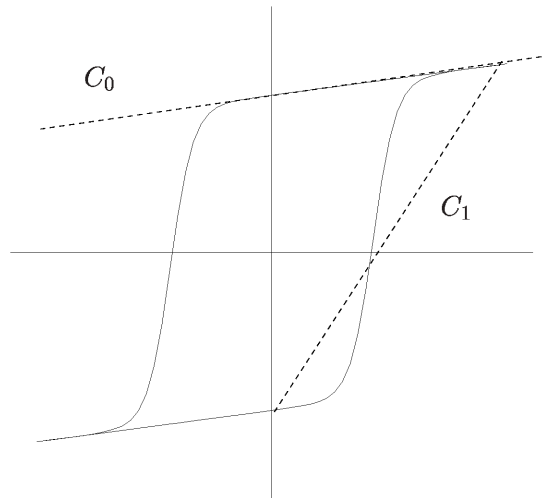


Figure 7.7: Approximation of the hysteresis loop with capacitors

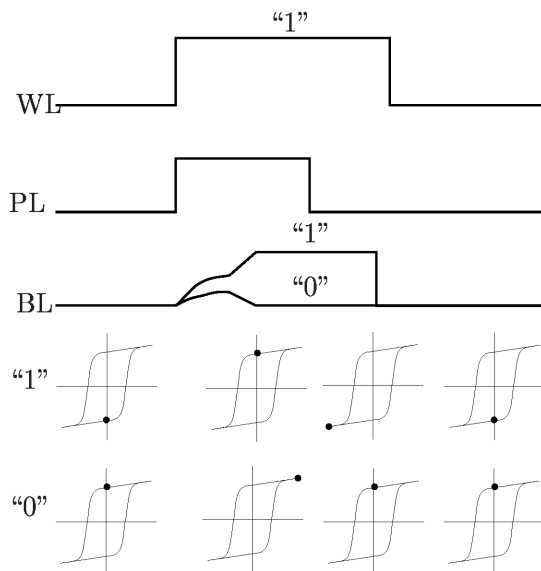


Figure 7.8: Timing diagram of the read operation of the 1C1T circuit

if the stored information is “1”. These two different voltages are detected by the sense amplifier, and, similarly to the 2C2T structure, the original information is restored in the memory cell.

7.2 The Ferroelectric Memory Field Effect Transistor

The Ferroelectric Memory Field Effect Transistor (FEMFET) takes direct advantage of the hysteretic properties of polarization and displacement of a ferroelectric material. The

FEMFET is constructed by inserting a ferroelectric segment into the sub-gate area of an NMOS, as outlined in Fig. 7.9.

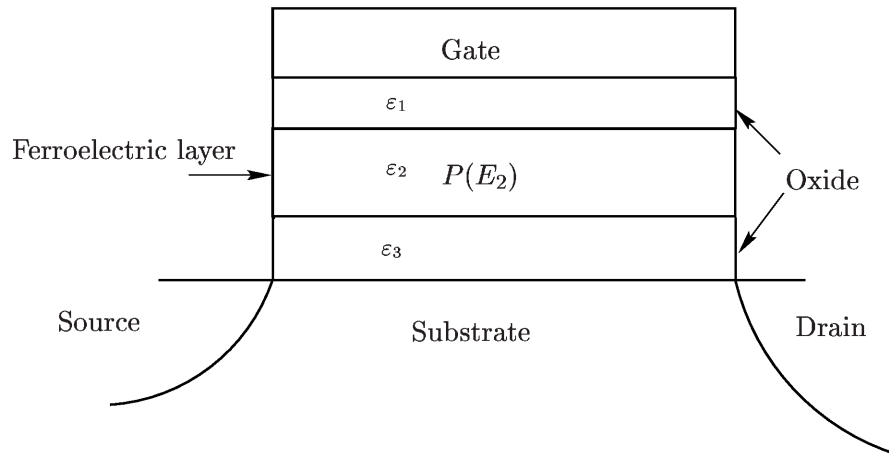


Figure 7.9: Ferroelectric non-volatile memory field effect transistor

This device design is attractive for large scale integration, as it represents a very compact design of a complete non-volatile memory cell. The achievable integration density is identical to the well-known floating-gate Flash memory cells, but the operating conditions are much smoother, as the information can be stored with the default operating voltages in the range of 1 V and, same as for the transistor-capacitor designs, no higher voltage peaks, as necessary for the floating gate device, are required.

This design was introduced by Miller and McWorther in 1992 [MM92], and a compact model for this device was extracted. In 1999 an advanced compact model introducing the Preisach hysteresis was presented by Ullmann et al. [UGH⁺99]. As a rigorous analysis shows, these compact models by far underestimate the complexity of the properties of the device.

Processing this device proved to be very complicated, especially the interface between substrate surface and ferroelectric layer caused many problems. Recently these problems seem to have been solved and the first prototypes have been presented [MWC99].

7.2.1 Operating Principle

The FEMFET technology is still in an early prototype phase, so no canonic sensing scheme exists to the date of this thesis. This subsection introduces a straightforward way to utilize the hysteresis properties of the gate dielectric.

During write operation a positive or negative pulse is applied to the gate, which will orient the dipoles in the gate dielectric either in the up or down direction. Due to the ferroelectric properties, they will keep their orientation after the write pulse has ended and the gate voltage drops back to zero. The impact of the resulting dipole moment on the charge distribution in the channel is schematically outlined in Fig. 7.10 and Fig. 7.11.

If the device is designed in a way that the threshold voltage is near zero, this will have drastic consequences to the drain current of the device. In the ON state a significant current will be detectable, where as in the OFF state the device is driven deep into the subthreshold regime.

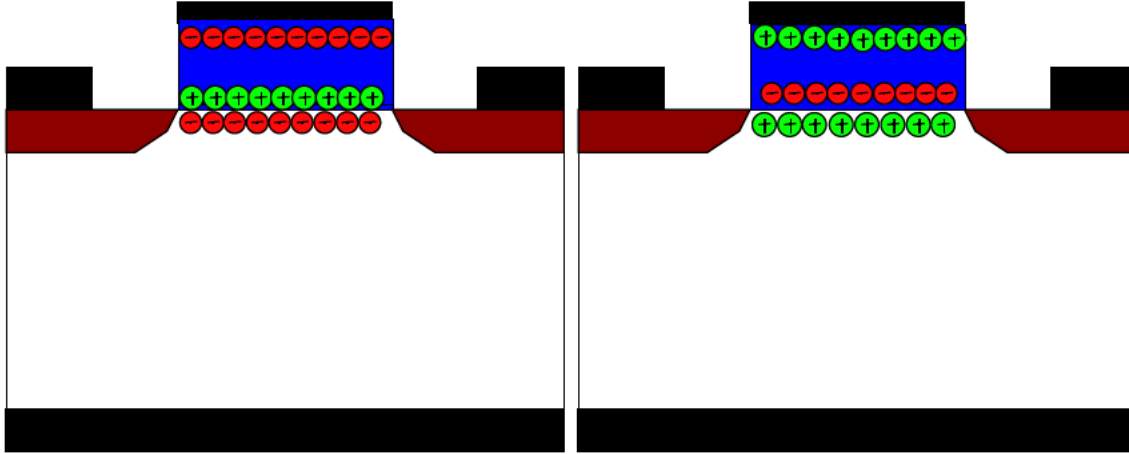


Figure 7.10: ON state of the FEMFET

Figure 7.11: OFF state of the FEMFET

Chapter 8

Simulation of Ferroelectric Devices

IN ORDER TO demonstrate the abilities of the implemented algorithms, several typical ferroelectric structures are analyzed with the device simulator MINIMOS-NT. Special care is taken of outlining possible applications of the tool for device and circuit design.

Section 8.1 concentrates on the general two-dimensional algorithm for isotropic materials. It is shown that with the simulation results equivalent parameters for a compact model can be extracted.

Section 8.2 deals with the influence of anisotropy, the inclusion of which gets mandatory if the thickness of the device gets into the range of the grain size.

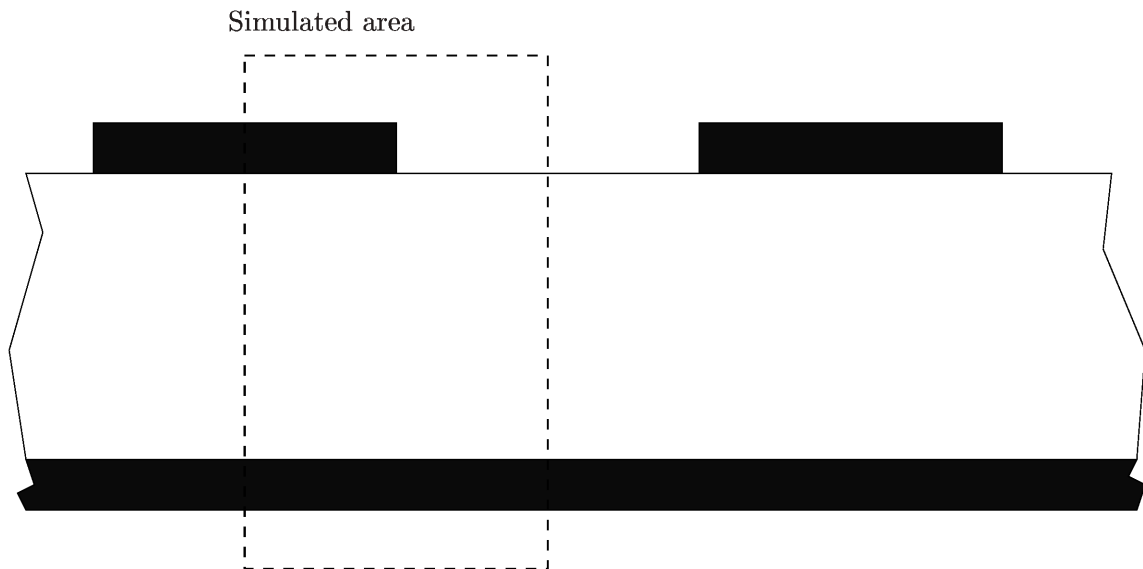


Figure 8.1: Cross section of a finger structure and the simulated area

Section 8.3 deals with the maybe most promising ferroelectric device, the FEMFET which is, from the viewpoint of device simulation, definitely the most complex ferroelectric device.

8.1 Extraction of Equivalent Parameters for a Finger Structure

The finger structure is a basic structure used for highly integrated memory cells. This structure consists of a series of top electrodes and a common ground plate. A cross section and the area simulated for the extraction of the basic hysteresis data are sketched in Fig. 8.1.

Fig. 8.2 shows the simulated Q/V characteristics of this two-dimensional device and compares them to the characteristics of the simple one-dimensional structure of the same width. It already contains properties and effects that exceed the one-dimensional case. As a result of the edge effect of the electric field, the field strength in this area will exceed the strength of the coercive field even for small contact voltages. This leads to an area of polarization reversal (Fig. 8.3) and to a decrease of the coercive field of the device.

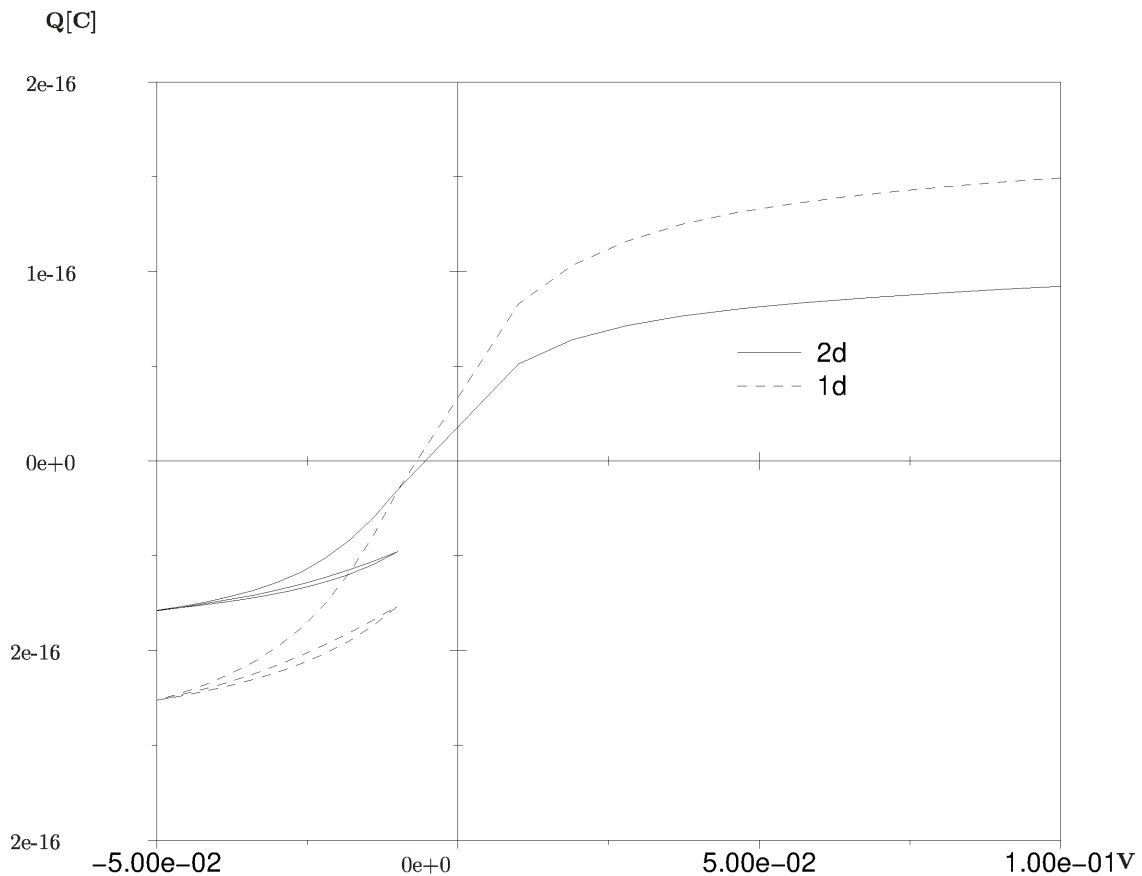


Figure 8.2: 'One-dimensional' capacitor versus finger structure

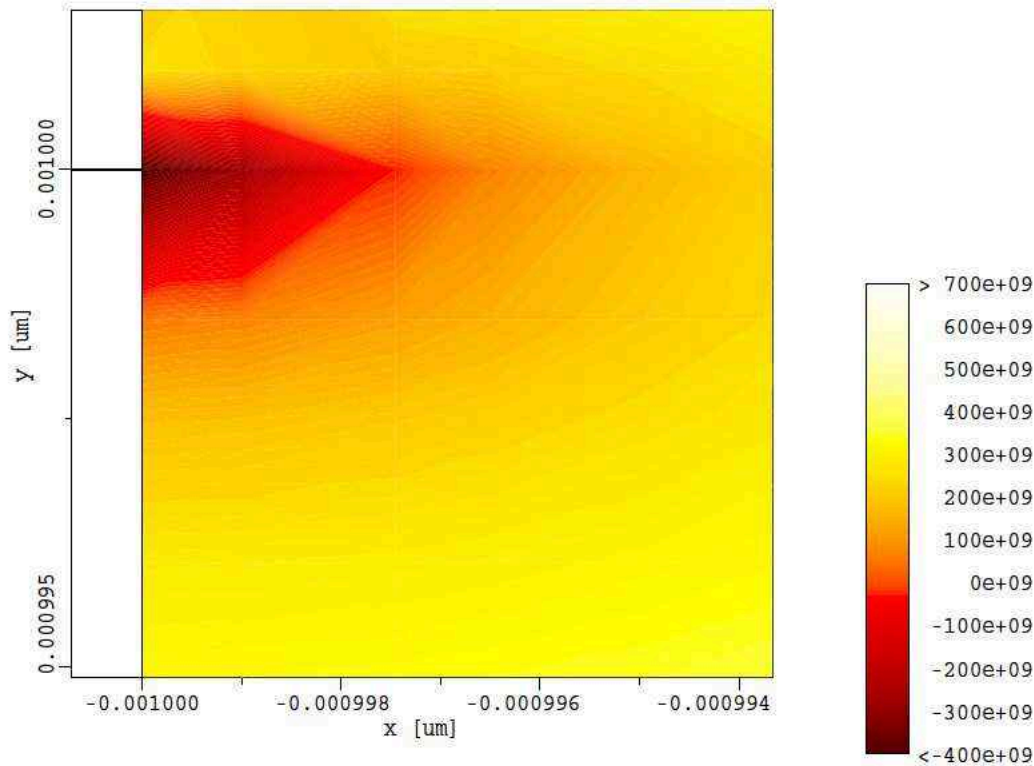


Figure 8.3: Polarization reversal near the edge of the contact

Of course the two-dimensional analysis is numerically more expensive than the analysis of a simple one-dimensional capacitor.

With the help of these simulation results it is possible to extract new hysteresis parameters for a one-dimensional device which allow the accurate simulation of this two-dimensional structure. The resulting Q/V characteristics of this calibration are outlined in Fig. 8.4. This feature of the simulator is very useful as it reduces the effort substantially and allows the utilization of a compact model. This opens the door to improved circuit simulation.

8.2 Simulation of Thin Films

As already outlined in Section 4.2.4, anisotropy has to be taken into account when the dimensions of the analyzed device reach into the range of the grain size of the ferroelectric

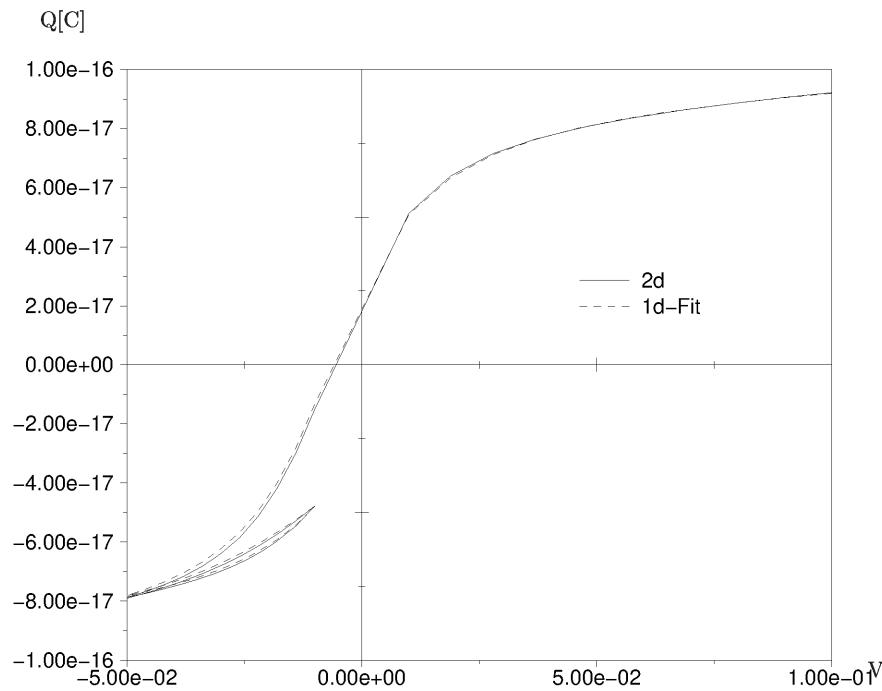


Figure 8.4: Comparison of the transfer characteristics of a finger structure and the 'one-dimensional' capacitor with fitted hysteresis parameters

material. Since these are the first simulations which have been carried out in this field, a planar capacitor with a ferroelectric dielectric is analyzed. The angles of the axes of anisotropy are defined as shown in Fig. 8.5.

8.2.1 Simulation of Materials with Uniaxial Anisotropy

Fig. 8.6 shows the different simulated down branches of the hysteresis when the orientation of the axis of a material with uniaxial anisotropy varies.

The absolute charge in the capacitor decreases with the angle and the coercive field increases. These effects can easily be understood by geometrical considerations. According to the Poisson equation, the contact charge is proportional to the component of the polarization which is perpendicular to the surface, and it will be reduced if the angle between the polarization and the vector perpendicular to the surface increases.

A similar effect causes the increase of the coercive field. In this case the component of the electric field in the direction of the anisotropy axis is decisive for the resulting polarization. Obviously, if the electric field is not parallel to the anisotropy axis, it has to be increased in order to raise a field of the same strength in the axis direction.

The nonlinearity of the material leads to a complex field distribution. Due to Poisson's equation, the displacement (Fig. 8.7) and, as a consequence of the monotonic D/E characteristics, the electric field (Fig. 8.8) decrease near the charge free boundary to the insulating material.

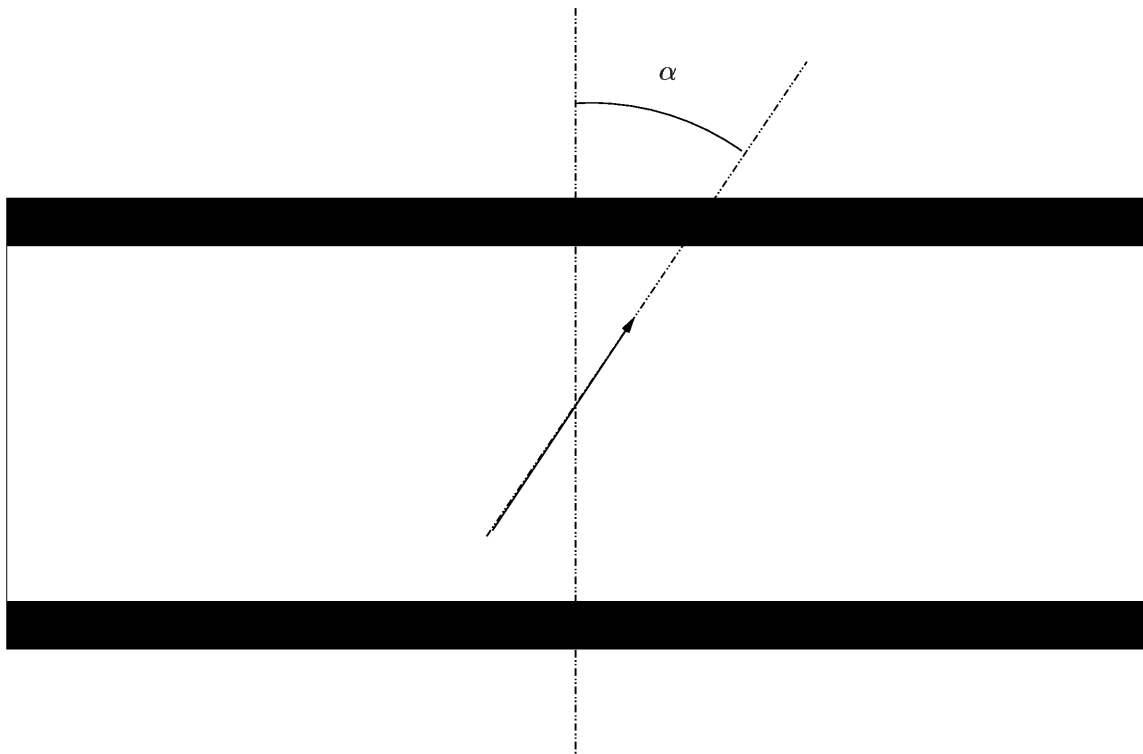


Figure 8.5: Definition of the angle α of the axis of anisotropy

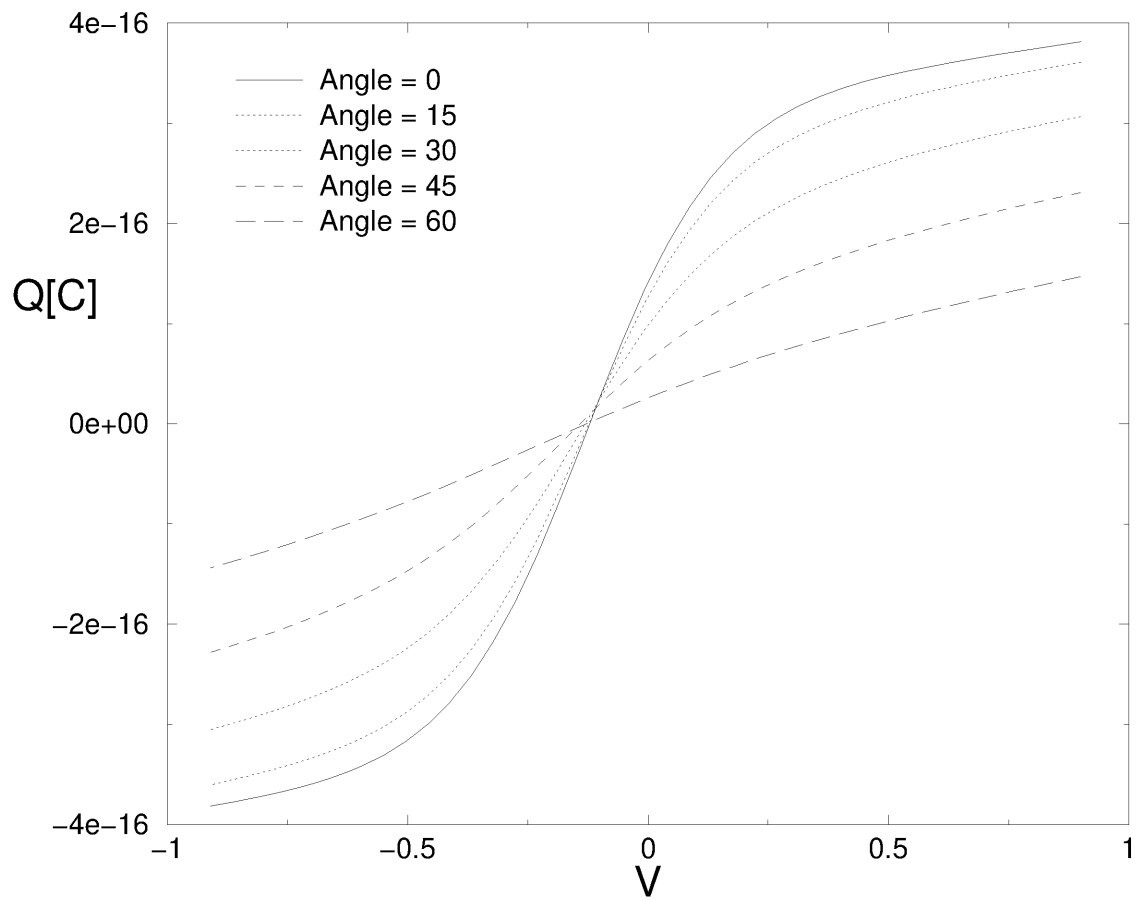


Figure 8.6: Hysteresis curves for different angles of the anisotropy axis

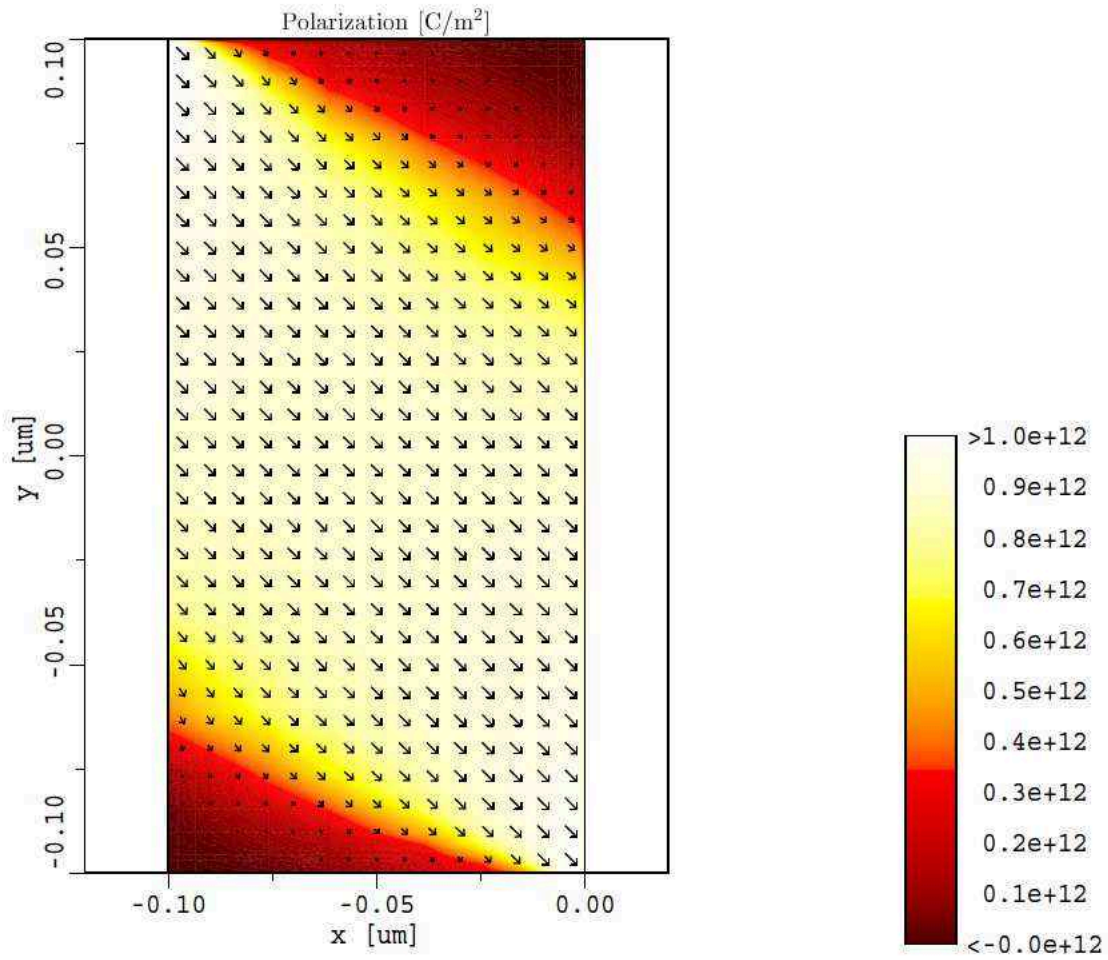


Figure 8.7: Distribution of the polarization field, angle = 45°

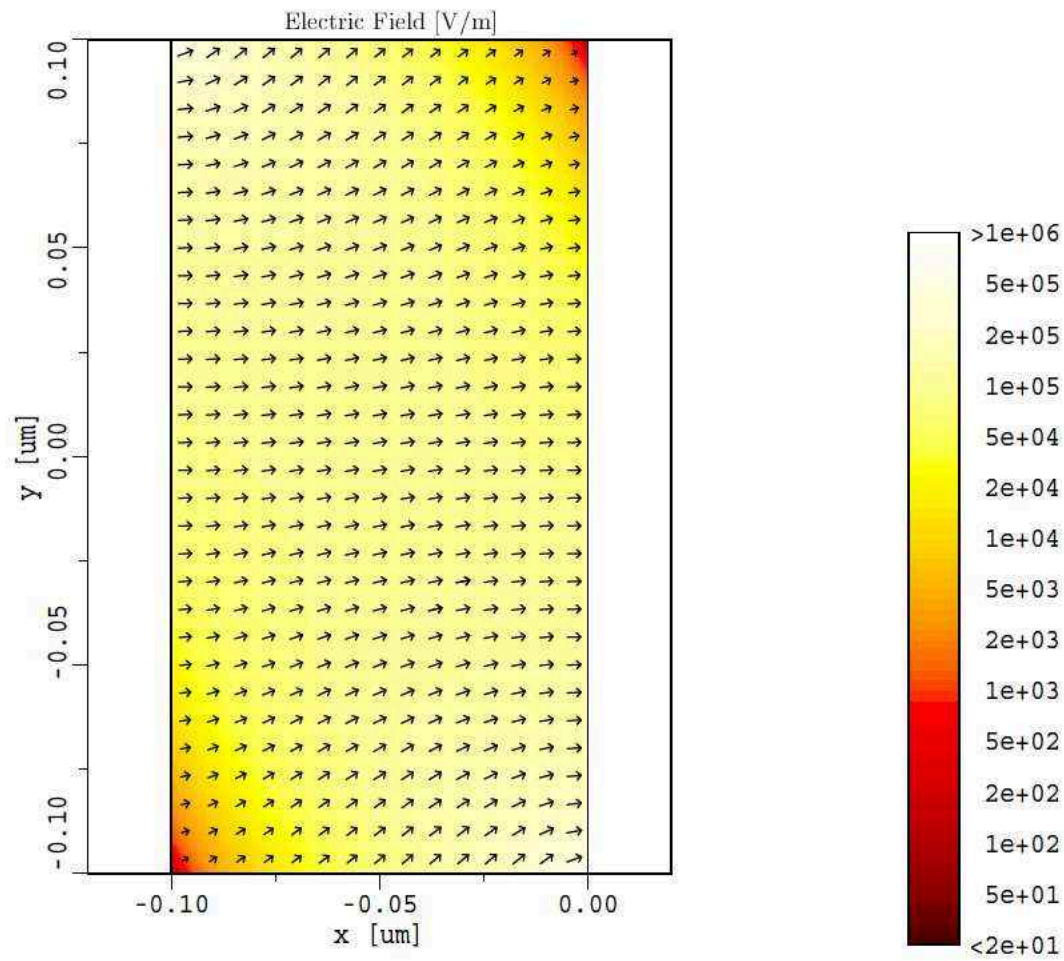


Figure 8.8: Distribution of the electric field, angle = 45°

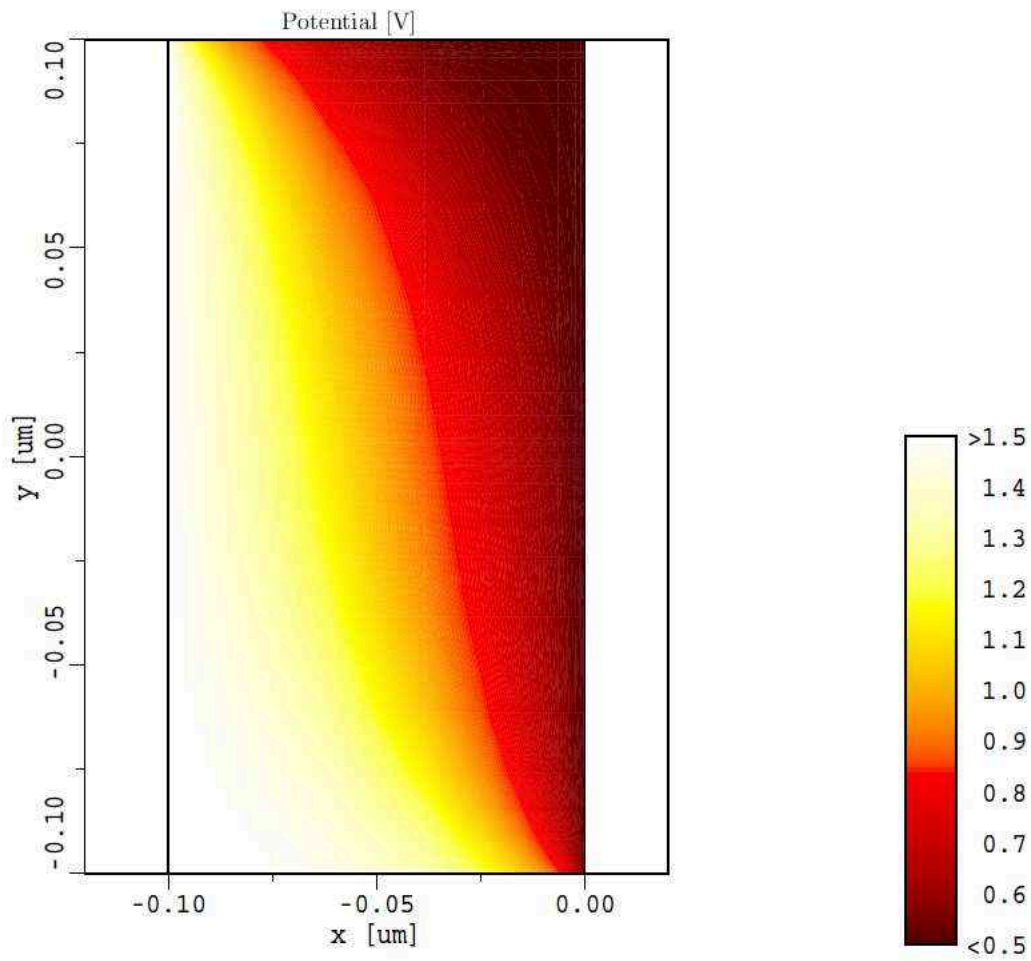


Figure 8.9: Distribution of the potential, angle = 45°

8.2.2 Simulation of Materials with Biaxial Anisotropy

Simulation of biaxial anisotropy shows different properties and, since the model is more complex, additional effects. The simulations concentrate on a material, with two perpendicular anisotropy axes.

Again first investigations are focused on the hysteresis of the Q/V characteristics. The down branches are plotted in Fig. 8.10. It is easy to see that if the electric field is parallel to one of the anisotropy axes, the same results as for uniaxial materials are obtained. Similarly to the uniaxial case, an increase of the angle between the anisotropy axis and the device axis leads to a reduction of polarization, but only until the angle reaches 45° .

The most interesting effect visible in Fig. 8.10 is the occurrence of kinks in the Q/V characteristic. These kinks develop when the axial components are reduced because their sum exceeds the saturation polarization.

The different polarization components and the total polarization are plotted separately, as shown in Fig. 8.11, Fig. 8.12, and Fig. 8.13. The angles of the anisotropy axes to the axes of the device were 15° and 75° , respectively. The applied potential was 0.91 V.

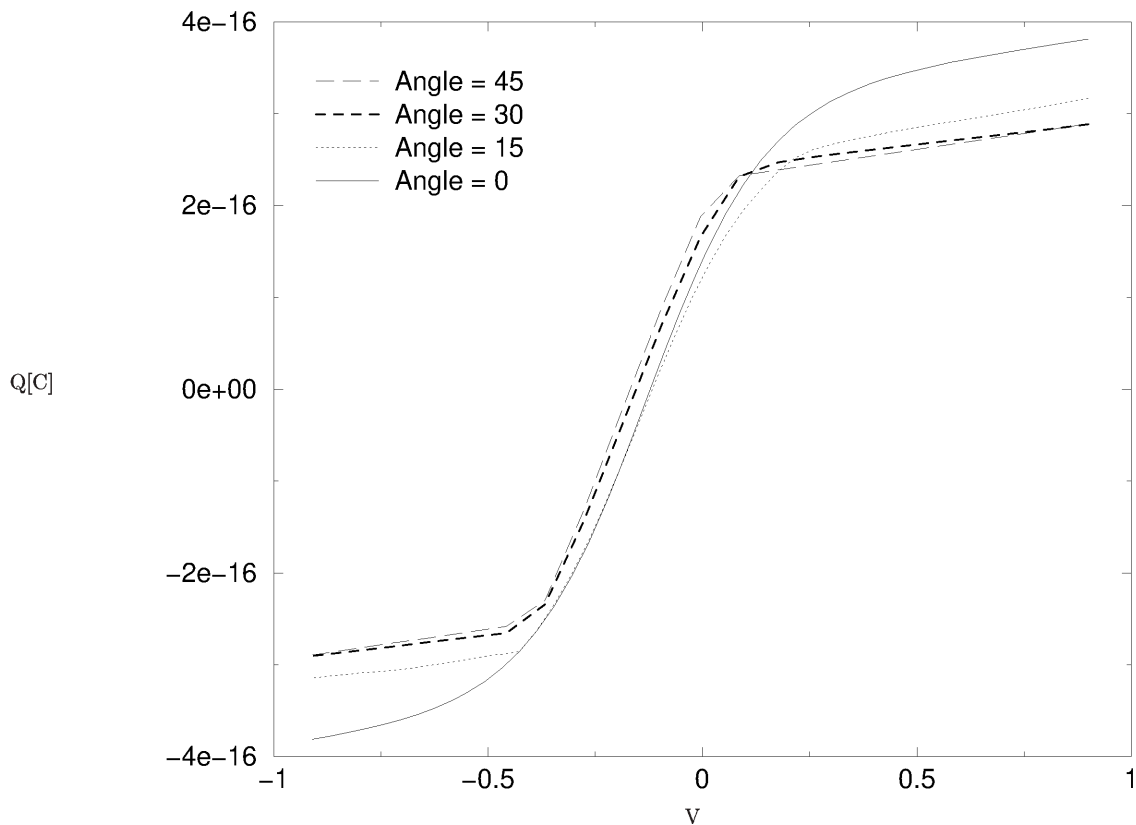


Figure 8.10: Hysteresis curves for different angles of the anisotropy axes; two perpendicular anisotropy axes are applied

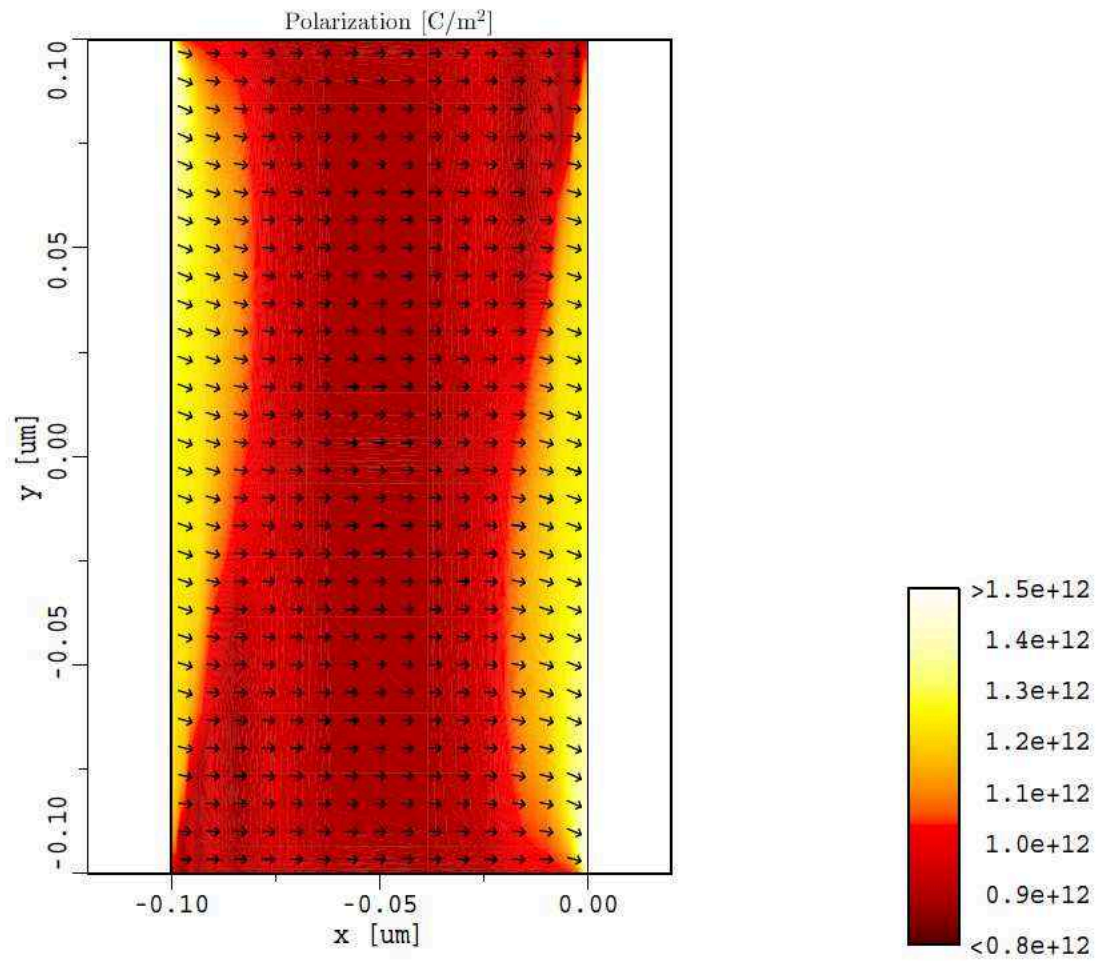


Figure 8.11: Total polarization in a device with two anisotropy axes

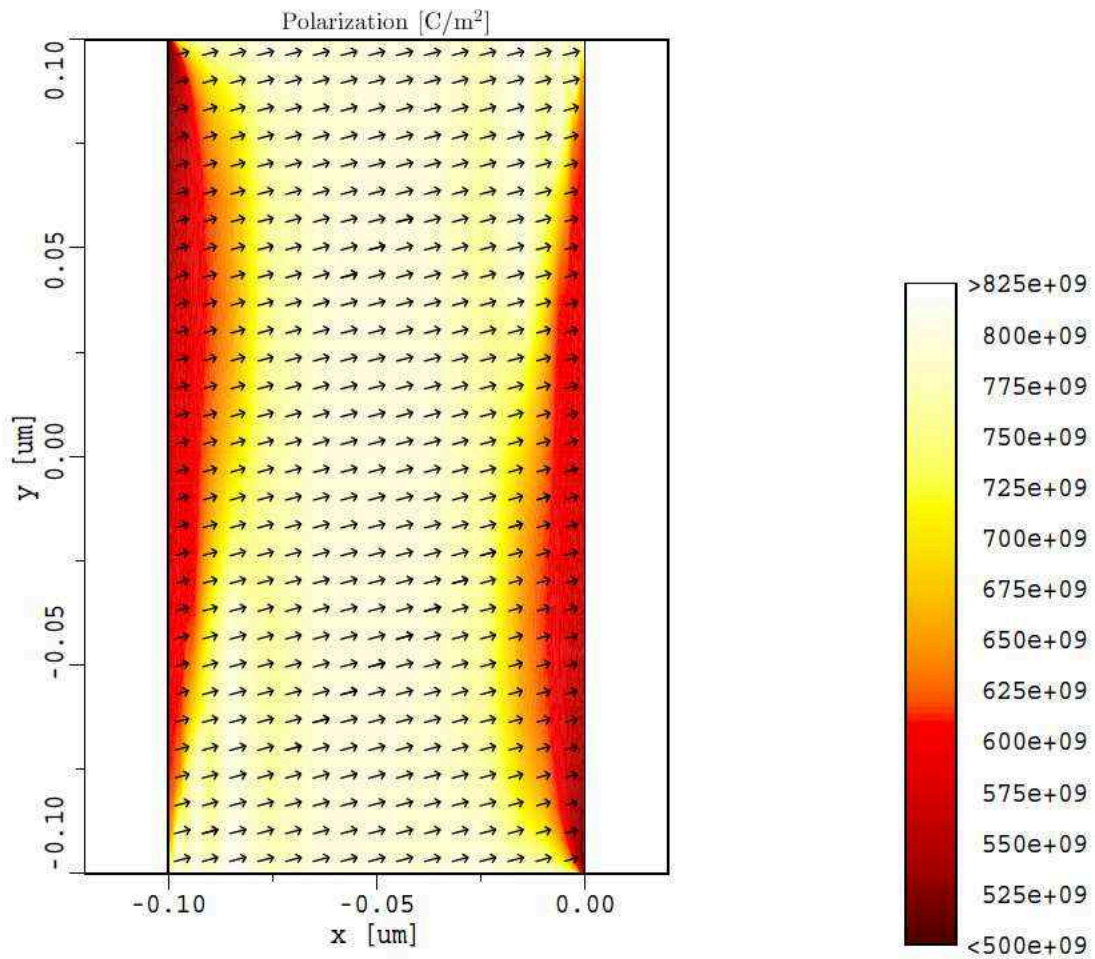


Figure 8.12: Polarization in the first anisotropy direction, angle = 15°

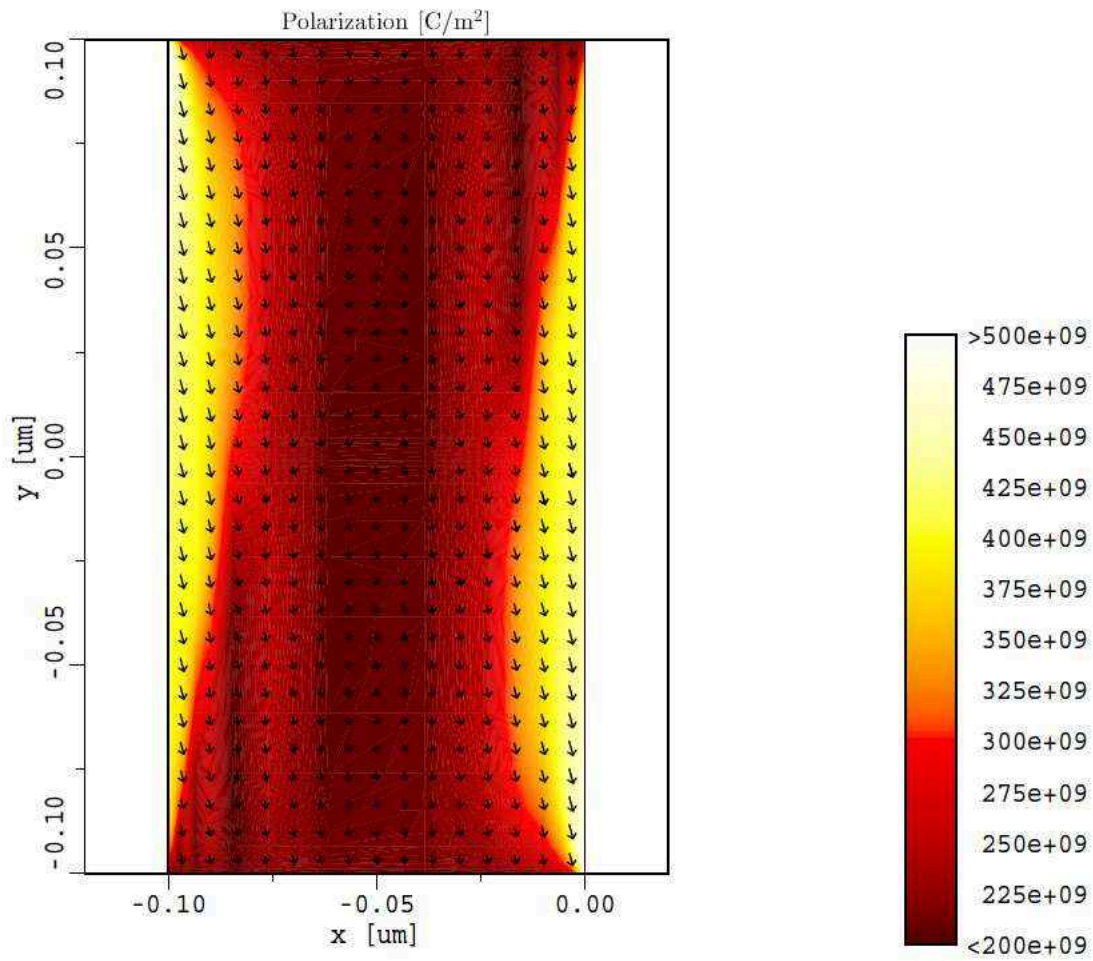


Figure 8.13: Polarization in the second anisotropy direction, angle = 75°

8.3 Analysis of a Ferroelectric Memory Field Effect Transistor

As outlined in Section 7.2, the FEMFET is one of the most attractive designs of ferroelectric non-volatile memory cells, especially because of its low space consumption. However this compact design also increases the complexity of and accordingly the demands on a simulation tool.

The insertion of a material with a high permittivity has strong impact on the device performance. This became one of the key issues of device design and is being investigated heavily, with respect to material issues [LWK⁺98][MOS⁺99] and the performance point of view [CCR⁺99][CCV⁺99][IRCW99][KYY⁺98][YKL98].

The modification of the dielectric properties of the gate insulator has visible consequences for device performance. Similarly to regular CMOS devices an increase of the relative dielectric constant ϵ_r shifts the I_d/V_g characteristics to the right. This can be avoided by an increase of the oxide thickness which has in turn a significant impact on the electrical behavior of the device. Since the distance from the gate to the channel is larger, this leads to a loss of control over the channel. The most serious consequence of this effect is a significant increase of the drain current in the OFF state of the transistor.

Next will be demonstrated that the simulation tool can keep up with the demands of TCAD by extraction of the significant device information like transfer characteristics, field distribution, and space charge density.

For the simulation an NMOS with $1\mu\text{m}$ gate length was transformed into a FEMFET, by entering a ferroelectric segment under the gate. In order to keep parasitic effects between gate and drain/source and between drain/source and channel low, two non-ferroelectric spacers are placed on both sides of the gate. The geometry of the simulated device is outlined in Fig. 8.14. Acceptor- and Donor doping distribution are shown in Fig. 8.15 and Fig. 8.16, respectively.

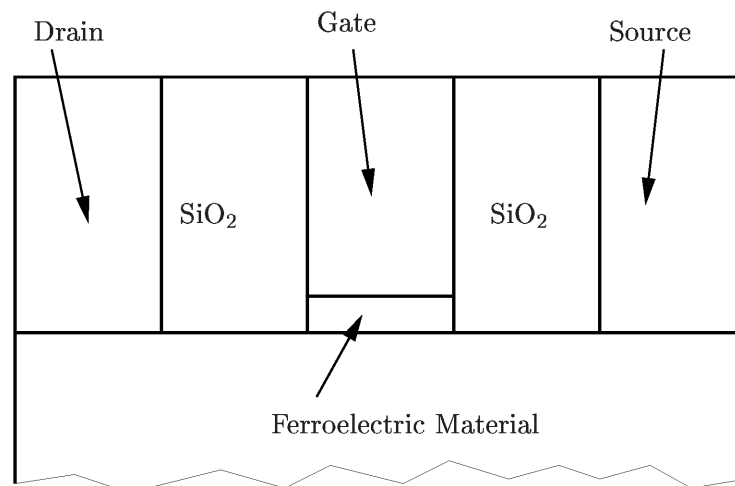


Figure 8.14: Geometry of the gate area

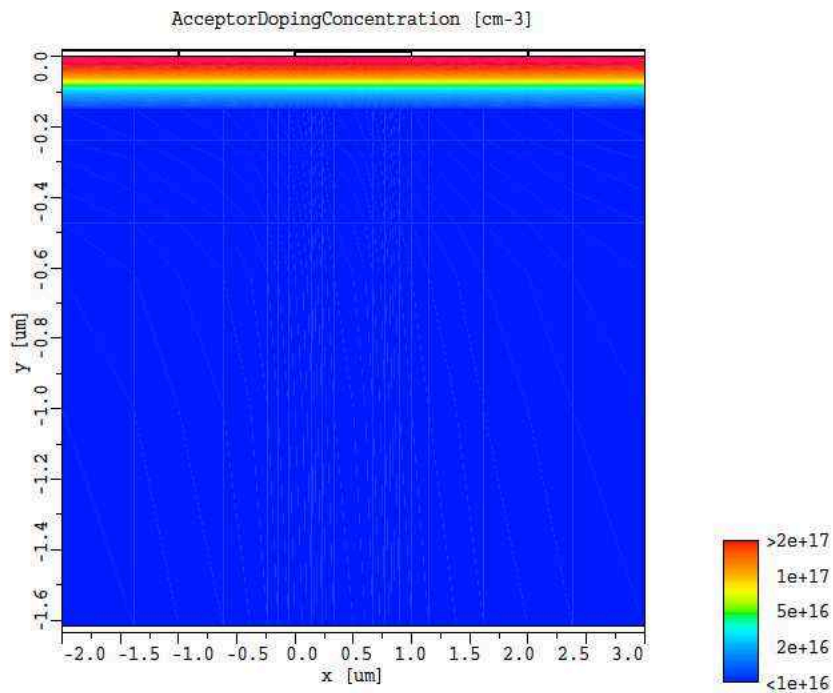


Figure 8.15: Acceptor doping distribution of NMOS and FEMFET

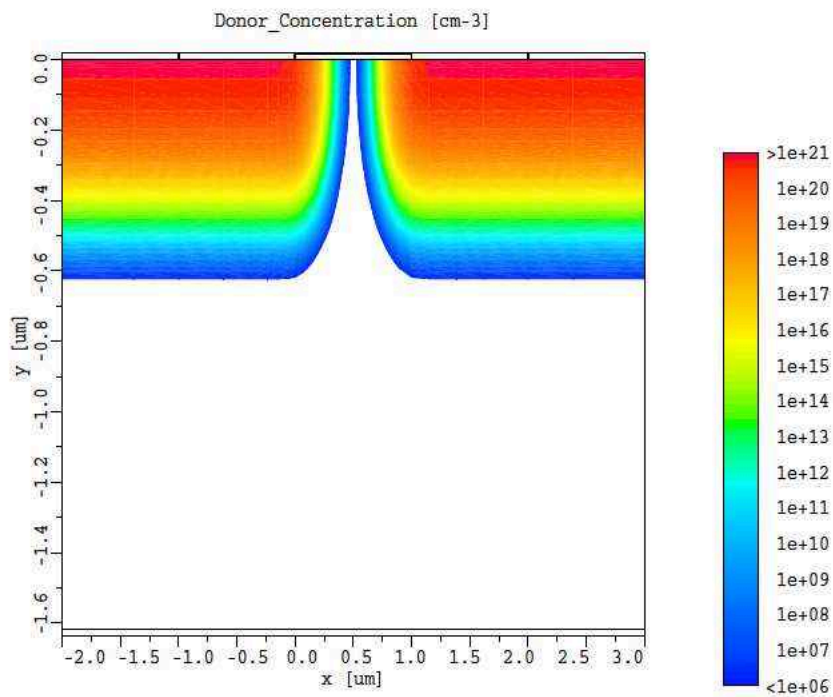


Figure 8.16: Donor doping distribution of NMOS and FEMFET

The operating conditions for the transistor were chosen at values similar to those of a CMOS transistor of the same gate length. V_D was 1.0V, bulk and source bias $V_B = V_S = 0$, respectively.

8.3.1 Transfer Characteristics

First the influence of the peak of the steering pulses on the operation points is analyzed. As expected the voltage shift between the up and the down curves increases if the applied amplitude is increased. The influence on the up curve is much stronger than on the other branch (Fig. 8.17 and Fig. 8.18).

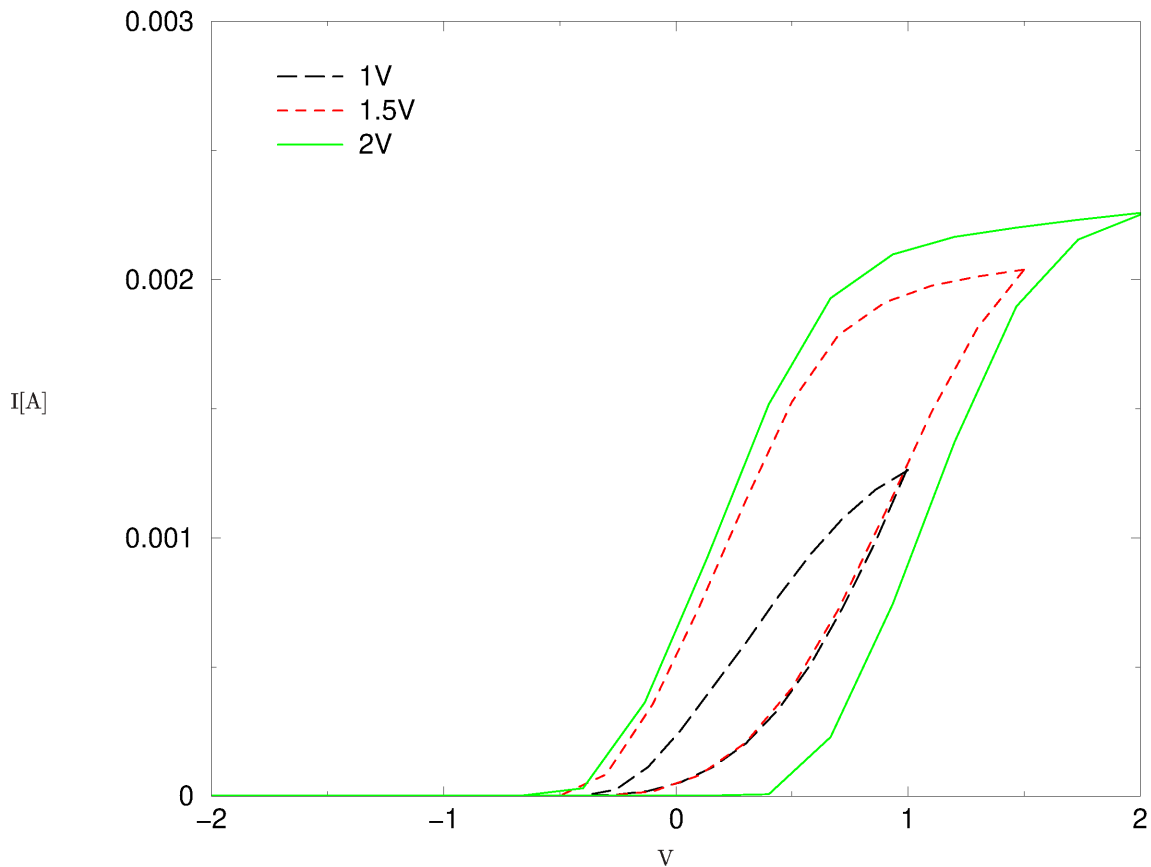


Figure 8.17: Transfer characteristics for different peak voltages, linear scale

8.3.2 Field and Charge Distribution

Using the new simulator allows to take a closer look at the properties inside the device and verify the operating principle outlined in Section 7.2.1.

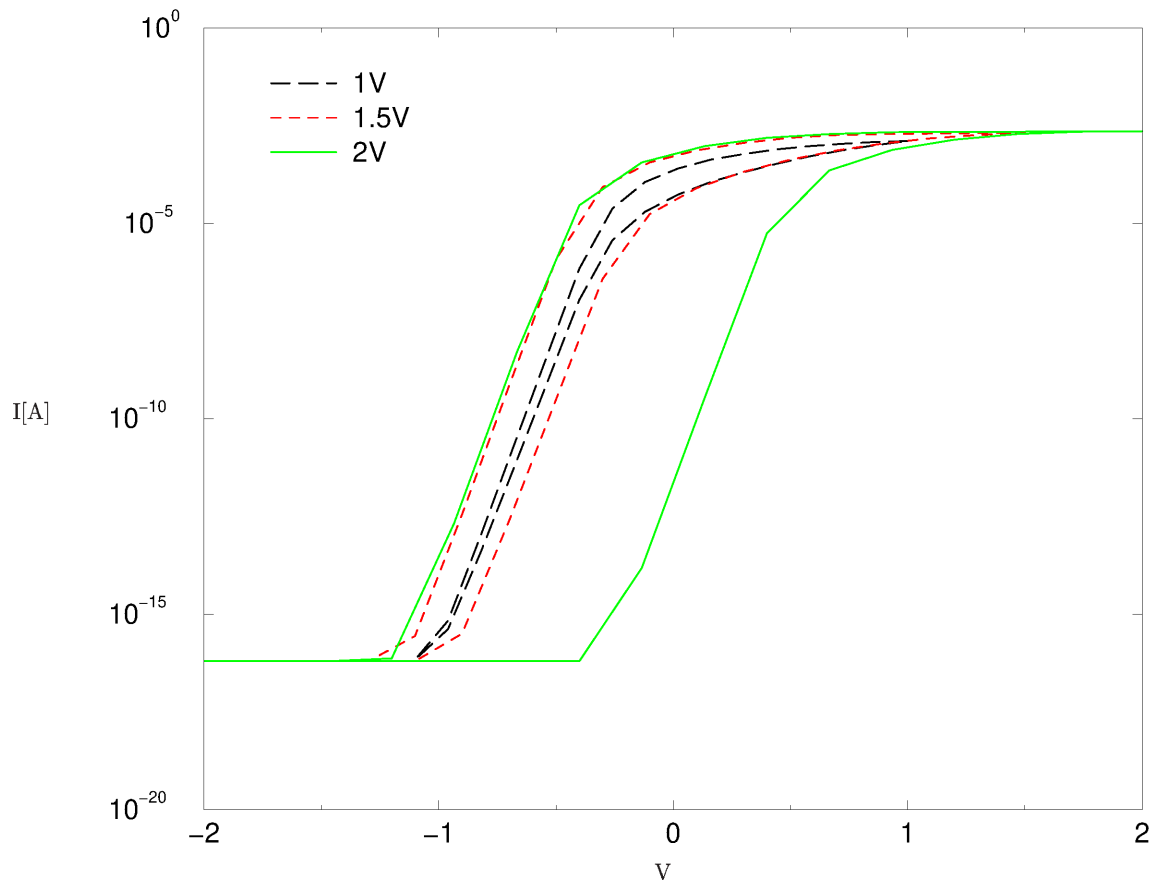


Figure 8.18: Transfer characteristics for different peak voltage, logarithmic scale

The gate voltage used for sensing was set to $V_g = 0V$. The applied peak values of the gate voltage pulses were $V_g = \pm 1V$. Fig. 8.19 and Fig. 8.21 show the space charge density and the current density in the ON state, Fig. 8.21 and Fig. 8.22 in the OFF state.

8.3.3 Discussion

These initial simulations of a FEMFET already show effects of the device geometry on the performance, which are related to two-dimensional properties. Fig. 8.19 shows that the charge distribution along the channel in the ON state is far from uniform, which causes strong impact on the ON current. Due to the highly nonlinear properties of a ferroelectric gate dielectric any change of drain or gate voltage shows a strong impact on charge distribution and current. This can be clearly seen in the plotted transfer characteristics (Fig. 8.17, Fig. 8.18), where an increase of the peak voltage by 0.5V leads to a threshold voltage shift of 1.5V. Using the simulator a rigorous analysis of these effects is now possible. The obtained results can be utilized to fulfill several tasks of fundamental interest for device engineering:

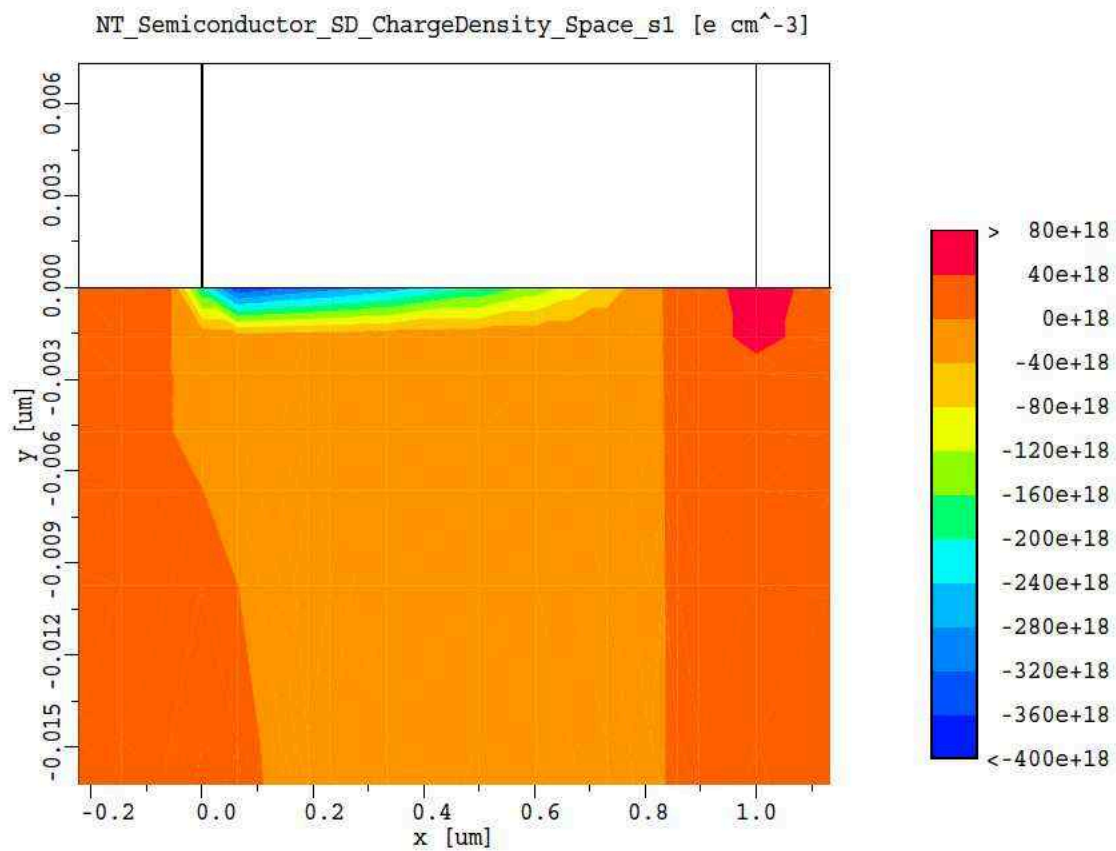


Figure 8.19: Space charge density in the ON state

- Optimization of the device geometry
- Optimization of operation schemes
- Development of compact models for circuit simulation

The fact that, according to the SIA roadmap [Sem99], the gate length of CMOS is getting shorter and shorter compared to the device size will increase the influence of the drain contact on the potential distribution in the channel, thus increasing the impact of the effects outlined above and, in parallel, the necessity to use a rigorous analysis tool as it is presented in this thesis.

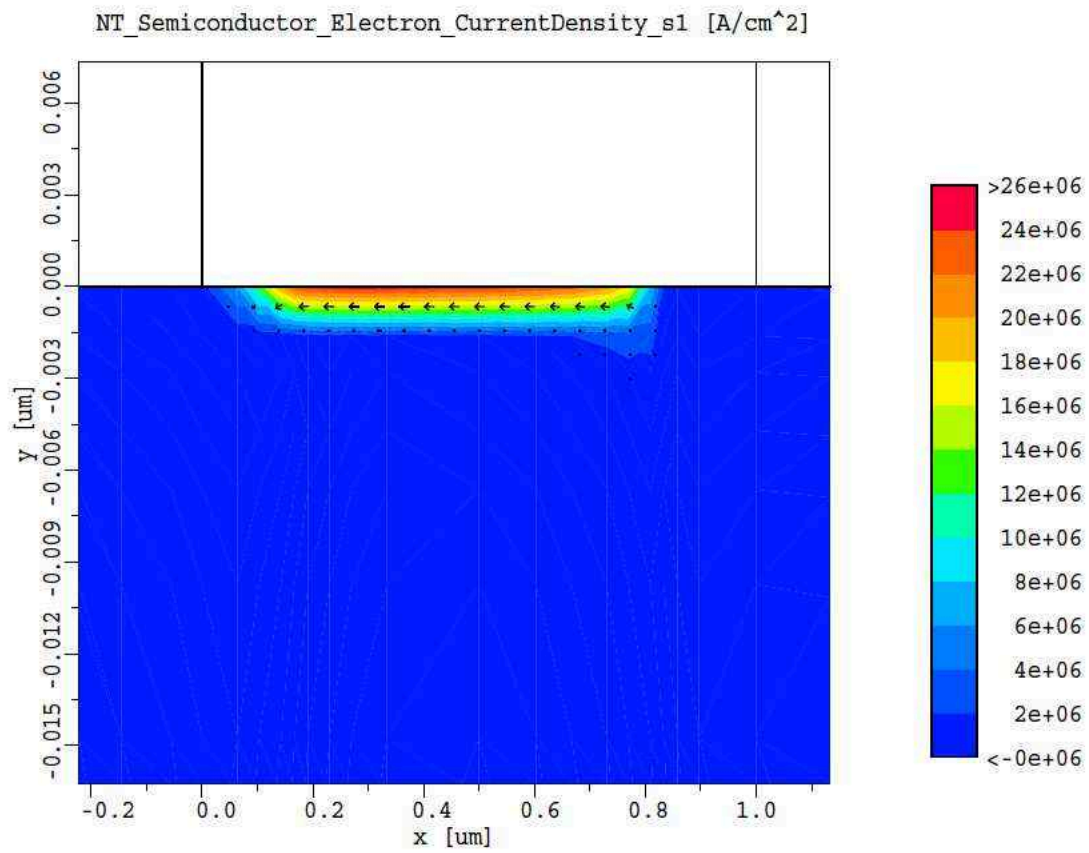


Figure 8.20: Current density in the ON state

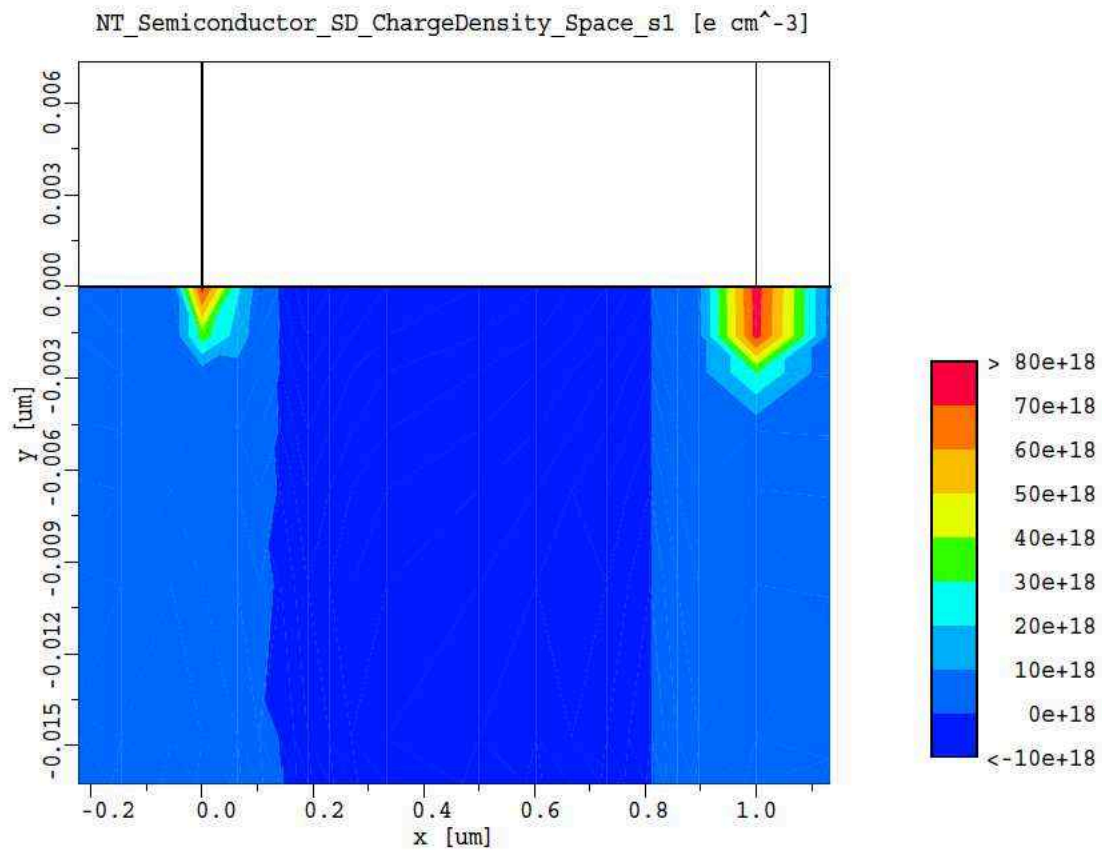


Figure 8.21: Space charge density in the OFF state

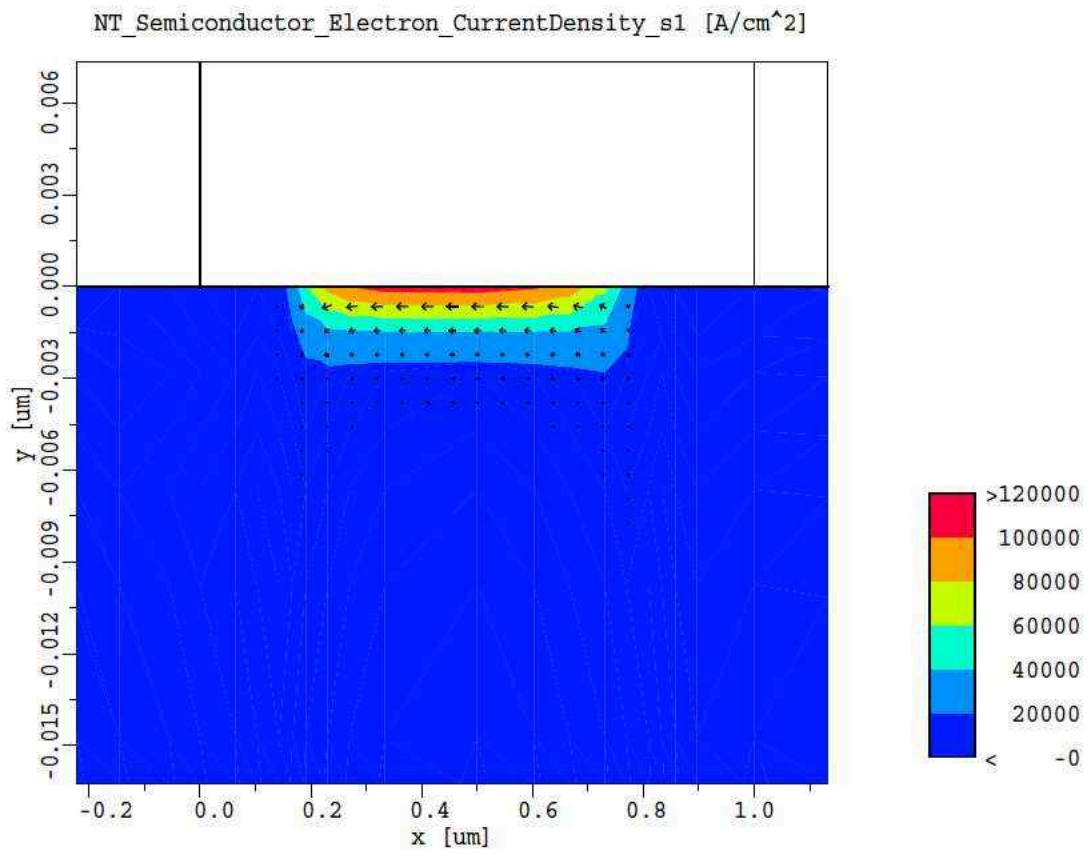


Figure 8.22: Current density in the OFF state

Chapter 9

Conclusion and Outlook

THE BASIC PURPOSE of this thesis was to find models for the analysis of ferroelectric memory cells. Starting from a comparison of existing approaches, new models, which match the constraints of computer aided device design, had to be developed. Now for the first time real two-dimensional simulation of ferroelectric materials with arbitrary geometry and material composition has become possible.

Special care was taken for the implementation of the new models into the device simulator MINIMOS-NT. Following the generic approach of MINIMOS-NT, a modular concept was found which will also be easily extendable for future simulation tasks, which is necessary as the knowledge about ferroelectric materials and the possible applications is still increasing.

In addition to the development and implementation of the two-dimensional algorithms, the transient properties were investigated, and a new model based on differential equations was developed. This model offers an excellent fit to the measured data for a frequency range starting from zero up to 1MHz.

In order to demonstrate possible applications of the new tools a series of concrete examples is provided. One of these examples builds a bridge from two-dimensional device geometry to circuit simulation, another one allows deep insight into the field properties inside an anisotropic crystal. The last example serves as the first profound analysis of a new, very promising nonvolatile memory cell, the FEMFET, and several critical issues concerning device performance and reliability are pointed out.

As earlier in this thesis a lot of research on ferroelectrics is carried out today. This will hopefully increase the availability of material data, thus allowing the extraction of the material parameters introduced in this thesis for a large number of different materials.

As outlined above this thesis was focused on the modeling of ferroelectric materials and the implementation of the resulting algorithms into a device simulator. This tool is now capable to allow a rigorous analysis of ferroelectric devices and opens the door to several critical issues concerning the development of the related memory cells. These include optimization of the device structure, extraction of possible operation schemes, and the development of compact models.

Bibliography

- [ATM⁺98] K. Amanuma, T. Tatsumi, Y. Maejima, S. Takahashi, H. Hada, H. Okizaki, and T. Kuno. Capacitor-on-Metal/Via-stacked- Plug (CMVP) Memory Cell for 0.25 μm CMOS Embedded FeRAM. *Proc.Intl.Electron Devices Meeting*, pages 363–366, 1998.
- [Bau99] L. Baudry. Theoretical Investigation of the Influence of Space charges on Ferroelectric Properties of PbZrTiO₃ Thin Film Capacitor. *J.Appl.Phys.*, 86(2):1096–1105, July 1999.
- [BDG⁺98] T. Binder, K. Dragosits, T. Grasser, R. Klima, M. Knaipp, H. Kosina, R. Mlekus, V. Palankovski, M. Rottinger, G. Schrom, S. Selberherr, and M. Stockinger. *MINIMOS-NT User's Guide*. Institut für Mikroelektronik, 1998.
- [BEL97] H.G. Brachtendorf, Ch. Eck, and R. Laur. Macromodeling of Hysteresis Phenomena with SPICE. *IEEE Trans.Circuits and Systems-II: Analog and Digital Signal Processing*, 44(5):378–388, May 1997.
- [BSHE83] J.A. Barker, D.E. Schreiber, B.G. Huth, and D.H. Everest. Magnetic Hysteresis and Minor Loops: Models and Experiments. In *Proceedings of the Royal Society of London*, volume A 386, pages 251–261, 1983.
- [CCR⁺99] B. Cheng, M. Cao, R. Rao, A. Inani, P. Vande Voorde, W.M. Greene, J.M.C. Stork, Z. Yu, P.M. Zeitzoff, and J.C.S. Woo. The Impact of High-k Gate Dielectrics and Metal Gate Electrodes on Sub-100nm MOSFET's. *IEEE Trans.Electron Devices*, 46(7):1537–1544, July 1999.
- [CCV⁺99] B. Cheng, M. Cao, P. Vande Voorde, W.M. Greene, J.M.C. Stork, Z. Yu, and J.C.S. Woo. Design Considerations of High-k Gate Dielectrics for Sub-0.1 μm MOSFET's. *IEEE Trans.Electron Devices*, 46(1):261–262, January 1999.
- [CPW97] J.F.M. Gillessen, M.W.J. Prins, and R.M. Wolf. Thickness Dependence of Switching Voltage in All-oxide Ferroelectric Thin-Film Capacitors Prepared by Pulsed Laser Deposition. *J.Appl.Phys.*, 81(6):2777–2783, March 1997.
- [DBL98] Guido W. Dietz, G. Braun, and O. Lohse. An Accurate Compact Model for Integrated Ferroelectric Capacitors. In *Siemens HL SIM confidential*, 1998.
- [Die97] G.W. Dietz. SrTiO₃-Dünnschichten unter dem Einfluss elektrischer Gleichfelder, volume 215 of *Fortschrittberichte VDI Reihe 21*. VDI-Verlag, Düsseldorf, 1997.

- [Dir86] H.J. Dirschmid. *Mathematische Grundlagen der Elektrotechnik*. Vieweg, 1986.
- [Dun94] D.E. Dunn. A Ferroelectric Capacitor Macromodel and Parametrization Algorithm for Spice Simulation. *IEEE Transactions on Ultrasonics, Ferroelectrics, and Frequency Control*, 41(3):360–369, May 1994.
- [EW88] J.T. Evans and R. Womack. An Experimental 512-bit Nonvolatile Memory with Ferroelectric Storage Cell. *IEEE J.Solid-State Circuits*, 23:1171–1175, 1988.
- [Fas87] G. Fasching. *Werkstoffe für die Elektrotechnik*. Springer, Wien, 1987. 2. Auflage.
- [Fis94] C. Fischer. *Bauelementsimulation in einer computergestützten Entwurfsumgebung*. Dissertation, Technische Universität Wien, 1994. <http://www.iue.tuwien.ac.at/diss/fischer/diss-new/diss.html>.
- [GLB⁺98] M. Grossmann, O. Lohse, D. Bolten, R. Waser, W. Hartner, G. Schindler, C. Dehm, N. Nagel, V. Joshi, N. Solayappan, and G. Derbenwick. Imprint in Ferroelectric SrBi₂Ta₂O₉ Capacitors for Non-volatile Memory Applications. In *Proceedings ISIF10, Monterey*, March 1998.
- [IRCW99] A. Inani, Ramgopal V. Rao, B. Cheng, and J. Woo. Gate Stack Architecture Analysis and Channel Engineering in Depp Sub-Micron MOSFETs. *J.Appl.Phys.*, 38(4B):2266–2271, April 1999.
- [Ish92] Y. Ishibashi. Hysteresis Loops in Ferroelectris Undergoing an Isomorphpous Phase Transition. *Japanese Journal of Applied Physics*, 31(2A):327–328, February 1992.
- [JA86] D.C. Jiles and D.L. Atherton. Theory of Ferromagnetic Hysteresis. *Journal of Magnetism and Magnetic Materials*, 61:48–60, 1986.
- [JCJ⁺97] R.E. Jones Jr., P.Y. Chu, B. Jiang, B.M. Melnick, D.J. Taylor, B.E. White Jr., S. Zafr, D. Price, P. Zurcher, S.J. Gillespie, T. Otsuki, T. Sumi, Y. Judai, Y. Uemoto, E. Fujii, S. Hayashi, N. Moriwaki, M. Azuma, Y. Shimada, K. Arita, H. Hirano, J. Nakane, T. Nakanum, and G. Kano. Non Volatile Memories Using SrBi₂Ta₂O₉ Ferroelectrics. *Integrated Ferroelectrics*, 17:21–30, 1997.
- [JZJ⁺97] B. Jiang, P. Zurcher, R.E. Jones, S.J. Gillespie, and J.C. Lee. Computationally Efficient Ferroelectric Capacitor Model for Circuit Simulation. In *IEEE Symposium on VLSI Technology Digest of Technical Papers*, pages 141–142, 1997.
- [Kit86] Ch. Kittel. *Introduction to Solid State Physics*. Wiley, New York, sixth edition, 1986.
- [KTM⁺97] S. Kobayashi, N. Tanabe, Y. Maehima, Y. Hayashi, and T. Kunio. Scaling Possibility of PZT Capacitors for High Density and Low-Voltage NVFRAM Application. *Integrated Ferroelectrics*, 17:81–88, 1997.
- [KYY⁺98] S. Krishnan, G.C.-F Yeap, B. Yu, Q. Xiang, and M. Lin. High-k Scaling of Gate Insulators: an Insightful study. In *Proc. Conf. on Microelectronic Device Technology*, volume 3506, pages 65–72. SPIE, September 1998.

- [LDTvV94] P.K. Larsen, G.J.M. Dormans, D.J. Taylor, and P.J. van Veldhoven. Ferroelectric Properties and Fatigue of $\text{PbZr}_{0.51}\text{Ti}_{0.49}\text{O}_3$ Thin Films of Varying Thickness: Blocking Layer Model. *J.Appl.Phys.*, 76(4):2405–2413, August 1994.
- [LG96] M.E. Lines and A.M. Glass. *Principles and Applications of Ferroelectrics and Related Materials*. Oxford University Press, 1996.
- [LWK⁺98] H.F. Luan, B.Z. Wu, L.G. Kang, B.Y. Kim, R. Vrtis, D. Roberts, and D.L. Kwong. Ultra High Quality Ta_2O_5 Gate Dielectric Prepared by In-situ Rapid Thermal Processing. In *Proc.Intl.Electron Devices Meeting*, pages 609–612, 1998.
- [Max91] J.C. Maxwell. *A Treatise on Electricity and Magnetism*. Dover, New York, 1991. 3.Edition.
- [Maz00] C. Mazure. FeRAM Technology. *29th European Solid-State Device Research Conference*, pages 64–67, 2000.
- [MF53] T. Mitsui and J. Furuichi. Domain Structure of Rochelle Salt and KH_2PO_4 . *Physical Review*, 90(2):193–203, 1953.
- [MM92] S. L. Miller and P. J. McWhorter. Physics of the Ferroelectric Nonvolatile Memory Field Effect Transistor. *J.Appl.Phys.*, 72(12):5999–6010, 1992.
- [MNS⁺90] S.L. Miller, R.D. Nasby, J.R. Schwank, M.S. Rodgers, and P.V. Dressendorfer. Device Modeling of Ferroelectric Capacitors. *J.Appl.Phys.*, 68(12):6463–6471, 1990.
- [MOS⁺99] Y. Ma, Y. Ono, L. Stecker, D.R. Evans, , and S.T. Hsu. Zirconium Oxide Based Gate Dielectrics with Equivalent Oxide Thickness of Less than 1.0nm and Performance of Submicron MOSFET Using a Nitride Gate Replacement Process. In *Proc.Intl.Electron Devices Meeting*, pages 149–152, 1999.
- [MWC99] R. McKee, F. Walker, and M. Chisholm. Crystalline oxides on silicon-alternative dielectrics for advanced transistor technologies. In *Ultrathin SiO_2 and High-K Materials for ULSI Gate Dielectrics. Symposium*, volume 17, pages 415–425, 1999.
- [Nag75] L.W. Nagel. SPICE2: A Computer Program to Simulate Semiconductor Circuits. Technical Report UCB/ERL M520, University of California, Berkeley, 1975.
- [OAI91] M. Omura, H. Adachi, and Y. Ishibashi. Simulation of Ferroelectric Characteristics Using a One-Dimensional Lattice Model. *Japanese Journal of Applied Physics*, 30(9B):2384–2387, September 1991.
- [OAI92] M. Omura, H. Adachi, and Y. Ishibashi. Simulation of Polarization Reversals by a Two-Dimensional Lattice Model. *Japanese Journal of Applied Physics*, 31(9B):3238–3240, September 1992.
- [PBOZ97] P. Pavan, R. Bez, P. Olivo, and E. Zanoni. Flash Memory Cells – An Overview. *Proc.IEEE*, 85(8):1248–1271, August 1997.

- [Pfi94] H. Pfützner. Rotational Magnetization and Rotational Losses of Grain Oriented Silicon Steel Sheets—Fundamental Aspects and Theory. *IEEE Trans.Magnetics*, 30(5):2802–2807, 1994.
- [Pre35] F. Preisach. Über die magnetische Nachwirkung. *Zeitschrift für Physik*, 94:277–302, 1935.
- [RW95] K.M. Rabe and U.V. Waghmare. Localized Basis for Effective Lattice Hamiltonians: Lattice Wannier Functions. *Physical Review B*, 52(18):13236–13246, November 1995.
- [Sch97] H.R. Schwarz. *Numerische Mathematik*. Teubner, Stuttgart, 1997. 4. Auflage.
- [Sco95] J.F. Scott. Models for the Frequency Dependence of Coercive Field and the Size Dependence of Remanent Polarization in Ferroelectric Thin Films. *Integrated Ferroelectrics*, 12:71–81, 1995.
- [Sem99] Semiconductor Industry Association. The National Technology Roadmap for Semiconductors, 1999.
- [SG00] A. Sheikholeslami and G. Gulak. A Survey of Circuit Innovations in Ferroelectric Random-Access Memories. *Proceedings of the IEEE*, 88(5):667–689, May 2000.
- [SMN⁺95] T. Sumi, N. Moriwaki, G. Nakane, T. Nakakuma, Y. Judai, Y. Uemoto, Y. Nagano, S. Hayashi, M. Azuma, T. Otsuki, G. Kano, J.D. Cuchiario, M.C. Scott, L.D. McMillan, and C.A. Paz de Araujo. A Model of Voltage Dependent Dielectric Losses for Ferroelectric MMIC Devices. *Integrated Ferroelectrics*, 6:1–13, 1995.
- [TAH⁺97] M. Takeo, M. Azuma, H. Hirano, K. Asari, N. Moriwaki, T. Otsuki, and K. Tatsuuma. SrBi₂Ta₂O₉ Thin Film Capacitor Model Including Polarization Reversal Response for Nanosecond Range Circuit Simulation of Ferroelectric Nonvolatile Memory. In *Proc.Intl.Electron Devices Meeting*, pages 621–624, 1997.
- [UGH⁺99] M. Ullmann, H. Goebel, H. Hoenigschmid, T. Haneder, and G.W. Dietz. An Accurate Compact Model for Ferroelectric Memory Field Effect Transistors. In *Simulation of Semiconductor Processes and Devices*, pages 175–178, Kyoto, Japan, September 1999.
- [WP08] P. Weiss and V. Planer. Hystérèse dans les Champs Tournants. *Journal de Physique (Théor. et Appl.)*, 4/7:5–27, 1908.
- [WR97] U.V. Waghmare and K.M. Rabe. Ab Initio Statistical Mechanics of the Ferroelectric Phase Transition in PbTiO₃. *Physical Review B*, 55(10):6161–6173, March 1997.
- [YKL98] G.C.-F. Yeap, S. Krishnan, and M. Lin. Fringing-induced Barrier Lowering (FIBL) in Sub-100nm MOSFETs with High-k Gate Dielectrics. *Electronics Letters*, 34(11):1150–1152, May 1998.

List of Publications

- [P12] K. Dragosits and S. Selberherr, “Two-Dimensional Simulation of Ferroelectric Memory Cells”, in *IEEE Transactions on Electron Devices*, to be published in February 2001
- P[11] K. Dragosits, R. Kosik, and S. Selberherr, “Two-Dimensional Simulation of Ferroelectric Materials”, in *Integrated Ferroelectrics*, to be published
- [P10] K. Dragosits and S. Selberherr, “Simulation of Ferroelectric Thin Films”, in *Radiation and Defects in Solids*, to be published
- [P9] K. Dragosits and S. Selberherr, “Simulation of Ferroelectric Materials with MINIMOS-NT”, in *Abstracts of 2000 MRS Spring Meeting*, San Francisco, California, USA p. 249, April 2000
- [P8] K. Dragosits and S. Selberherr, “Simulation of Ferroelectric Nonvolatile Memory Cells with MINIMOS-NT”, in *Proceedings of the 3rd International Conference on Micro Materials MicroMat2000*, Berlin, Germany, pp. 1023-1026, April 2000
- [P7] K. Dragosits and S. Selberherr, “Simulation of Ferroelectric Thin Films”, in *Programme and Abstracts of the 14th International Conference on Defects in Insulating Materials*, Johannesburg–Midrand, South Africa, p. 179, April 2000
- [P6] K. Dragosits, R. Hagenbeck, and S. Selberherr, “Transient Simulation of Ferroelectric Hysteresis”, in *Proceedings of the 3rd International Conference on Modeling and Simulation of Microsystems*, San Diego, California, USA, pp. 433-436, March 2000
- [P5] K. Dragosits, R. Kosik, and S. Selberherr, “Two-Dimensional Simulation of Ferroelectric Materials”, in *Abstracts of the 12th International Symposium on Integrated Ferroelectrics*, Aachen, Germany, p. 128, March 2000
- [P4] K. Dragosits, M. Knaipp, and S. Selberherr, “Two-Dimensional Simulation of Ferroelectric Memory Cells”, in *Journal of the Korean Physical Society*, Vol. 35 , pp. S104–S106, July 1999.
- [P3] K. Dragosits and S. Selberherr, “Numerical Aspects of the Simulation of Two-Dimensional Ferroelectric Hysteresis”, in *Proceedings of the 2nd International Conference on Modeling and Simulation of Microsystems*, San Juan, Puerto Rico, USA, pp. 309–312, April 1999
- [P2] K. Dragosits, M. Knaipp, and S. Selberherr, “Two-Dimensional Simulation of Ferroelectric Memory Cells”, in *Simulation of Semiconductor Processes and Devices* (K. De Meyer and S. Biesemans, eds.), pp. 368–371, Leuven, Belgium, Sept. 1998.
- [P1] K. Dragosits, M. Knaipp, and S. Selberherr, “Two-Dimensional Simulation of Ferroelectric Memory Cells”, in *Abstract Book of the 4th International Conference on Electronic Materials*, Cheju, Korea, p. 40, August 1998.

Curriculum Vitae

- June 2000 – July 2000 Visiting Researcher at the Samsung Institute of Advanced Technology, Suwon, Korea, working on the simulation of the transient behavior of ferroelectric materials.
- March 2000 Visiting Researcher at Philips Research, Eindhoven, the Netherlands, working on the analysis of high-k gate structures.
- since September 1997 Technical University of Vienna, Austria. Enrolled in a full Ph.D. program at the Institute for Microelectronics under the supervision of Prof. Siegfried Selberherr.
- 1996 – 1997 Compulsory community service.
- 1987 – 1996 Technical University of Vienna, Austria, master's degree, "Diplomingenieur", in Communication Engineering.
- 1979 – 1987 High school, Reutte in Tirol, Austria.
- 1975 – 1979 Primary school, Lechaschau, Austria.
- October 9, 1969 Born in Bruck an der Mur, Austria.